The role of standing and travelling waves in stratosphere-troposphere coupling

by

Oliver Watt-Meyer

A thesis submitted in conformity with the requirements
for the degree of Doctor of Philosophy
Graduate Department of Physics
University of Toronto

Abstract

The role of standing and travelling waves in stratosphere-troposphere coupling

Oliver Watt-Meyer
Doctor of Philosophy
Graduate Department of Physics
University of Toronto
2016

Upward wave activity flux in the mid-latitudes is a strong control on the strength and temperature of the stratospheric polar vortex in the Northern Hemisphere winter. In this thesis, the variability of upward wave activity flux is studied using the ideas of linear interference. This framework separates meteorological fields into a zonally asymmetric climatology—the stationary wave—and a wave anomaly. Fluxes are then decomposed into a linear term that measures the spatial coherence of the anomaly and the climatology and an additional nonlinear term. In order to determine the structure of the wave anomalies that interfere with the climatology, a novel spectral decomposition of wave disturbances into standing and travelling components is developed. Unlike previous methods, it explicitly accounts for the covariance between the two components. The decomposition is applied to planetary waves in the Northern Hemisphere winter. It is shown that standing waves explain the majority of the variance of the linear part of the upward wave activity flux. Furthermore, the connection between upward wave activity flux in the troposphere and the strength of the stratospheric polar vortex is shown to be primarily driven by standing waves amplifying and attenuating the climatological wave.

The relationship between the linear and nonlinear parts of the upward wave activity flux is investigated. It is shown that there is a roughly quadratic relationship between the two when considering individual wavenumbers, and that this can act as an explanation for the positive skewness of the wavenumber-1 upward wave activity flux distribution. A

statistical model is constructed which demonstrates that a westward tilted climatological wave is the key ingredient in having a positively skewed wave activity flux distribution.

Last, the analysis is extended to consider the dynamics of tropospheric variability and weather extremes. The standing-travelling wave decomposition is applied to tropospheric weather variability in order to separate the slow and fast drivers of cold winter weather over eastern North America. It is found that standing waves driven from the tropics largely control the large-scale ridge-trough structure over North America, but that eastward travelling synoptic waves can strongly modify it on shorter timescales.

For my parents Pati and Bernard, whose immeasurable
love and support made this thesis possible.

Acknowledgements

Arriving at the University of Toronto five years ago, I was completely new to the fields of atmospheric and climate science. I am grateful to many people for introducing me to these areas, teaching me so much about them and sharing their excitement for them with me.

I am particularly grateful to my supervisor, Dr. Paul Kushner, for his academic guidance throughout my time as a graduate student. From the suggestion of my thesis topic to regular and thoughtful advice on research directions and strategies, he has made every effort to ensure the success of my graduate degree. His substantial support for travel to conferences and the connections to researchers around the world he has provided me with have been invaluable. Paul's careful approach to science has been an excellent model to learn from, and I have become a better scientist under his guidance.

I would also like to thank my committee members, Dr. W. Richard Peltier and Dr. Kimberly Strong. Their suggestions at regular committee meetings were always helpful, and I am appreciative of their support for my research.

During the summer of 2015, I spent three months at the National Center for Atmospheric Research in Boulder, Colorado. I am very grateful to Dr. Jadwiga Richter for hosting me there, as well as to Dr. Isla Simpson and Dr. Lantao Sun for regularly meeting with me and giving helpful advice on research directions. I would also like to thank Dr. Karen Smith for hosting me at the Lamont-Doherty Earth Observatory for a fruitful visit in 2013. In addition, throughout my degree, Karen has made significant effort to help me understand aspects of her previous work and has given me excellent suggestions for my own research.

It has been a huge help to have likeminded people around in the Atmospheric Physics group. Thanks to Melanie, Russell, Fred, Neil, Ellen, Robert, Adeline, Keven, Deepak, Hesam and many others for the helpful science chats, and even more so, the helpful beers and barbecues. From Brewer seminars to weather club to the picket line, it's been great to do this with all of you.

Finally, enormous thanks to my family and friends. My brother Ben for inspiring me with his passion and hard work, and my parents Pati and Bernard for their constant love and support. And to all my friends outside of science: Jarlath, Matt, Ross, BWI, Karen and many others, thank you for keeping me thinking about the bigger picture.

Contents

List of Tables

List of Figures

Chapter 1

Introduction

1.1 Preface

In their seminal paper on the wave-driven variability of the stratospheric polar vortex, Holton and Mass (1976) began as follows:

> The winter seasonal mean circulation of the Northern Hemisphere stratosphere consists primarily of planetary waves of zonal wavenumbers 1 and 2 superposed on a zonal westerly vortex. The planetary waves are quasi-stationary in phase but tend to fluctuate in amplitude. Occasionally the anomalous amplification of such waves leads to an enormous enhancement of the poleward eddy heat flux which in turn leads to a reversal of the normal pole-to-equator temperature gradient over a sufficient depth of the stratosphere so that the mean polar westerlies are replaced by easterlies. [...] However, relatively little attention has been given to the weaker wave-mean flow oscillations which occur at about 1 to 4 week intervals throughout the winter.
>
> These quasi-periodic oscillations, [...] can, to a large extent, be accounted for by the presence of traveling wave modes which alternately constructively and destructively interfere with the quasi-stationary waves.

This passage demonstrates the intuitive understanding that Holton and Mass had in regards to the types of wave variability that drives fluctuations in the strength of the stratospheric circulation: the most important effect is the change in amplitude of quasi-stationary planetary waves, but travelling waves moving in and out of phase with

the quasi-stationary component are a key secondary consideration. Research in the years since the study of Holton and Mass (1976) has confirmed that amplification and attenuation of the climatological or stationary wave can explain the stratospheric response to various tropospheric forcings such as El Niño (Ineson and Scaife, 2009; Garfinkel et al., 2010; Fletcher and Kushner, 2011) or Eurasian snow cover anomalies (Smith et al., 2010, 2011), as well as stratospheric variability more generally (Smith and Kushner, 2012). Furthermore, it has been shown that interference between travelling and stationary waves can significantly modulate the strength of upward wave activity flux (Salby and Garcia, 1987). However, a quantitative analysis of the relative roles of these two types of variability in wave-mean flow interactions in the stratosphere has not been undertaken.

The primary advance of this thesis is to precisely quantify the relative portions of wave-driving of the stratosphere that come from standing waves amplifying and attenuating the stationary climatological wave versus travelling waves moving in and out of phase with the stationary wave. In order to do this, a novel spectral decomposition of wave variability into standing and travelling components is developed (Chapter 2). Defining such a decomposition is not trivial due to the fact that standing and travelling waves are in general not orthogonal. Nevertheless, we find that our method gives reasonable results in various contexts and is an improvement on previous methods developed in the papers Hayashi (1973, 1977, 1979); Pratt (1976) and documented in the standard textbook (von Storch and Zwiers, 1999). The decomposition is applied to geopotential height anomalies in the Northern Hemisphere winter and it is shown that for planetary scales, standing waves are usually dominant but at certain frequencies there are strong travelling wave modes. Using this method, we find that the standing waves explain the majority of the variance of the component of upward wave activity flux that is driven by waves coherent with the climatological wave, and are an important precursor to sudden stratospheric warmings (Chapter 3).

In addition to its primary focus on the drivers of upward wave activity flux variability, this thesis addresses two additional topics. First, the cause of the positive skewness of the temperature distribution in the polar stratosphere is examined (Chapter 4). It is shown that upward wave activity flux itself has a positive skew, and this suggests that there may be a role for dynamics in setting the non-Gaussian nature of the temperature distribution. The skewness of the upward wave activity distribution is explained by appealing to a newly demonstrated relationship between the component of wave activity flux that is due to the wave anomaly's interference with the climatological wave, and the

component that is solely due to the wave anomaly.

The analytical framework developed in Chapter 2 has broader applications. In the final part of the original research presented in this thesis, the standing-travelling wave analysis is applied to the Northern Hemisphere winter mid-tropospheric atmospheric circulation (Chapter 5). The motivation is to better understand the drivers of the anomalously cold weather that was experienced in eastern North America during the winters of 2013/14 and 2014/15. The contributions that these wave types make to the ridge-trough structure over North America that was proximally responsible for the cold conditions is examined. It is shown that although standing waves are most important overall to the cold temperatures experienced in these winters, an eastward travelling wave of nearly record-breaking amplitude drove the extreme cold temperatures over eastern North America on 7 January 2014.

The remainder of this chapter introduces concepts that will be used throughout this thesis. First, an overview of the most important types of waves found in the atmosphere is provided (Section 1.2). Some of the terms that will be used to describe them, including *stationary*, *standing* and *travelling* are defined. As well, a brief introduction to the idea of a standing-travelling wave decomposition is given. Section 1.3 outlines some aspects of extratropical stratospheric variability and explains its importance for extended timescale predictability and ozone chemistry. A summary of the Transformed Eulerian Mean theory, which can be used to explain the meridional and vertical propagation of waves in the atmosphere and their impact on the zonal-mean flow, is provided. Section 1.4 introduces the concept of stationary wave driving, or linear interference. This is a way to understand the impact of climatological zonal asymmetries in the atmosphere (i.e. the stationary waves in the Northern Hemisphere) on the variability of upward wave activity flux. Finally, Section 1.5 discusses the use of the standing-travelling wave decomposition for understanding the tropospheric extratropical circulation. Last, Section 1.6 summarizes the introduction and lists which parts of this thesis have been published or are in preparation for submission.

1.2 Atmospheric waves

A basic way to begin to understand planetary atmospheric circulations is to separate quantities into their zonal means and deviations therefrom (e.g. Section 4.1 of Peixoto

and Oort, 1992). In many cases, the deviation from the zonal mean, which is typically referred to as the eddy component, exhibits wavelike behaviour such as a well defined dispersion relation. Furthermore, the interaction between the eddy and zonal mean parts of the flow is known to be of fundamental importance for various properties of the Earth's atmospheric circulation, like the existence of sharp jet streams (e.g. Baldwin et al., 2007) and the occurrence of phenomena such as sudden stratospheric warmings (see Section 1.3). This section classifies the eddy component of the atmospheric circulation into different wave types that have differing underlying physical mechanisms. It then introduces the decomposition of atmospheric waves into standing and travelling components, which will be discussed in detail throughout this thesis.

Wave variability in the extratropical atmosphere occurs on a vast range of length and timescales. Wave types can be distinguished by their restoring mechanisms. Buoyancy or gravity waves exist in the atmosphere because of the strong vertical gradient in density—air parcels that are displaced upwards or downwards will have larger or smaller densities than the surrounding air, and thus will be accelerated in the opposite direction as the initial displacement resulting in oscillatory motion. The primary sources of gravity waves are airflow over topography and convective activity, and they dominate variability on shorter length and time scales (on the order of kilometres to hundreds of kilometres, and minutes to hours) (Fritts, 2003). While gravity waves are essential in explaining the circulation of the mesosphere and higher layers (e.g. McIntyre, 1989), in the troposphere and stratosphere they are of relatively smaller dynamical importance, although certainly not negligible. In these lower layers of the atmosphere, in the extratropics, Rossby waves are the most important type of wave variability for large (i.e. synoptic and planetary) spatial scales. Rossby waves are supported by the meridional gradient in potential vorticity provided by the Earth's rotation. They are dominant on longer length scales—thousands to tens of thousands of kilometres—and time scales—days to weeks. They manifest themselves most familiarly as the eastward travelling high and low pressure systems associated with weather in the extratropics, but also exist as planetary-scale disturbances, both stationary and travelling.

For clarity, the precise definitions of stationary, standing and travelling waves are provided here. Note that these terms, in particular standing, are sometimes used differently by other authors. See discussion in Section 4.1 of Andrews et al. (1987).

- *Stationary waves* are typically defined as the time-mean part of the wave field, and hence have phases and amplitudes that are fixed with time. They are forced by

asymmetries in the Earth's surface, such as topography, which are themselves fixed in place.

- *Standing waves* are disturbances of the form $\cos(k\lambda)\cos(\omega t)$, i.e. waves with fixed nodes and antinodes, like standing waves on a string.
- *Travelling waves* are those whose phases change over time. They have the mathematical form $\cos(k\lambda - \omega t)$.
- The *climatological stationary wave* is the wave field averaged over many years. Hence, it does not vary from year to year, but it can vary within a season.

A basic point is that a standing wave is the sum of two oppositely travelling waves of equal amplitude and phase speed: $2\cos(k\lambda)\cos(\omega t) = \cos(k\lambda - \omega t) + \cos(k\lambda + \omega t)$. Because of this, standing and travelling waves of the same wavenumber and frequency are not independent, and it is thus not trivial to separate a total wave field into its standing and travelling components. Estimation of standing and travelling wave power spectra has been described previously (Hayashi, 1973, 1977, 1979; Pratt, 1976). However, the methods proposed by Hayashi and Pratt both suffer from the same issue: they exclusively decompose the power spectrum into standing and travelling parts with no possibility for covariance between these wave structures. We will show in Chapter 2 that although standing-travelling wave decompositions are not unique, the most useful formulations yield standing waves that are not orthogonal to the travelling waves and hence include significant covariance.

1.3 Stratospheric variability and stratosphere troposphere coupling

In this section, some basic characteristics of the mean-state and of the variability of the extratropical stratospheric circulation are introduced. The importance of understanding the variability of the strength of the stratospheric polar vortex is due to a wide range of dynamical and chemical processes. For example, a strong and undisturbed polar vortex acts as a transport barrier to mixing between the polar and mid-latitude regions, and also leads to cold temperatures within the polar vortex. Both of these factors are important for the chemistry of ozone loss. Furthermore, the state of the stratosphere has an impact onto the troposphere circulation on sub-seasonal, interannual and decadal timescales.

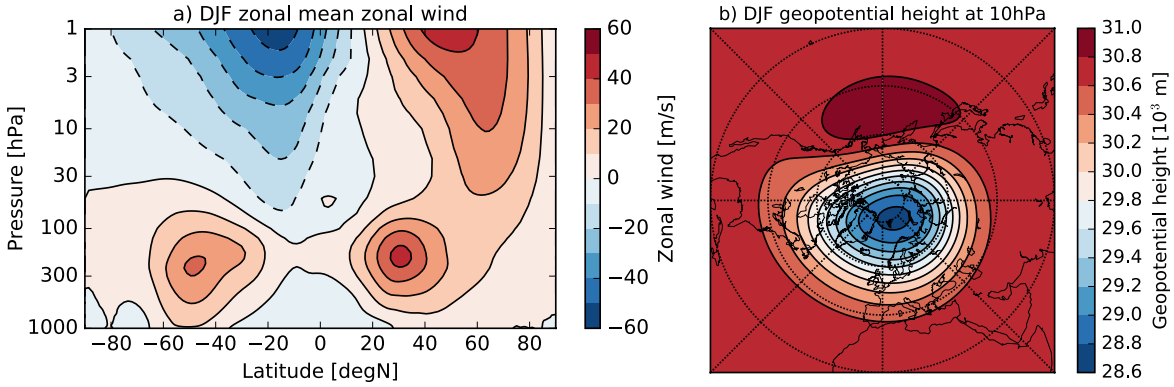

Figure 1.1: The climatological a) zonal mean zonal wind and b) geopotential height at 10hPa averaged over all December, January and February days. Computed from the ERA-Interim Reanalysis (Dee et al., 2011) using the years 1979-2013.

It also plays an important role in modulating the tropospheric response to increased greenhouse gas forcing. The details of these connections will be discussed at the end of this section.

The climatological zonal-mean Northern Hemisphere winter circulation in the stratosphere consists of strong (20 to 50 m/s) westerly winds roughly within 45°N and 75°N (Fig. 1.1a). This is the stratospheric polar vortex, which is the dominant feature of the extratropical circulation in the wintertime stratosphere. On average, the vortex in the mid-stratosphere tends to be displaced towards northern Europe, with an anticyclone over the Aleutian islands (Fig. 1.1b). However, the Northern Hemisphere's vortex exhibits a large amount of variability, including movement of its location, stretching and distortion of its shape and, occasionally, a complete breakdown of the vortex along with a reversal of the winds and a strong warming (up to 30-40K) in the polar stratosphere over the course of just a few days. These events, termed sudden stratospheric warmings (SSWs)[1], were first observed by rocketsondes in the 1950s (Scherhag, 1952). Some early attempts to explain the SSW phenomenon considered the possibility of internal instabilities of the jet in the stratosphere (Murray, 1960; McIntyre, 1972), but were unable to explain the key features of SSWs (for example, the most unstable modes were predicted to be of significantly smaller spatial scales than the wave-1 and wave-2 disturbances typically associated with SSWs). The first theory to successfully capture the main features of these events was presented by Matsuno (1971). The proposed mechanism was that planetary waves generated in the troposphere propagate upwards and deposit easterly momentum in the upper stratosphere. Since density decreases with altitude, the wave

[1]Historically, stratospheric sudden warming was used interchangeably with sudden stratospheric warming, but efforts are being made to standardize the phrase as it used here (Butler et al., 2015).

amplitudes will increase with height and force a larger easterly acceleration at higher levels. At some level, the westerly jet will eventually be reversed and a critical layer will be formed. This critical layer will force a dissipation of the upward propagating waves, and lead to a rapidly descending change in the zonal winds to easterly, as observed during SSW events. In general, this is still the most widely accepted model for SSWs, although there are various additional complexities required for a quantitative understanding of observed SSWs. For example, preconditioning of the stratosphere, that is, dynamical forcing of the stratospheric polar vortex such that its shape and strength is ideal for further upward propagation of wave activity, is thought to be an important part of the SSW lifecycle (Labitzke, 1981; Butchart et al., 1982; McIntyre, 1982; Limpasuvan et al., 2004). This can occur through either planetary or gravity wave driving (Albers and Birner, 2014). A separate theory of Rossby wave resonance causing SSWs has also been proposed by some authors (Tung and Lindzen, 1979a,b; Plumb, 1981; Esler and Scott, 2005; Esler et al., 2006). Finally, SSW events are often separated into two categories, "split" and "displacement", based on the spatial structure of the polar vortex during the events (e.g. Charlton and Polvani, 2007). Evidence will be shown in this thesis which suggests that these types of events have distinct precursors.

The modern theoretical framework for understanding the propagation of waves in the atmosphere and their impact on zonal mean winds and temperatures is the Transformed Eulerian Mean (TEM) theory (Eliassen and Palm, 1961; Andrews and McIntyre, 1976; Andrews et al., 1987). The key advance of this theory is to define a "residual" mean meridional circulation, and by doing so isolate the impact of wave forcing into one term, namely the divergence of a quantity $\mathbf{F}$, known as the Eliassen-Palm flux (EP-flux). The EP-flux can be related to physical properties of the waves such as their transience and group velocity. Furthermore, the residual circulation is closely related to the Lagrangian transport of mass and the isentropic circulation. A full development of the TEM theory can be found in Andrews et al. (1987) and here we simply supply the essential results for the quasi-geostrophic beta-plane case, which introduces the key concepts in a simple context. Given the separation of variables into a zonal mean (denoted by brackets) and eddy (denoted by a star) component, e.g., $u = \{u\} + u^*$, one can show

$$\frac{d\{u\}}{dt} - f_0\{v_r\} - \{X\} = \frac{1}{\rho_0}\nabla \cdot \mathbf{F}, \tag{1.1}$$

$$\frac{d\{\theta\}}{dt} + \{w_r\}\frac{d\theta_0}{dz} - \{Q\} = 0, \tag{1.2}$$

$$\frac{d\{v_r\}}{dy} + \frac{1}{\rho_0}\frac{d(\rho_0\{w_r\})}{dz} = 0, \tag{1.3}$$

$$f_0\frac{d\{u\}}{dz} + \frac{1}{H}Re^{-\kappa z/H}\frac{d\{\theta\}}{dy} = 0, \tag{1.4}$$

where

$$\mathbf{F} = \left(0, -\rho_0\{v^*u^*\}, \frac{\rho_0 f_0}{d\theta_0/dz}\{v^*\theta^*\}\right) \tag{1.5}$$

and

$$\{v_r\} = \{v_a\} - \frac{1}{\rho_0}\frac{d}{dz}\left(\frac{\rho_0\{v^*\theta^*\}}{d\theta_0/dz}\right) \tag{1.6}$$

$$\{w_r\} = \{w_a\} + \frac{d}{dy}\left(\frac{\{v^*\theta^*\}}{d\theta_0/dz}\right). \tag{1.7}$$

In the above, v_a and w_a are the ageostrophic meridional and vertical winds, v_r and w_r are the "residual" meridional circulation, θ_0 is a background profile of potential temperature and other notation is standard. As described above, the advantage of writing the equations of motion as above is that the eddy forcing terms $\{v^*u^*\}$ and $\{v^*\theta^*\}$ act only in the particular combination

$$\nabla\cdot\mathbf{F} = -\frac{d}{dy}\left(\rho_0\{v^*u^*\}\right) + \frac{d}{dz}\left(\frac{\rho_0 f_0}{d\theta_0/dz}\{v^*\theta^*\}\right) \tag{1.8}$$

and only on the right hand side of the momentum equation (Eq. 1.1). For the wave-driving of the stratosphere, the vertical component of the EP-flux is typically dominant. Furthermore, the simple meridional heat flux, $\{v^*T^*\}$ is often used as a proxy for the vertical EP-flux (e.g. Newman et al., 2001; Polvani and Waugh, 2004). This will be done in this thesis, and the terms "upward wave activity flux," "upward EP-flux" and "heat flux" will be used interchangeably.

The TEM theory of wave-mean flow interaction has allowed significant advances in the understanding of atmospheric dynamics, including explanations for the maintenance of the tropospheric annular modes (Limpasuvan and Hartmann, 1999), the occurence of SSWs (Limpasuvan et al., 2004) and more generally the dynamical control of temperature in the winter polar stratosphere (Newman et al., 2001), the forcing of the meridional mass circulation in the middle atmosphere (Holton et al., 1995) and the quasi-biennial oscillation in the tropical stratosphere (e.g. Section 8.3 of Andrews et al., 1987). However, the applicability of the TEM theory to observed circulations with strong climatological zonal

asymmetries has received relatively less attention. In the Northern Hemisphere winter, there are strong stationary zonal asymmetries in the atmosphere forced by orography and thermal contrasts between land and ocean. Thus, if we expand variables about a zonally symmetric background state (i.e. $u(t,p,\lambda,\phi) = \{u\}(t,p,\phi) + u^*(t,p,\lambda,\phi)$) we are left with a zonally asymmetric term u^* that consists of a climatological component u^*_c and an anomaly component $u^{*\prime}$ whose contributions to the wave activity flux anomalies can consist of terms linear and quadratic in the wave anomaly. In Section 1.4 a framework will be presented which accounts for this issue by separating variables into climatological and time anomaly components. Chapter 3 will use this theory to quantify the impact of standing and travelling waves on the stratospheric circulation.

In the last part of this section, the practical motivation for understanding the drivers of stratospheric variability and SSWs is presented. To begin with, the temperature structure of the stratosphere is of fundamental importance for ozone chemistry. For example, the polar stratospheric clouds which are an essential part of the heterogenous chemistry reactions that lead to ozone depletion require sufficiently cold temperatures to form (Solomon, 1999). In the Southern Hemisphere, the polar vortex is relatively undisturbed during the winter because of the lack of planetary scale wave forcing. This means that the air inside the polar vortex does not strongly mix with air outside of it, and in combination with the cold temperatures that are reached inside the vortex, this causes significant ozone depletion in the springtime—up to two thirds of historical values (Solomon, 1999). This leads to substantial negative environmental and health consequences at the surface (e.g. Bornman et al., 2011). On the other hand, the stronger wave-driving of the Northern Hemisphere's stratospheric polar vortex typically leads to more mixing, warmer temperatures and less ozone loss. However, there is a significant amount of variability in the dynamical forcing of the Northern Hemisphere stratosphere, and thus some winters, such as the 2010/11 one (Manney et al., 2011), can have substantial amounts of ozone loss in part due to differences in dynamical wave driving (Fusco and Salby, 1999; Randel et al., 2002; Shaw and Perlwitz, 2014).

The impact of stratospheric variability onto the tropospheric circulation is another motivation for understanding the drivers of polar vortex strength changes. There were early studies that suggested an influence on the tropospheric circulation from changes in the strength of the stratospheric polar vortex in the Northern Hemisphere winter using both modelling and observational studies (Boville, 1984; Kodera et al., 1990; Kodera and Koide, 1997). However, it was the work of Baldwin and Dunkerton (1999, 2001) which

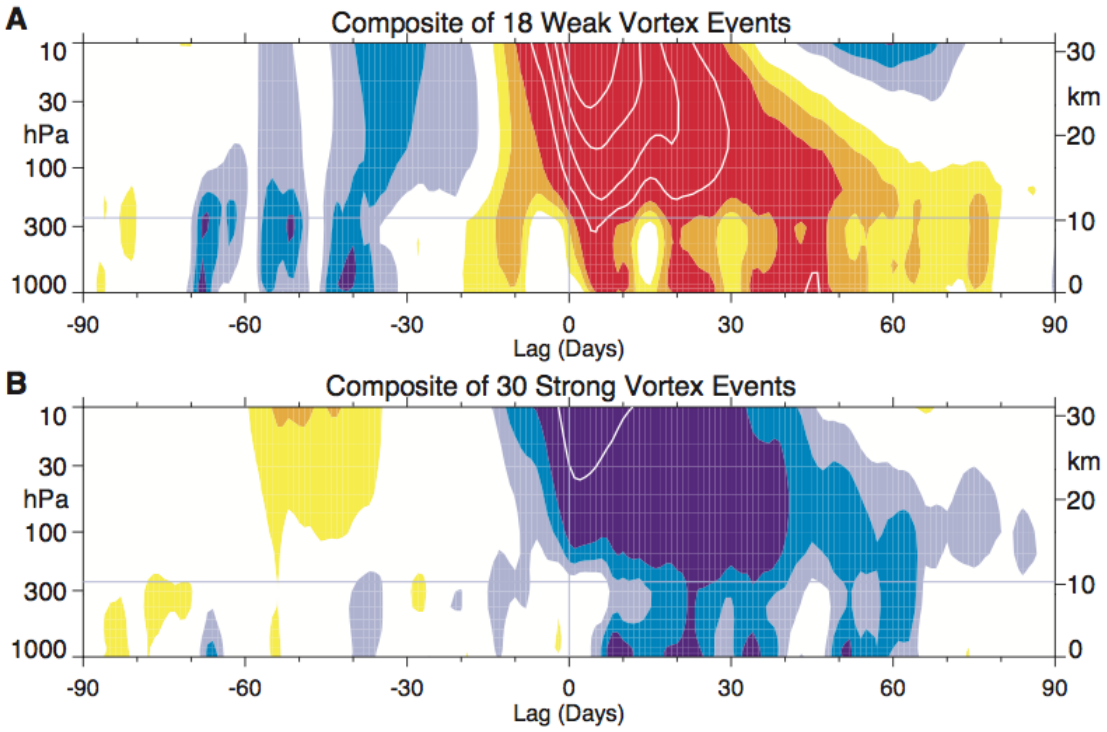

Figure 1.2: Composites of time-height development of the northern annular mode for (A) 18 weak vortex events and (B) 30 strong vortex events. The events are determined by the dates on which the 10-hPa annular mode values cross -3.0 and +1.5, respectively. The indices are nondimensional; the contour interval for the color shading is 0.25, and 0.5 for the white contours. Values between -0.25 and 0.25 are unshaded. The thin horizontal lines indicate the approximate boundary between the troposphere and stratosphere. Reproduced from Baldwin and Dunkerton (2001).

convincingly showed that a strong or weak stratospheric polar vortex in the Northern Hemisphere tends to be followed by, respectively, a poleward or equatorward shifted jet stream in the troposphere. Figure 1.2, reproduced from Baldwin and Dunkerton (2001), plots the composite Northern Annular Mode (NAM) as a function of pressure and lag during extreme stratospheric NAM events. The NAM corresponds to the strength of the polar vortex in the stratosphere, and to the position of the eddy-driven jet in the troposphere (Thompson and Wallace, 2000). Figure 1.2A shows that after an extreme negative NAM signal in the stratosphere, which signifies a weak vortex and is often associated with an SSW event, there is a downward propagation of the NAM anomaly through the stratosphere and an impact on the NAM in the troposphere for 60 days (implying an equatorward shift of the tropospheric jet). A similar sequence of events occurs for extreme positive NAM (strong vortex) events resulting in a persistent poleward shift of the tropospheric jet.

The state of the stratospheric circulation can also impact the troposphere on longer timescales. For example, the historical development and expected future recovery of the ozone hole in the Southern Hemisphere springtime has had an impact on the polarity of the Southern Annular Mode (Gillett and Thompson, 2003; Son et al., 2008). Furthermore, studies with general circulation models have shown that there is a dynamical impact of the strength of the stratospheric polar vortex onto the tropospheric circulation (Polvani and Kushner, 2002; Scaife et al., 2005; Douville, 2009) and that it is important to properly resolve the stratosphere in order to faithfully simulate tropospheric climate both in terms of interannual variability and long-term trends (Shindell et al., 1999; Gerber et al., 2012).

The long-lived persistence of the tropospheric NAM anomalies after extreme events in the stratosphere is suggestive of a potential source of extended time-scale predictability. For example, observations show statistically significant differences in the frequency of occurrence of cold weather extremes after weak and strong stratospheric polar vortex events (Thompson et al., 2002). Furthermore, the state of the NAM in the lower stratosphere is a better predictor of the upcoming monthly-mean surface NAM than the surface NAM itself (Baldwin et al., 2003; Charlton et al., 2003). Recent studies have shown a clear impact of the stratosphere on extended timescale weather predictions with atmospheric models and seasonal forecast systems. Predictions of certain North Atlantic Oscillation (NAO) related variables in a high-top model with good stratospheric representation are significantly better for predictions initialized during or shortly after SSWs versus those initialized when the stratosphere is closer to its climatological state (Sigmond

et al., 2013). Furthermore, the high skill of some recent seasonal hindcasts of the NAO has been claimed to be partially due to a proper representation of the stratosphere and its seasonal responses to the Quasi-Biennial Oscillation (QBO) and the El Niño-Southern Oscillation (Scaife et al., 2014, 2016).

Because of the long-lived impact of changes in the stratospheric circulation on the troposphere, it would be helpful to understand how predictable changes in the stratospheric circulation itself are. This can be considered as either a boundary-value problem or an initial-value problem (Tripathi et al., 2015). For example, external boundary conditions such as the phase of El Niño (Butler and Polvani, 2011), large-scale snow cover anomalies (Cohen et al., 2007) and the phase of the QBO (Holton and Tan, 1980) have been claimed to affect the probability of SSWs.[2] These relatively slow processes can impact the probability of an SSW throughout a winter season, a fact that is useful for seasonal predictions (Scaife et al., 2014, 2016). However, for predictions on the sub-seasonal (i.e. roughly 10 to 60 day) timescale, it is of more interest to make deterministic predictions of the actual timing of a particular SSW event. For example, as discussed above, Sigmond et al. (2013) showed that the significant improvement in skill scores for NAO-related variables was conditional on an SSW event happening in the first place. Thus, the second approach to understanding the predictability of the extratropical stratosphere considers the initial-value problem: how far in advance can a specific SSW be predicted? Some studies have searched for typical precursors to extreme changes in the strength of the polar vortex. For example, blocking events in the troposphere tend to precede SSWs (Quiroz, 1986; Martius et al., 2009), although there are many more blocking events than SSW events (Albers and Birner, 2014). Garfinkel et al. (2010) identified anomalous tropospheric circulation patterns that tend to precede vortex weakening events. They found that precursors tend to be wave anomalies that act to amplify the climatological wavefield. This idea will be referred to as "linear interference" and has been used to understand the drivers of particular SSW events (Nishii et al., 2009), the impact of El Niño (Garfinkel et al., 2010; Fletcher and Kushner, 2011), the Madden-Julian Oscillation (Garfinkel et al., 2012, 2014) and Eurasian snowcover (Smith et al., 2010, 2011; Smith, 2012) on the polar vortex. The primary goal of Chapters 2 and 3 is to understand the structure of the waves responsible for the linear interference driving of the stratospheric polar vortex, motivated by the aim of identifying precursors to SSWs.

[2] Although the QBO is not external to the stratosphere, it can be considered as approximately external to the extratropical stratosphere given that its driving is mainly of tropical origin and given the large separation of timescales between the tropical and extratropical stratospheres.

The next section will introduce and precisely define the linear interference effect.

1.4 Linear interference effects

The linear interference framework is a useful way to understand the variability of upward wave activity flux and the driving of polar vortex events (Nishii et al., 2009; Garfinkel et al., 2010; Smith and Kushner, 2012). This method separates flux anomalies into a contribution that is due to the interference of wave anomalies with the background climatological wave (the LIN term), and another term that is solely due to interactions of the wave anomaly with itself (the NONLIN term). This thesis will focus on meridional eddy heat flux as a proxy for upward wave activity (see Eq. 1.5) as it has been shown that time-integrated heat flux in the lower stratosphere is highly correlated with mid-stratospheric temperatures (Newman et al., 2001) and stratospheric polar vortex strength (Polvani and Waugh, 2004).

Quantitatively, the decomposition into LIN and NONLIN terms is done as follows. Using the expansion of the meridional wind and temperature zonal eddies into their climatological (denoted with a subscript c) and anomaly (denoted with a prime) components, $v^* = v^*_c + v^{*\prime}$ and $T^* = T^*_c + T^{*\prime}$, the total meridional heat flux can be written as

$$\{v^*T^*\} = \{v^*_c T^*_c\} + \{v^{*\prime} T^*_c\} + \{v^*_c T^{*\prime}\} + \{v^{*\prime} T^{*\prime}\}. \tag{1.9}$$

Taking the climatology of Eq. 1.9, and using $(v^{*\prime})_c = 0$ and $(T^{*\prime})_c = 0$, one finds

$$\{v^*T^*\}_c = \{v^*_c T^*_c\} + \{v^{*\prime} T^{*\prime}\}_c. \tag{1.10}$$

Then, subtracting Eq. 1.10 from Eq. 1.9, the anomalous heat flux can be separated into the LIN and NONLIN terms as follows:

$$\begin{aligned} \{v^*T^*\}' =& \{v^*T^*\} - \{v^*T^*\}_c \\ =& \{v^{*\prime} T^*_c\} + \{v^*_c T^{*\prime}\} + \{v^{*\prime} T^{*\prime}\} - \{v^{*\prime} T^{*\prime}\}_c \\ =& \text{LIN} + \text{NONLIN} \end{aligned} \tag{1.11}$$

where

$$\text{LIN} = \{v^{*\prime}T^{*}_{c}\} + \{v^{*}_{c}T^{*\prime}\} \tag{1.12}$$

$$\text{NONLIN} = \{v^{*\prime}T^{*\prime}\} - \{v^{*\prime}T^{*\prime}\}_{c} = \{v^{*\prime}T^{*\prime}\}'. \tag{1.13}$$

As will explicitly be shown in Chapter 4, the LIN term is linear in the wave anomaly amplitude, and its sign is determined by the relative phase of the anomaly and climatology. The NONLIN term is quadratic in the wave anomaly amplitude, and its sign is determined by the tilt of the wave anomaly (positive for westward tilted with height, negative for eastward tilted). The motivation for this decomposition comes from the fact that, as shown in Fig. 1.3, periods of anomalously large and small upward wave activity flux correspond to wave anomalies being in and out of phase with the climatological wave. This suggests that the relative phasing of wave anomalies and the background climatology, which is quantified by the LIN term, is an important determinant of the heat flux anomaly. Smith and Kushner (2012) examined the characteristics of the LIN and NONLIN terms, and their relative roles in initiating stratosphere-troposphere interactions. Their primary conclusions were that the LIN term explains the largest portion of the interannual variability of anomalous heat flux in both hemisphere's winters, and that the LIN term is driven by low-frequency planetary scale (wavenumbers 1 and 2, primarily) waves. Furthermore, the LIN term was shown to be more persistent than either the total heat flux anomaly or the NONLIN term, and this was attributed to the apparent extremely long persistence of the phase of wave-1 anomalies.

A key question of interest outstanding from Smith and Kushner (2012) was whether the LIN term is primarily driven by standing waves with fixed nodes and varying amplitude or travelling waves moving in and out of phase with the climatology. This question is not without precedent, and indeed the ideas behind it were suggested by Holton and Mass (1976) as described in Section 1.1. Clear examples of both behaviours can be seen in nature. In Fig. 1.4 are Hovmöller plots of the wave-1 geopotential height anomalies at 60°N and 100hPa for the winter of 1979-1980, which consisted of persistent westward-propagating wave-1 anomalies, and for the winter of 1990-1991, which was dominated by a large-amplitude standing wave event. Our interest is in how these different wave anomalies interfere with the background climatology, and thus drive fluctuations in the LIN term. The other panels of Fig. 1.4 show the wave-1 component of LIN for each of these winter seasons. The positive and negative periods of LIN correspond to wave-1 anomalies being, respectively, in and out of phase with the wave-1 background climatol-

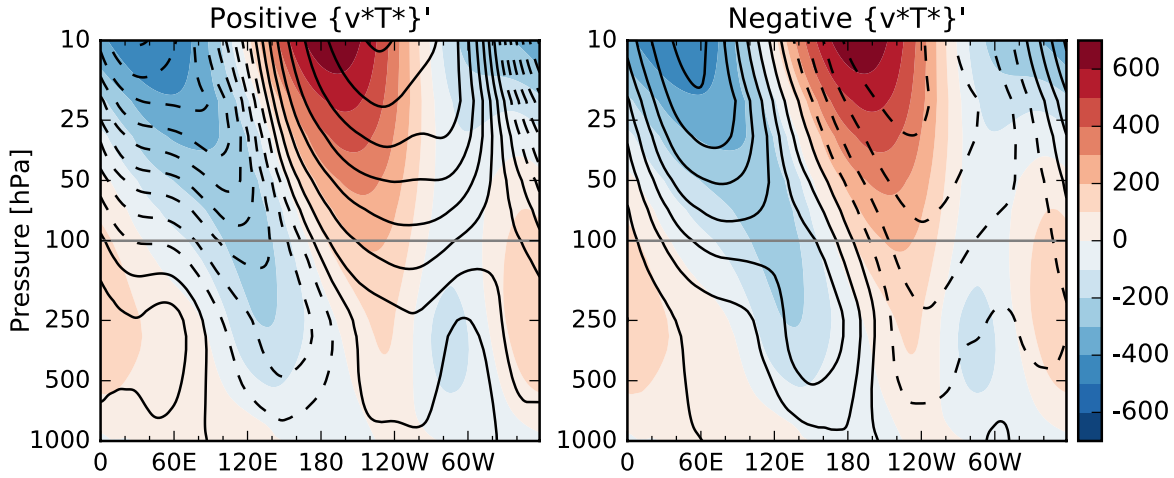

Figure 1.3: Shading: the NDJFM climatological stationary wave Z_c^* at 60°N, in units of m. Contours: the wave anomaly $Z^{*\prime}$ at 60°N, composited over days of anomalously high (left) and low (right) heat flux at 60°N and 100hPa. The particular days selected for compositing are the period of most extreme 10-day averaged poleward heat flux anomaly $\{v^*T^*\}'$ (which is a measure of upward Rossby wave activity flux) over each NDJFM season. The contour line intervals for $Z^{*\prime}$ are 40m with dashed lines negative and solid lines zero or positive.

ogy (the longitudes of the maximum and minimum of the daily wave-1 climatology are indicated by the solid and dashed black lines). A standing-travelling decomposition will allow us to determine whether fluctuations in LIN are being driven primarily by travelling waves of consistent amplitude propagating in and out of phase with the background, or by standing waves fixed in space. Chapter 2 will introduce such a decomposition, and Chapter 3 will apply it to the LIN term.

Smith and Kushner (2012) noted a weak negative covariance between the LIN and NONLIN terms in the Northern Hemisphere winter (their Fig. 2). However, it was found to be only marginally statistically significant, and events of extreme LIN or NONLIN heat flux appeared to largely independent. Nevertheless, Chapter 4 will show that there is actually a nonlinear relationship between these two terms when they are filtered by wavenumber. For example, wave-1 NONLIN has a clear dependence on wave-1 LIN: NONLIN tends to be large and positive for either negative or positive LIN. Explicit expressions for this dependence will be shown for a monochromatic wave in geostrophic and hydrostatic balance, and the implications of it for the distribution of the total heat flux are discussed. In particular, the positive skewness of the heat flux distribution in the lower stratosphere can be explained through this relationship, as the LIN and NONLIN terms tend to cancel each other when LIN is negative, but amplify each other when LIN is positive. A simple model of wave interference is developed to test this idea, and it is shown that the westward tilt of the climatological wave is the key requirement for the

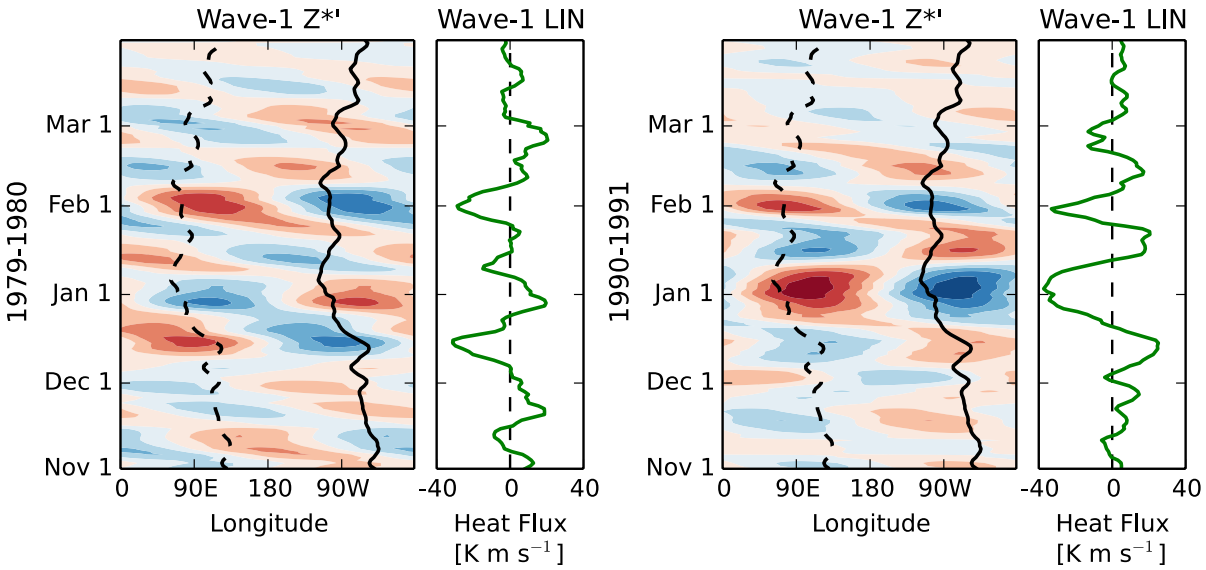

Figure 1.4: Wave-1 $Z^{*\prime}$ and LIN heat flux at 60°N and 100hPa for two NDJFM seasons: left, 1979-1980 and right, 1990-1991. The contour levels for the Hovmöllers are $\pm(0, 100, 200, 300, 400, 500)$m where the reds are positive and blues are negative. The solid and dashed black lines show the daily position of the maximum and minimum of the wave-1 of Z_c^*.

positive skewness of the heat flux anomaly.

1.5 Standing and travelling waves in the troposphere

The Northern Hemisphere's wintertime tropospheric circulation is a complex combination of fast eastward travelling synoptic waves, quasi-stationary ridges and troughs, and, at high latitudes, planetary scale westward travelling waves (e.g. Branstator, 1987). The possible changes under global warming to these dynamical aspects of the atmospheric circulation are in most cases highly uncertain (Shepherd, 2014). Some authors have suggested that Arctic amplification, and hence changes in the equator-to-pole temperature gradient, is or will be responsible for changes in wave amplitudes in the mid-latitudes (Francis and Vavrus, 2012; Cohen et al., 2014), but whether statistically significant changes have actually been observed is disputed (Barnes, 2013; Screen and Simmonds, 2013). Furthermore, the specific drivers of certain mid-latitude weather regimes, such as the ridge-trough pattern which led to persistent cold weather in eastern North America during the winters of 2013/14 and 2014/15, are unclear. The traditional view that anomalies in sea surface temperature in the tropics are the primary cause of seasonal anomalies in the extratropical circulation (Hoskins and Karoly, 1981; Trenberth et al.,

1998) has been suggested by some to help explain recent extreme North American winters (Wang et al., 2014; Hartmann, 2015), but other authors have not found a strong connection between tropical anomalies and the pattern of cold temperatures of 2013/14 and 2014/15 (Sigmond and Fyfe, 2016). The possibility of Arctic warming and reduced sea-ice driving mid-latitude cooling over North America has also been suggested (Lee et al., 2015; Kug et al., 2015).

Given the disparate mechanisms proposed to explain cold weather extremes over eastern North America, and the general uncertainty about future trends in wave amplitudes, in Chapter 5 the standing-travelling wave decomposition will be applied to the mid-tropospheric atmospheric circulation. Using this novel spectral decomposition provides new insights into the causes of cold winter weather over eastern North America. In addition, the decomposition may provide a useful tool for understanding possible future changes in wave amplitudes or phase speeds. Typically, separating the quasi-stationary and transient components of the atmospheric circulation has been done with band-pass filtering (Blackmon, 1976; Hoskins and Valdes, 1990). However, this necessitates the use of arbitrarily defined limits of high- and low-frequency variability, and requires additional analysis to distinguish between eastward and westward travelling disturbances. The standing-travelling wave decomposition will be used here as an alternative method to separate the quasi-stationary and transient components of the flow. This will avoid building in assumptions about characteristic length and time scales.

Stationary waves in the atmosphere are known to be driven by zonal asymmetries at the surface such as topography (Charney and Eliassen, 1949), the thermal contrasts between land and ocean (Smagorinsky, 1953) and forcing from transient eddies (Lau and Holopainen, 1984). However, because of variability in both the background flow (which will affect the structure of the stationary waves) and of the forcing mechanisms themselves, it is natural to expect some sub-seasonal variability in the stationary/quasi-stationary wave field. Thus, while the seasonal or climatological mean of the eddy geopotential height field is often taken as the quasi-stationary component driven by topography and thermal forcing, the standing-travelling algorithm used in Chapter 5 additionally includes in the standing component subseasonal timescale variations which could be related to variability in the thermal forcing, orographic forcing, and non-linear interactions between the mean field and the external forcing.

1.6 Conclusion

This thesis presents a novel spectral decomposition of atmospheric variability into standing and travelling waves and uses this to make advances in three areas of atmospheric dynamics. In particular, this thesis addresses 1) the structure of waves that drive upward wave activity flux and hence changes in stratospheric polar vortex strength, 2) the cause of the positive skewness of upward wave activity flux in the lower stratosphere, and 3) the relative roles of standing and travelling waves in causing cold weather extremes in central eastern North America.

The method for separating atmospheric disturbances into standing and travelling components, based on a two-dimensional Fourier transform, is an improvement on previous techniques because it explicitly calculates the covariance between the two wave types. Furthermore, it preserves phase information, and because of this it is straightforward to compute the real space standing and travelling wave fields. Chapter 2 applies this method to geopotential height anomalies in the Northern Hemisphere winter, and shows that although standing waves typically dominate for lower wavenumbers and frequencies, there are well defined travelling modes such as a westward travelling wave-1 feature with a period of approximately 20-25 days. The distinct vertical structures of the standing and travelling waves are described. Furthermore, it is shown that the wave-1 standing wave has preferred longitudes for its antinodes, and these tend to be fairly well aligned with the extremes of the climatological wave. This suggests that the standing waves are primarily driving amplifications or attenuations of the climatological wave, and thus should be efficient drivers of the LIN heat flux.

Chapter 3 quantifies the relative roles of standing and travelling waves in driving variability of the LIN heat flux during the Northern Hemisphere winter season. It is found that standing waves drive a larger portion of the variance of LIN, and are particularly dominant on monthly versus daily timescales. The standing portion of the LIN term is shown to be the most persistent part of the heat flux anomaly, and as such it is suggested to be most important for driving changes in the strength of the stratospheric polar vortex. This is tested by computing lag-correlations between various components of the heat flux anomaly and the NAM. It is shown that the standing part of the LIN term shows a clear time-lagged relationship between heat flux in the troposphere and stratospheric polar vortex strength. Furthermore, it is shown that this part of the heat flux is the largest part of the total heat flux signal that precedes displacement SSWs, while the NONLIN

term is more important for split SSWs. The simulation of the heat flux-NAM connection in two general circulation models is documented.

Next, Chapter 4 demonstrates that there is a previously undocumented relationship between the LIN and NONLIN terms when they are examined by individual wavenumber. It is shown that this is a way to explain the positive skewness of the heat flux distribution in the lower stratosphere, since the two terms will tend to reinforce each other when LIN is positive, but cancel each other out when LIN is negative. A simple statistical model of wave interference is constructed to test this idea, and it is shown that a westward tilted stationary wave is the key ingredient needed to get a positively skewed upward wave activity flux distribution. The implications for the possible dynamical control of the non-Gaussianity of the temperature distribution in the polar stratosphere are discussed.

Finally, Chapter 5 returns to the standing-travelling wave decomposition, but in this case applies it to tropospheric variability. The general characteristics of standing, eastward travelling and westward travelling waves in the Northern Hemisphere winter mid-tropospheric height field are documented. It is shown that standing waves are responsible for classical teleconnections such as the Pacific/North America pattern (Wallace and Gutzler, 1981), while eastward travelling waves have their peaks in variance in the storm track regions (Hoskins and Valdes, 1990). Next, a focus is made on the ridge-trough circulation pattern that brought cold air to eastern North America during the "polar vortex" winters of 2013/14 and 2014/15. It is shown that the North American ridge-trough pattern is largely controlled by standing waves of subtropical origin that can be be rapidly modulated by eastward travelling synoptic waves. The decomposition reveals distinctive temporal signatures for different cold extreme events. In particular, the major cold air outbreak of early January 2014 was driven by an eastward travelling synoptic wave of extremely large amplitude rapidly intensifying a season-long anomalous strengthening of the North American ridge-trough mid-tropospheric flow. On the other hand, the cold anomalies of February 2015 were largely driven by the standing component, and relatedly were more persistent. No statistically significant long-term trend is seen in either the standing or eastward travelling wave components of the ridge-trough pattern over eastern North America.

Nearly all of the material in this thesis is either published or under preparation for submission. Chapter 2, with the exception of Section 2.3.7, and with additional introduction material from Sections 1.2 and 1.4, was published in the Journal of the Atmospheric Sciences (Watt-Meyer and Kushner, 2015a). Chapter 3, with the addition

of some introductory material from Sections 1.1 and 1.4, was published in the Journal of Climate (Watt-Meyer and Kushner, 2015b). Chapters 4 and 5 are in preparation for submission.

Chapter 2

A spectral decomposition of atmospheric disturbances into standing and travelling waves

2.1 Introduction

In this chapter, we propose a simple decomposition of the wavenumber-frequency spectrum into standing and travelling parts, calculate analytic expressions for the variance of each component and their covariance, and show how the decomposition can be used to reconstruct standing and travelling wave fields. While the techniques we describe are quite general, as introduced in Section 1.4, we were motivated to carry out this analysis by particular issues related to wave-driven stratosphere-troposphere coupling in the Northern Hemisphere extratropics (Baldwin and Dunkerton, 2001; Garfinkel et al., 2010; Shaw et al., 2010; Smith and Kushner, 2012). Thus the technique is applied to geopotential height anomalies in the Northern Hemisphere winter and the focus is on the planetary scales (zonal wavenumbers 1 and 2).

Computations of standing and travelling wave decompositions of the extratropical circulation have to a large extent relied on the methods of Hayashi (1977, 1979) and Pratt (1976). These methods were summarized in the textbook by von Storch and Zwiers (1999). For example, Fraedrich and Böttger (1978) decompose the spectrum of geopotential heights at 500hPa and 50°N into standing and travelling parts using a method that combines the techniques of Pratt and Hayashi. Their focus is on higher wavenum-

ber and frequency disturbances, where the authors observe several distinct peaks in the spectrum. The authors suggest that differing types of baroclinic instability—associated with dry versus moist static stability—could be responsible for these separate peaks. Speth and Madden (1983), using the Hayashi (1977) method, highlight and investigate in more detail the presence of a high-latitude 15- to 30-day period westward travelling wave-1 feature. Using the meridional and vertical structure of the feature's amplitude as evidence, the authors attribute it to a manifestation of the theoretically predicted 16-day wave (Haurwitz, 1940; Madden, 1979). Other studies have used Hayashi and Pratt's methods to determine whether the Madden-Julian Oscillation is primarily a standing or propagating pattern (Zhang and Hendon, 1997); to analyze the atmospheric variability in general circulation models and its dependence on the El Niño-Southern Oscillation (May, 1999); and to quantify mid-latitude tropospheric variability, and possible changes to it under global warming scenarios, in the Coupled Model Intercomparison Project phase 3 (Lucarini et al., 2007) and phase 5 (Di Biagio et al., 2014) model ensembles.

These examples show the potentially wide applicability of standing-travelling wave decompositions. We will show that the previously used decomposition methods, however, do not explicitly account for the lack of uniqueness of these decompositions or for the non-orthogonality of the resulting wave fields. These shortcomings and their implications will be addressed in this chapter, which is structured as follows. Section 2.2 will outline the proposed standing-travelling decomposition, describe some simple analytical results, outline previously defined techniques and describe the data to which we apply the analysis technique. Section 2.3 will show the results of applying the method to Northern Hemisphere geopotential height anomalies, including a detailed comparison with previous approaches and an overview of the climatological wavenumber-frequency spectra in the extratropics. To investigate planetary-wave interference effects, we will compare the structure of the standing waves and the climatological wave field. Lastly, we will compute the vertical and time-lagged coherences of the standing and travelling waves at selected Northern Hemisphere extratropical locations using correlation-coherence analysis (Randel, 1987). Section 2.4 will summarize the results and discuss implications for stratosphere-troposphere coupling.

Although not related to stratosphere-troposphere coupling, in Section 2.3.7 the standing-travelling wave decomposition will be applied to convectively-coupled equatorial waves. The analysis will be used on outgoing longwave radiation between 15°S and 15°N, as an exploratory extension of the previous work of Wheeler and Kiladis (1999).

The possibility of using the standing-travelling decomposition to isolate wave modes will be discussed.

2.2 Theory and data

2.2.1 Standing-travelling wave decomposition

This section describes our proposed decomposition of the wavenumber-frequency spectrum into standing and travelling parts. To begin, given some longitude- and time-dependent variable $q(\lambda, t)$, with daily frequency over a period of time of length T days and defined at N equally spaced points in longitude, the discrete 2D Fourier transform is computed as

$$\hat{q}_{k,j} = \sum_{n=0}^{N-1} \sum_{t=0}^{T-1} e^{-ik\lambda_n - i\omega_j t} q(\lambda_n, t) \tag{2.1}$$

where $\lambda_n = \frac{2\pi n}{N}$ and $\omega_j = \frac{2\pi j}{T}$, defined for $k = 0, \ldots, N-1$ (k is the planetary wavenumber) and $j = 0, \ldots, T-1$ (j is an integer index that corresponds to the frequency ω_j). For simplicity, $q(\lambda, t)$ is assumed to have zero zonal and time mean, and N and T are assumed to be odd. Given that $q(\lambda, t)$ is real, as shown in Appendix A.1, one can write the inverse transform as

$$q(\lambda, t) = \frac{2}{NT} \sum_{k=1}^{N_2} \sum_{j=1}^{T_2} q_{k,\pm j}(\lambda, t) \tag{2.2}$$

where $N_2 = (N-1)/2$, $T_2 = (T-1)/2$ and

$$\begin{aligned} q_{k,\pm j}(\lambda, t) = {} & Q_{k,j} \cos\left(k\lambda + \omega_j t + \phi_{k,j}\right) \\ & + Q_{k,-j} \cos\left(k\lambda - \omega_j t + \phi_{k,-j}\right) \end{aligned} \tag{2.3}$$

where we have used $\omega_{-j} = -\omega_j$ and where $Q_{k,j}$ and $\phi_{k,j}$ are the amplitude and phase of $\hat{q}_{k,j}$. That is, $\hat{q}_{k,j} = Q_{k,j} e^{i\phi_{k,j}}$, with $Q_{k,j}$ real and positive and $-\pi < \phi_{k,j} \leq \pi$.

We now decompose the amplitudes $Q_{k,j}$ in Eq. 2.3 in order to express $q(\lambda, t)$ as a combination of standing and travelling waves at each wavenumber and frequency. Using the fact that a pure standing wave consists of two travelling waves of equal amplitude and phase speed moving in opposite directions, we define standing and travelling amplitudes

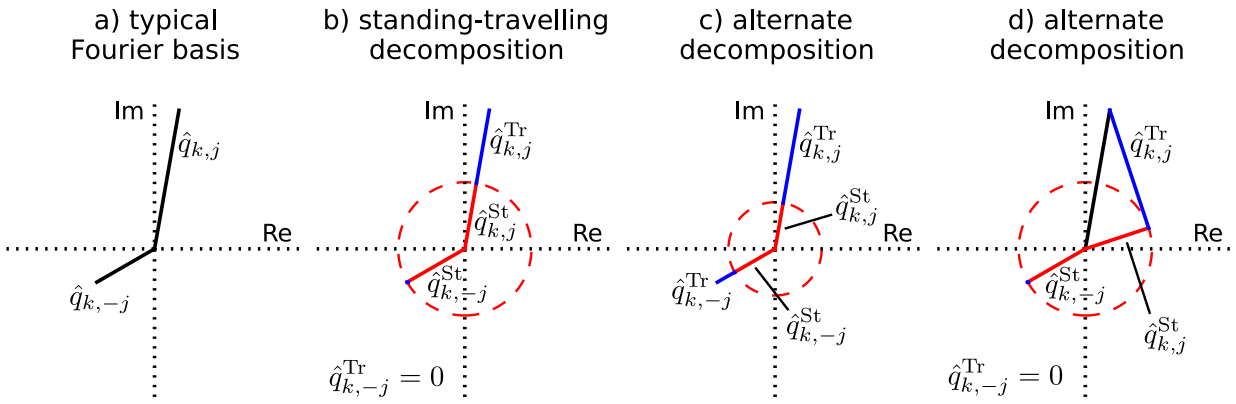

Figure 2.1: Different possible decompositions of two Fourier coefficients into standing and travelling components. a) Two arbitrary Fourier coefficients (see Eq. 2.1) corresponding to the same wavenumber and opposite frequencies, plotted on the complex plane. b) Decomposition of these two coefficients into standing (red) and travelling (blue) parts as implemented in this chapter, following Eq. 2.4. c) An alternate decomposition in which there are travelling waves propagating in both directions. d) An alternate decomposition in which the phases of the standing and travelling components are allowed to differ from the phase of the total Fourier coefficient. In all cases, the standing wave amplitude is equal for $+j$ and $-j$.

as

$$Q^{\mathrm{St}}_{k,j} = \min(Q_{k,j}, Q_{k,-j}) \tag{2.4a}$$

$$Q^{\mathrm{Tr}}_{k,j} = Q_{k,j} - Q^{\mathrm{St}}_{k,j} \tag{2.4b}$$

recalling that $Q_{k,j} \geq 0$ and noting that these definitions imply that $Q^{\mathrm{St}}_{k,j} = Q^{\mathrm{St}}_{k,-j}$ and that either $Q^{\mathrm{Tr}}_{k,j} = 0$ or $Q^{\mathrm{Tr}}_{k,-j} = 0$. Furthermore, we have that $Q^{\mathrm{St}}_{k,j}$ and $Q^{\mathrm{Tr}}_{k,j}$ are real and non-negative. The phases of the standing and travelling components are set to be equal to the original Fourier coefficient phases, that is, $\phi^{\mathrm{St}}_{k,j} = \phi^{\mathrm{Tr}}_{k,j} = \phi_{k,j}$. A phasor representation in the complex plane of this decomposition of two Fourier coefficients $\hat{q}_{k,\pm j}$ into standing and travelling components is given in Figs. 2.1a-b. Alternative decompositions shown in Figs. 2.1c-d will be described in Section 2.2.2. Note that although we define the standing waves amplitude for both positive and negative frequencies, since our definition ensures the standing wave power is symmetric with respect to frequency, we could equivalently consider a "one-sided" spectrum for the standing wave, as in some previous works (e.g. Fraedrich and Böttger, 1978).

One of the main uses of the Fourier transform is to decompose the total variance of a signal into contributions from different wavenumbers and frequencies. From Parseval's

theorem, written here using the same assumptions on $q(\lambda, t)$ as above, we have

$$\sum_{n=0}^{N-1}\sum_{t=0}^{T-1}\left[q(\lambda_n, t)\right]^2 = \frac{2}{NT}\sum_{k=1}^{N_2}\sum_{j=-T_2}^{T_2}(Q_{k,j})^2. \tag{2.5}$$

Furthermore, from Eq. 2.4b, we have

$$(Q_{k,j})^2 = \left(Q_{k,j}^{\mathrm{St}}\right)^2 + \left(Q_{k,j}^{\mathrm{Tr}}\right)^2 + 2Q_{k,j}^{\mathrm{St}}Q_{k,j}^{\mathrm{Tr}}. \tag{2.6}$$

Thus, the variance of the signal $q(\lambda, t)$ is decomposed at each wavenumber and frequency into a standing part, a travelling part, and a term which represents the covariance between the two parts. Note that since $Q_{k,j}^{\mathrm{St}}$ and $Q_{k,j}^{\mathrm{Tr}}$ are greater than or equal to zero, the covariance term is always non-negative. This is to be expected: since in the definition of the standing and travelling parts of the signal we maintain the same phases $\phi_{k,j}$, the travelling wave will always positively correlate with one of the components of the standing wave.

In our decomposition the standing waves have an easily defined structure. At each wavenumber and pair of frequencies, the standing wave can be written as

$$\begin{aligned} q_{k,\pm j}^{\mathrm{St}}(\lambda, t) &= \frac{2}{NT}Q_{k,j}^{\mathrm{St}}\cos\left(k\lambda + \omega_j t + \phi_{k,j}\right) \\ &\quad + \frac{2}{NT}Q_{k,-j}^{\mathrm{St}}\cos\left(k\lambda - \omega_j t + \phi_{k,-j}\right) \\ &= \frac{4}{NT}Q_{k,j}^{St}\cos\left(k\lambda + \overline{\phi}_{k,j}\right)\cos\left(\omega_j t + \Delta\phi_{k,j}\right) \end{aligned} \tag{2.7}$$

where

$$\overline{\phi}_{k,j} = \frac{1}{2}(\phi_{k,j} + \phi_{k,-j}),\ \Delta\phi_{k,j} = \frac{1}{2}(\phi_{k,j} - \phi_{k,-j}). \tag{2.8}$$

Thus the standing wave corresponding to the wavenumber-frequency pair $(k, \omega_{\pm j})$ will have its crests and troughs at longitudes of $\lambda = \frac{1}{k}(\pi m - \overline{\phi}_{k,j})$ where m is an integer. It is shown in Appendix A.2 that $\overline{\phi}_{k,j}$ gives the same result for the positions of antinodes as the formula given by Hayashi, e.g. Eq. 4.5 in Hayashi (1977).

We are also interested in examining the typical behaviour of standing and travelling waves consisting of more than one frequency, across one or more seasons. To this end, we compute the variance over time of $q_k(\lambda, t) = \frac{2}{NT}\sum_{j=1}^{T_2} q_{k,\pm j}(\lambda, t)$. As demonstrated in

Appendix A.3, using the orthogonality of the cosine basis functions, one can show that

$$\begin{aligned}\mathrm{var}[q_k](\lambda) &= \frac{1}{T}\sum_{t=0}^{T-1}\left(q_k(\lambda,t)\right)^2 \\ &= \frac{2}{N^2T^2}\sum_{j=-T_2}^{T_2}\{Q_{k,j}^2 \\ &\quad + 2Q_{k,j}Q_{k,-j}\cos^2(k\lambda+\overline{\phi}_{k,j}) - Q_{k,j}Q_{k,-j}\}\end{aligned} \tag{2.9}$$

where $\overline{\phi}_{k,j}$ was defined in Eq. 2.8. If the signal $q_k(\lambda,t)$ is the sum of pure standing waves (i.e. $Q_{k,j}=Q_{k,-j}$) then Eq. 2.9 simplifies to:

$$\mathrm{var}[q_k^{\mathrm{St}}](\lambda) = \frac{4}{N^2T^2}\sum_{j=-T_2}^{T_2} Q_{k,j}^2\cos^2(k\lambda+\overline{\phi}_{k,j}). \tag{2.10}$$

On the other hand, if our signal is the sum of pure travelling waves (i.e. either $Q_{k,j}=0$ or $Q_{k,-j}=0$ for every j; that is, $Q_{k,j}Q_{k,-j}=0$) then Eq. 2.9 simplifies to:

$$\mathrm{var}[q_k^{\mathrm{Tr}}](\lambda) = \frac{2}{N^2T^2}\sum_{j=-T_2}^{T_2} Q_{k,j}^2. \tag{2.11}$$

2.2.2 Alternate decompositions

Because the standing and travelling waves at the same wavenumber and frequency are not orthogonal, the decomposition defined in Eq. 2.4 is not unique. For example, one could assign less amplitude to the standing wave, and have travelling waves moving in both directions at each absolute frequency, as in Hayashi (1977). An example of this is shown in Fig. 2.1c. Furthermore, if one allows for the phases of the standing and travelling components to be different, this allows another set of possibilities for the decomposition, an example of which is shown in Fig. 2.1d. Nevertheless, we argue that our choice defined in Eq. 2.4 is a natural decomposition to work with for a number of reasons. First, we reject the possibility of having travelling waves moving in both directions at the same wavenumber and phase speed, as in Fig. 2.1c, since these will just add up to an additional standing wave at this frequency. Second, we choose to keep the same phases for the standing and travelling components, because this is the simplest choice, and because it ensures that the standing and travelling parts of the signal each have the maximum correlation with the total signal.

Note that if we allow the phases of the standing and travelling components to vary, as in Fig. 2.1d, the covariance can also be negative or zero. In particular, assuming only that $\hat{q}_{k,j} = \hat{q}^{\mathrm{St}}_{k,j} + \hat{q}^{\mathrm{Tr}}_{k,j}$ we can generalize Eq. 2.6 to

$$(Q_{k,j})^2 = \left(Q^{\mathrm{St}}_{k,j}\right)^2 + \left(Q^{\mathrm{Tr}}_{k,j}\right)^2 + 2Q^{\mathrm{St}}_{k,j}Q^{\mathrm{Tr}}_{k,j}\cos(\phi^{\mathrm{St}}_{k,j} - \phi^{\mathrm{Tr}}_{k,j}). \tag{2.12}$$

When $\phi^{\mathrm{St}}_{k,j} = \phi^{\mathrm{Tr}}_{k,j}$ as before, we recover Eq. 2.6 and the covariance is strictly positive. However, it is also possible to force $\phi^{\mathrm{St}}_{k,j} - \phi^{\mathrm{Tr}}_{k,j} = \pm\frac{\pi}{2}$ (one of these cases is illustrated in Fig. 2.1d) in which case the covariance will be zero. Nevertheless, the $\phi^{\mathrm{St}}_{k,j} = \phi^{\mathrm{Tr}}_{k,j}$ case is the most intuitive decomposition because it maximizes the correlation between each of the standing and travelling components and the total signal. This follows from the fact that the Fourier coefficients for the standing and travelling waves are parallel to the total coefficient in the complex plane (as in Fig. 2.1b).

As far as we are aware, all standing-travelling decompositions discussed in the literature (Hayashi, 1973, 1977, 1979; Pratt, 1976) do not explicitly account for the covariance term between standing and travelling waves. The authors generally take it as an assumption that the standing and travelling waves will be independent, although they do recognize that this is not always actually the case. In particular, they require that, written in our notation, either $(Q_{k,j})^2 = (Q^{\mathrm{St}}_{k,j})^2 + (Q^{\mathrm{Tr}}_{k,j})^2 + \text{noise}$ (Pratt, 1976) or $(Q_{k,j})^2 = (Q^{\mathrm{St}}_{k,j})^2 + (Q^{\mathrm{Tr}}_{k,j})^2$ (Hayashi, 1977) without any explicit representation of covariance between the standing and travelling parts of the signal.

We thus identify two distinct advances arising from our technique. First, we can precisely account for and calculate the often significant contribution from the joint variability of standing and travelling waves. Second, it is also straightforward to reconstruct the real-space standing and travelling parts of the signal,[1] something that is not simple to do with the other techniques.

2.2.3 Other techniques

Some previous techniques for computing the wavenumber-frequency spectrum, starting with Hayashi (1971), take a somewhat different approach than what we have described above. They begin by computing a spatial Fourier transform of $q(\lambda, t)$ at each timestep, and defining $c_k(t)$ and $s_k(t)$ as the timeseries for the cosine and sine coefficients at

[1] To do this, simply use the inverse transform given in Eqs. 2.2 and 2.3 with the standing or travelling amplitudes, $Q^{\mathrm{St}}_{k,j}$ or $Q^{\mathrm{Tr}}_{k,j}$, instead of the total amplitude $Q_{k,j}$.

wavenumber k (again we are assuming the zonal mean of q is zero):

$$q(\lambda, t) = \sum_{k=1}^{N} \{c_k(t)\cos(k\lambda) + s_k(t)\sin(k\lambda)\}. \tag{2.13}$$

The wavenumber-frequency spectrum is then defined as (see also von Storch and Zwiers, 1999)

$$P_{k,\omega}[q] = \frac{P_\omega[c_k] + P_\omega[s_k]}{2} + Q_\omega[c_k, s_k], \tag{2.14}$$

where $P_\omega[c_k]$ and $P_\omega[s_k]$ are the power spectra of $c_k(t)$ and $s_k(t)$ respectively, and $Q_\omega[c_k, s_k]$ is the quadrature spectrum (i.e. imaginary part of the cross spectrum) between the two. Note that, as shown by Tsay (1974), $P_{k,\omega}[q]$ is equal to the 2D Fourier amplitudes squared, $|\hat{q}_{k,\omega_j}|^2$, where $\hat{q}_{k,\omega_j}$ was defined in Equation 2.1.

Pratt (1976) and Hayashi (1977) define the standing wave variance as

$$P^{\mathrm{St}}_{k,\omega}[q] = \sqrt{\frac{1}{4}\left(P_\omega[c_k] - P_\omega[s_k]\right)^2 + K^2_\omega[c_k, s_k]} \tag{2.15}$$

where $K_\omega[c_k, s_k]$ is the co-spectrum between $c_k(t)$ and $s_k(t)$.

Pratt and Hayashi differ in how they define the propagating part of the variance. Pratt defines the travelling variance as the difference between the eastward and westward components, or,

$$P^{\mathrm{Tr}}_{k,\omega}[q] = 2|Q_\omega[c_k, s_k]|. \tag{2.16}$$

The direction of propagation is defined by whether $P_{k,\omega}$ or $P_{k,-\omega}$ is greater. By Pratt's definition, there is no guarantee that the standing and propagating components of the variance add up to the total wavenumber-frequency spectrum. Hayashi, on the other hand, simply defines the propagating variance as the total wavenumber-frequency spectrum minus the standing portion (e.g. Eq. 5.9 in Hayashi (1977)). However, this can lead to negative powers for the propagating variance, since the standing wave variance as defined in Eq. 2.15 can sometimes be larger than the total wavenumber-frequency spectrum. Hayashi states this is most often an issue when there is insufficient smoothing in the frequency domain. There are two main differences between our technique and those of Pratt and Hayashi. First, we make no assumption about the independence of the travelling and standing waves, unlike the previous authors (e.g. see Section 5 of Hayashi, 1977). Second, our decomposition is based on the 2D Fourier coefficients themselves, as opposed to the power, co- and quadrature spectra as in Eqs. 2.15 and 2.16.

We point out that there is some confusion in the literature about the Pratt and Hayashi techniques. von Storch and Zwiers (1999) correctly describe how Pratt defines the travelling wave variance (Eq. 2.16) but incorrectly state that Pratt defines the standing variance as the remainder of the total. This is actually how Fraedrich and Böttger (1978) explain the standing-travelling decomposition, effectively mixing the Pratt and Hayashi techniques. In Section 2.3.1 we will briefly compare results for the standing-travelling decomposition as we define it, and using the two methods described in von Storch and Zwiers (1999).

2.2.4 Data and notation

We apply the analysis technique to 1979 to 2013 daily mean geopotential height from the ERA-Interim reanalysis (Dee et al., 2011). The data is on a $1.5^\circ \times 1.5^\circ$ latitude-longitude grid, on 37 vertical levels ranging from 1000hPa to 1hPa. We first remove the zonal mean and the daily climatology, which is computed by averaging each calendar day over all 35 years of the dataset. We use a superscript asterisk to denote the deviation from the zonal mean and a prime to denote the climatological anomaly:

$$Z^* = Z - \{Z\}, \qquad Z' = Z - Z_c \tag{2.17}$$

where $\{Z\}$ and Z_c are the zonal and daily climatological means of Z respectively.

The spectral analysis is then applied to $Z^{*\prime}$ separately at each latitude and pressure level, on 151-day periods starting November 1 of each year (thus on non leap-years, the period is from November 1 to March 31, and on leap years it is until March 30). Note that before applying the spectral analysis, we linearly detrend and remove the time-mean from the data over each winter period, as in Wheeler and Kiladis (1999). This does not have a major impact on our results since we have already removed the climatology. Although we compute the spectral decompositions independently at each latitude and pressure, in Section 2.3.6 we will use the statistical method of Randel (1987) to examine aspects of the wave structures' spatial and temporally-lagged coherence.

Following Randel and Held (1991) we use a normalized Gaussian spectral window of the form

$$W(\omega_j - \omega_{j_0}) \propto e^{-[(j-j_0)/\Delta j]^2} \tag{2.18}$$

to smooth the power spectra about the frequency ω_{j_0}. Here, $W(\omega_j - \omega_{j_0})$ is the weight

given to the spectrum at frequency ω_j for computing the smoothed power at frequency ω_{j_0}. The Δj is the width of the Gaussian window in terms of the frequency index, which we take to be $\Delta j = 1.5$. We are able to have a higher spectral resolution (smaller Δj) than Randel and Held (1991) because we are averaging our spectra over 34 winter seasons, as opposed to only seven.

Note that we apply the smoothing directly to each of the three terms on the right hand side of Eq. 2.6, after having made the standing-travelling decomposition. This is in contrast to Hayashi and Pratt, who compute smoothed spectra before making the standing and travelling decomposition (Pratt, 1976). For comparison, we will also show some results in Section 2.3.1 where we smooth the wavenumber-frequency spectrum before making the decomposition into standing and travelling parts. For our method, this is slightly more involved because our decomposition is actually based on the amplitudes, not the amplitudes squared. Thus, to make the cleanest possible comparison with Hayashi and Pratt in Section 2.3.1, we square the amplitudes, then smooth, and then take the square root to get smoothed amplitudes, upon which we apply the decomposition into standing and travelling components following Eq. 2.4. Finally, we point out that we only smooth the spectra for display, for example in Fig. 2.4, but not when reconstructing the standing and travelling signals $q^{\mathrm{St}}(\lambda, t)$ and $q^{\mathrm{Tr}}(\lambda, t)$.

2.3 Results

2.3.1 Methods comparison

We begin by showing the various steps taken to compute the final, smoothed, wavenumber-frequency spectra, including the decomposition into standing and travelling waves. We show all the steps for the wave-1 component of $Z^{*\prime}$ for the 1979-1980 year, which will be shown in Fig. 2.3. For comparison, we will also show the standing-travelling decomposition as computed by following the methods of Hayashi and Pratt, and by a version of our method that is more consistent with the Hayashi and Pratt methods.

Figure 2.2a shows the normalized[2] wave-1 component of the raw wavenumber-frequency spectrum, i.e. $\frac{2}{N^2T}(Z_{k,j})^2$. Since we are showing results specific for geopotential heights, we write $Z_{k,j}$ here instead of $Q_{k,j}$ as in Section 2.2. The zero-frequency

[2]The normalization is chosen such that summing the spectrum over positive wavenumbers and integrating over all frequencies will recover the total time-longitude variance of the original signal.

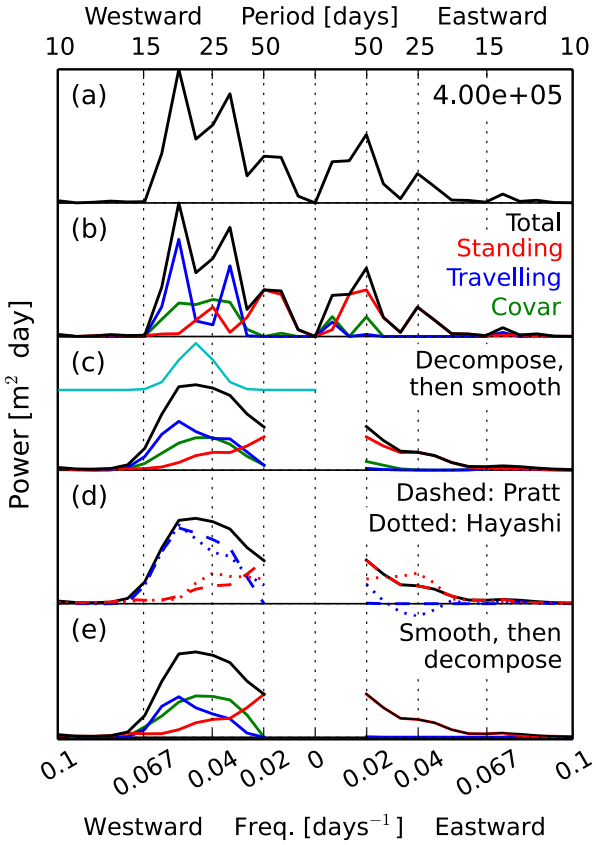

Figure 2.2: Different versions of the wave-1 component of the wavenumber-frequency spectrum of ND-JFM 1979-1980 $Z^{*\prime}$ at 60°N and 100hPa. (a) Unsmoothed wavenumber-frequency spectrum normalized such that integrating over frequency will give the wave-1 variance (i.e. we plot $\frac{2}{N^2 T} Z^2_{k,j}$). The number in the top-right corner gives the maximum value achieved by the spectrum over all frequencies in units of $\mathrm{m}^2 \cdot \mathrm{day}$. (b) Decomposition of the unsmoothed spectrum into standing (red), travelling (blue) and covariance (green) terms according to Eq. 2.6. (c) Spectra from (b) smoothed with a gaussian window, which is shown by the thin cyan line (see Eq. 2.18; width is $\Delta j = 1.5$). (d) Decompositions of the smoothed wavenumber-frequency spectrum into standing (red) and travelling (blue) components according to Pratt (1976) (dashed) and Hayashi (1977) (dotted). (e) Decomposition of the smoothed wavenumber-frequency spectrum into standing, travelling and covariance components using our method (as opposed to (c), here the smoothing is performed before the standing-travelling decomposition; see discussion in Section 2.2.4). For the smoothed spectra, we only plot the well-resolved frequencies. Note all spectra are plotted on the same scale, indicated in (a).

component is plotted at the centre of the figure, with westward moving waves (positive ω_j in Eq. 2.2) on the left side and eastward moving waves (negative ω_j) on the right side. The absolute value of frequency increases moving away from the centre of the figure, and we omit the frequencies higher than 0.1 days^{-1} since they contain negligible power for this year, latitude and pressure level. Note that the zero-frequency component has zero amplitude because we have removed the time-mean before computing the spectrum. Furthermore, the westward power is generally higher than the eastward power, indicative of a prominent westward travelling wave.

Next, the decomposition into standing and travelling components is made based on the Fourier amplitudes (which are not shown) using Eq. 2.4. In Fig. 2.2b we replot the total amplitudes squared, and also show the three terms in Eq. 2.6: the standing variance $(Z^{\mathrm{St}}_{k,j})^2$ in red, the travelling variance $(Z^{\mathrm{Tr}}_{k,j})^2$ in blue, and the covariance between the two, $2Z^{\mathrm{St}}_{k,j}Z^{\mathrm{Tr}}_{k,j}$, in green (the same normalization as in Fig. 2.2a is used in all cases). There is substantial westward travelling wave variance between periods of 15 to 30 days, while standing waves dominate at the lowest frequencies. We also have the expected properties that $Z^{\mathrm{St}}_{k,j} = Z^{\mathrm{St}}_{k,-j}$, and that either $Z^{\mathrm{Tr}}_{k,j} = 0$ or $Z^{\mathrm{Tr}}_{k,-j} = 0$. Next we smooth each of the terms individually, as discussed in Section 2.2.4. The smoothed spectra, as well as the gaussian window used to do the smoothing, are plotted in Fig. 2.2c.

We also compare with the methods described by von Storch and Zwiers (1999), which are based on those in Pratt (1976) and Hayashi (1977). However, as noted in Section 2.2.3, the Pratt method described in von Storch and Zwiers (1999) is actually a conflation of the true Pratt and Hayashi methods. For the remainder of this chapter, when we discuss the "Pratt" method, we refer to the method attributed to Pratt that is described in Section 11.5.7 of von Storch and Zwiers (1999).

In Fig. 2.2d the decompositions described by Pratt and Hayashi are shown. The variance is exclusively decomposed into standing and travelling portions, without any covariance. Furthermore, note that these authors suggest computing a smoothed wavenumber-frequency spectrum before making the decomposition into standing and travelling components. This is what has been done in Fig. 2.2d, and so for comparison, in Fig. 2.2e we show the results for our decomposition based on the pre-smoothed total spectrum (see discussion in Section 2.2.4). Our method gives identical results for the standing wave power as the Pratt method when consistent smoothing is done, and the Hayashi standing wave power is generally similar. However, both Pratt and Hayashi attribute the remaining variance exclusively to the travelling wave, whereas we assign it to both

the travelling wave and the covariance between the standing and travelling waves. This leads to a major reduction in the variance attributed exclusively to the travelling wave in our method. Also, note that Hayashi's method gives a negative travelling wave power at some frequencies, a clearly non-physical result.

2.3.2 Reconstruction of standing and travelling wave fields

Using Eqs. 2.2 and 2.3 with the decomposed amplitudes $Q^{\mathrm{St}}_{k,j}$ and $Q^{\mathrm{Tr}}_{k,j}$ replacing the total amplitudes $Q_{k,j}$, one can reconstruct the standing and travelling parts of the signal $q(\lambda, t)$. To accurately reconstruct the original signal, it is necessary to use the unsmoothed amplitudes. In the two right columns of Fig. 2.3, the wave-1 portions of the standing and travelling signals are plotted for 60°N and 100hPa, for the 1979-1980 and 1990-1991 winters. As we had expected from viewing the total wave-1 anomaly (left column of Fig. 2.3), the 1979-1980 year contains a consistent westward propagating wave. However the quantitative decomposition we make allows us to also recognize the significant contribution of standing waves to the variability this year. For the 1990-1991 year, we see the expected result: the standing wave field looks very similar to the total field, while the travelling wave field generally has small amplitudes. Note that the standing and travelling wave reconstructions are not "pure" standing or travelling waves because they are the combination of a range of frequencies. As well, since the method naturally focuses on explaining the largest-variance features, in some cases it is possible for the technique to generate somewhat spurious results in the low-amplitude part of the signal. For example, in Fig. 2.3, the standing part of the signal for mid-November to December of 1990 contains an eastward propagating feature. Nevertheless, it is of much smaller amplitude than the standing wave feature later in the season, which is accurately captured.

2.3.3 Climatological spectra at 60°N

The frequency spectra at 60°N for three different vertical levels and for planetary waves 1 to 3 are shown in Fig. 2.4. Note that in Fig. 2.4 we do not have the property that either $Q^{\mathrm{Tr}}_{k,j} = 0$ or $Q^{\mathrm{Tr}}_{k,-j} = 0$. This is because we have averaged over multiple spectra, each corresponding to one winter season. For some wavenumbers and levels, it is common to have either westward or eastward travelling waves depending on the winter, and so for the climatological spectra one can have travelling waves contributions in both directions at the same absolute frequency.

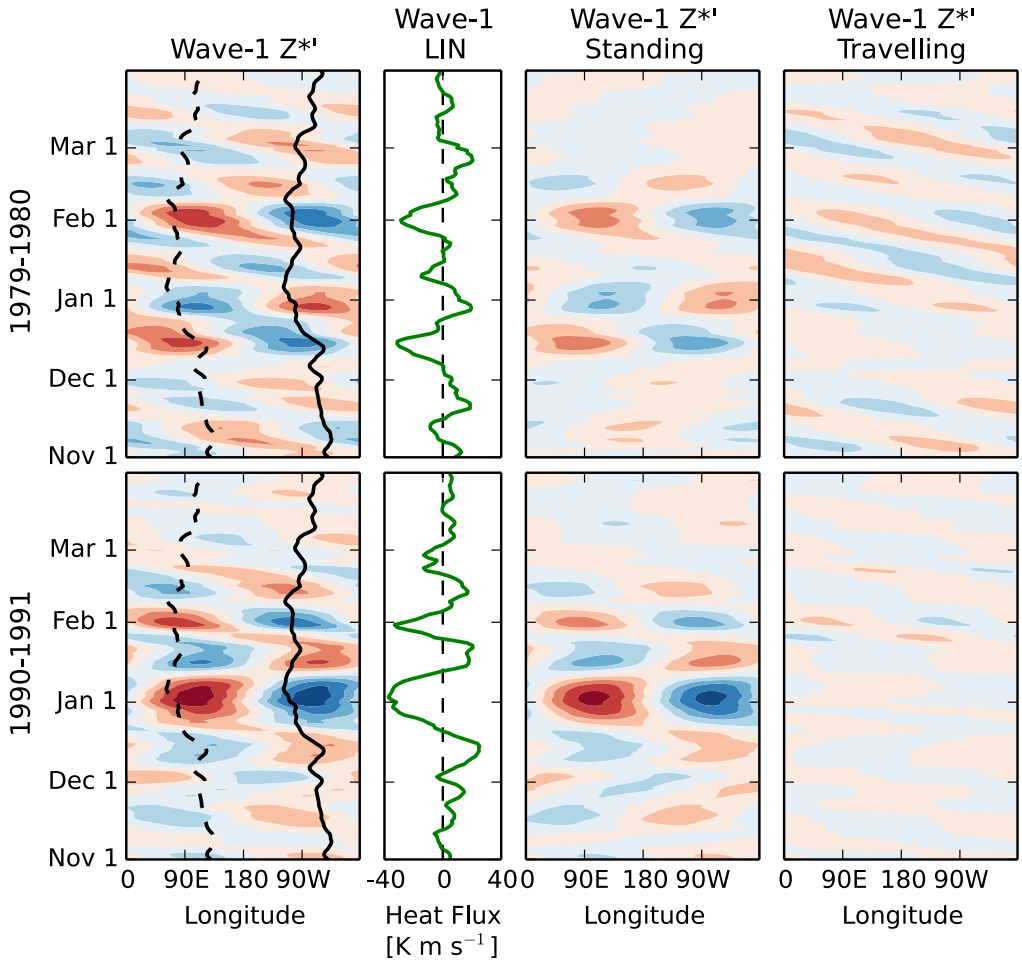

Figure 2.3: Wave-1 $Z^{*\prime}$ and LIN heat flux at 60°N and 100hPa for two NDJFM seasons: top, 1979-1980 and bottom, 1990-1991. From left to right: wave-1 $Z^{*\prime}$, wave-1 component of LIN heat flux, wave-1 ${Z^*_{\mathrm{St}}}'$ and wave-1 ${Z^*_{\mathrm{Tr}}}'$. The contour levels for all the Hovmöllers are $\pm(0, 100, 200, 300, 400, 500)$m where the reds are positive and blues are negative. The solid and dashed black lines on the furthest left panels show the daily position of the maximum and minimum of the wave-1 of Z^*_c. For each row the two right panels sum to the leftmost panel.

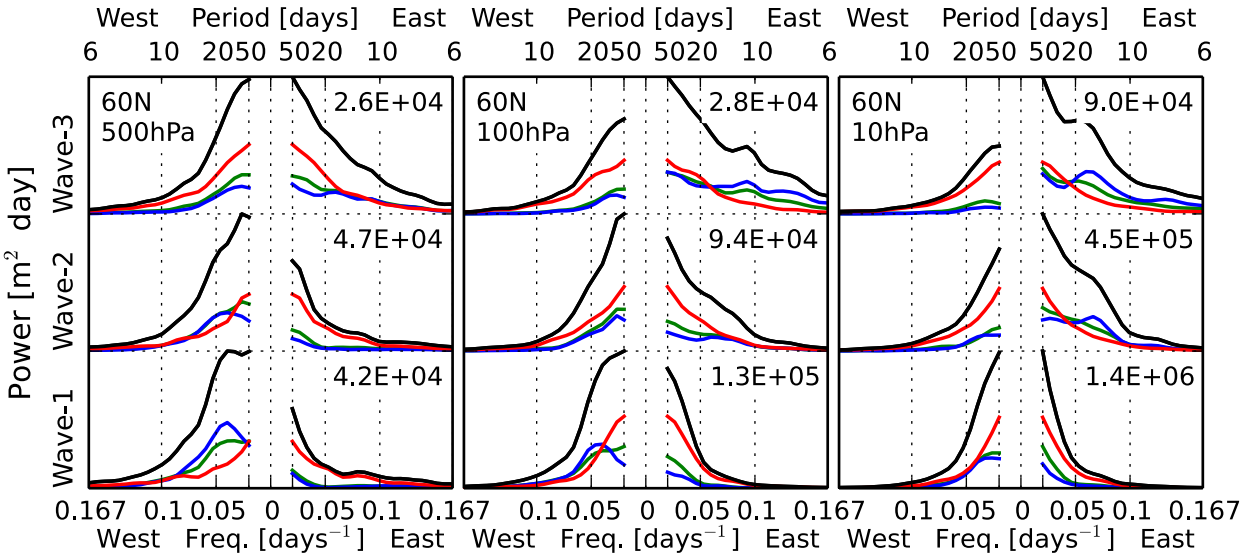

Figure 2.4: The climatological wavenumber-frequency spectrum of anomalous geopotential height, $Z^{*\prime}$, for NDJFM at 60°N and left) 500hPa, middle) 100hPa and right) 10hPa. Black is total spectrum $(Z_{k,j})^2$; red is standing spectrum $(Z^{\mathrm{St}}_{k,j})^2$; blue is travelling spectrum $(Z^{\mathrm{Tr}}_{k,j})^2$; and green is standing-travelling covariance $2Z^{\mathrm{St}}_{k,j}Z^{\mathrm{Tr}}_{k,j}$. Only the first three wavenumbers, and periods to 6 days are shown. The same smoothing as in Fig. 2.2c is used. All wavenumbers and levels are plotted using different scales, which are shown in the top-right corner of each plot, indicating in units of $\mathrm{m}^2 \cdot$day the maximum value reached by the total spectrum for that wavenumber and level. The spectra are normalized by $\frac{2}{N^2 T}$ so that integrating over frequency and summing over wavenumber will recover the total variance of the original signal.

Figure 2.4 shows that standing waves explain the largest portion of the variance of $Z^{*\prime}$ at most wavenumbers and especially for low frequencies at the given latitude and pressure levels. An exception is for wave-1 and wave-2 at 500hPa, and to a lesser extent 100hPa, where there is a substantial westward travelling peak in the spectrum at a period of approximately 25 days. This feature has been identified before by Speth and Madden (1983) and others. As well, in the mid-stratosphere there are eastward travelling wave-2 and wave-3 components, although wave-3 explains a very small portion of the variance here. Finally, Fig. 2.4 also shows that the covariance term explains a significant portion of the total variance, typically being roughly similar to the variance explained by the travelling component.

2.3.4 Frequency-integrated Northern Hemisphere spectra

To better appreciate the contributions of standing and travelling waves throughout the atmosphere, we integrate the individual spectra (the total, standing, travelling and covariance parts) over frequency to find the climatological variance explained by each of these portions for each wavenumber, at all latitudes and levels. The total and standing spectra are integrated over all frequencies, whereas the travelling and covariance parts are integrated separately over negative and positive frequencies to isolate the eastward and westward components. These quantities are shown for the Northern Hemisphere in Fig. 2.5. We separately show the contributions from waves 1 through 4, and sum together the contributions from waves 5 through 10. Note the logarithmic scale for the contours: each contour represents a doubling of variance. Furthermore, in each row, the five right panels summed together give the left-most panel.

The most important points to take from Fig. 2.5 are the following. As expected by the Charney-Drazin criteria (Charney and Drazin, 1961), the stratospheric anomalies are dominated by wave-1 and wave-2, and to a lesser extent wave-3. In the stratosphere, the standing waves typically explain about half the total variance and the remaining variance is distributed roughly equally between the four remaining categories for wave-1, while for waves-2 and -3 there is more power in the eastward travelling and covariance parts than in the westward parts. In the troposphere, there is a largely different distribution of variance. In terms of wavenumber, the maximum contribution depends on the latitude: at very high latitudes (north of 75°) wave-1 makes the largest contribution, while moving to lower latitudes, larger wavenumbers tend to make relatively larger

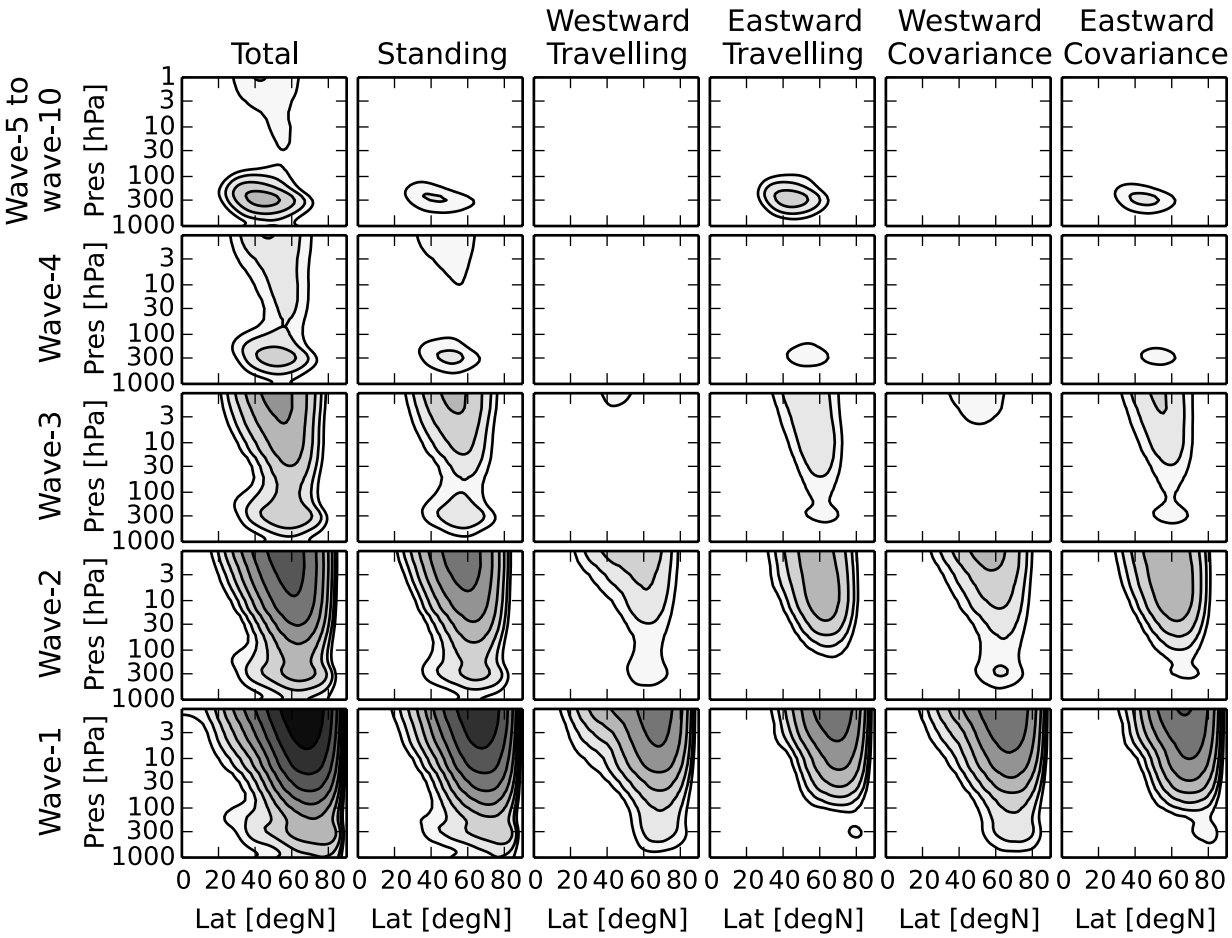

Figure 2.5: The total variance integrated over frequency of various components of wavenumber-frequency spectra of anomalous geopotential height, $Z^{*\prime}$, for NDJFM in the Northern Hemisphere. The six columns are, from left to right: 1) the total power spectrum (positive and negative frequencies), 2) the standing variance (positive and negative frequencies), 3) the travelling variance (westward) and 4) the travelling variance (eastward), 5) the standing-travelling covariance (westward) and 6) the standing-travelling covariance (eastward). The five rows correspond to, from bottom to top: 1) wave-1, 2) wave-2, 3) wave-3, 4) wave-4 and 5) sum from wave-5 to wave-10. The contours levels are the same in all subplots: (8, 16, 32, 64, 128, 256, 512, 1024, 2048, 4096)$\times 10^2 \mathrm{m}^2$.

contributions. Furthermore, at very high-latitudes standing waves explain a majority of the variance of wave-1, while between 60°N and 80°N there is a substantial westward travelling and covariance contribution. This was noted previously in Fig. 2.4. Moving to higher wavenumbers, there is generally a diminishing contribution from standing waves, and an increase in the variance explained by eastward propagating waves instead of westward propagating waves, as we expect from the simple β-plane Rossby wave dispersion relation. For synoptic scale disturbances (waves 5-10), the majority of the variance is explained by eastward travelling waves in the mid-latitudes, as expected.

The westward and eastward covariance portions, in the two right columns of Fig. 2.5, are generally similar in structure and amplitude to the respective westward and eastward travelling variances. We do not necessarily expect to find any independent information in the covariance plot: by the construction of the standing-travelling decomposition, the covariance between the two wave structures at some wavenumber and frequency is entirely determined by the amplitudes (or variances) of the individual standing and travelling parts (see Eq. 2.6).

2.3.5 Relative structure of standing and climatological wave

Having established the importance of standing waves throughout the extratropical atmosphere, we now seek to understand their zonal structure. In particular, we wish to know whether the nodes and antinodes of these standing waves have preferred longitudinal positions. If so, and if the antinodes are in alignment with the maximum and minimum of the climatological wave, then the standing waves will primarily be driving amplification and attenuation of the climatological wave (instead of, for example, a zonal shift of the climatological wave). This would imply that the standing waves would be efficient drivers of the linear part of the vertical flux of Rossby wave activity (i.e. the LIN term introduced in Section 1.4).

Figure 2.6 shows the climatological time-variance of $Z^{*}_{\mathrm{St}}{}'$ (see Eq. 2.9) over NDJFM for wave-1 and wave-2 at 500hPa, 100hPa and 10hPa, as well as the climatological wave-1 and wave-2 Z^{*}_{c} at these levels. The presence of zonal maxima of variance, especially in wave-1, indicates that the standing waves do have preferred spatial positions. This can be confirmed by plotting a histogram of the phase $\overline{\phi}_{k,j}$ (Eq. 2.8) computed for all winter seasons and frequencies (not shown, but see Fig. 4.6 in Chapter 4 which shows a histogram of wave-1 phase at 60°N and 100hPa over all wintertime days).

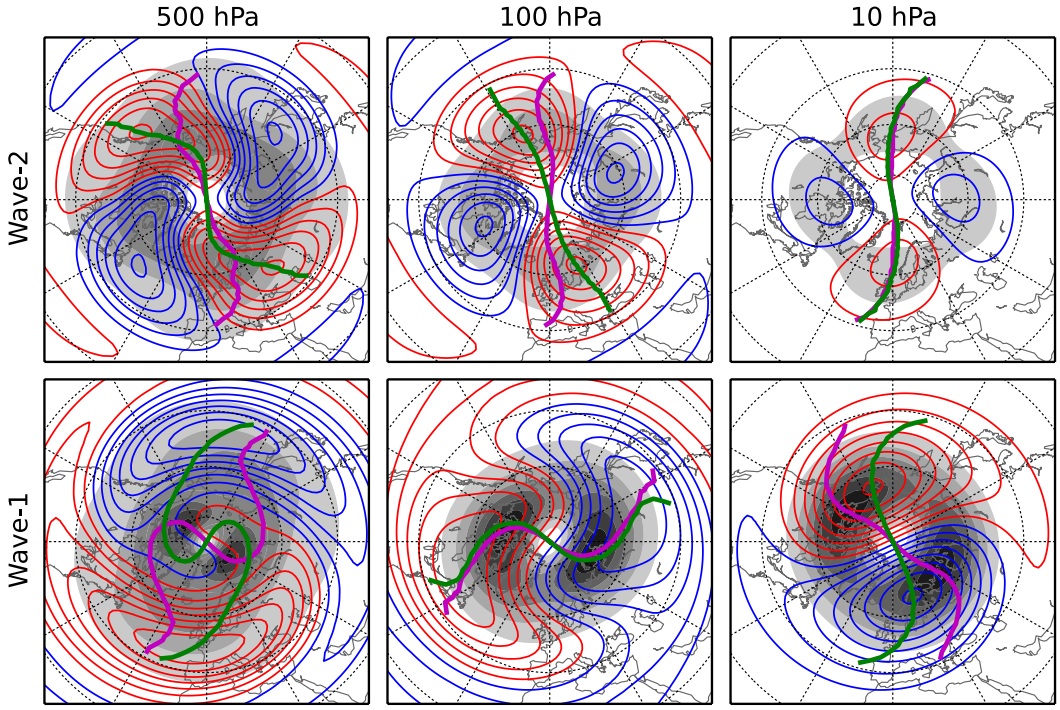

Figure 2.6: Shading: variance over time of $Z^*_{\mathrm{St}}{}'$, as in Eq. 2.10, computed individually for each winter season, then averaged over all years. Contours: climatological wave Z^*_c averaged over NDJFM. Bottom row is wave-1, top row is wave-2, columns from left to right are 500hPa, 100hPa and 10hPa. The shaded contours are, from left to right: $(0, 6, ..., 48)\times10^2\mathrm{m}^2$, $(0, 2, ..., 14)\times10^3\mathrm{m}^2$, and $(0, 15, ..., 105)\times10^3\mathrm{m}^2$. The coloured line contours are, from left to right, $\pm(7, 21, 35, ..., 119)$m, $\pm(12, 36, 60, ..., 156)$m, and $\pm(40, 120, 200, ..., 640)$m. Blues are negative, reds are positive. The contours are the same for wave-1 and wave-2. The thick purple and green lines show the positions of the zonal extremes of, respectively, the variance over time of $Z^*_{\mathrm{St}}{}'$ and the climatological wave Z^*_c. These lines are only plotted north of 40°N.

Focusing on wave-1, Fig. 2.6 shows that the relationship between the structure of the standing waves and the climatological wave changes substantially at different vertical levels. To clarify this point, we have plotted the longitude of the zonal maxima of the standing wave variance in the purple line, and the longitude of the zonal extrema of the climatological wave in the green line. We can see that at 500hPa, the maximum of the standing wave variance is at a much more northerly latitude than the maximum of the climatological wave and is zonally positioned near the zero lines of the climatological wave. On the other hand, at 100hPa and to a lesser extent 10hPa, the maximum of the standing wave variance is closely aligned with the climatological wave. This suggests that the wave-1 standing waves will be important drivers of linear interference effects at these levels. Note that although the wave-2 standing waves are weaker, they also have preferred zonal positions and are typically well aligned with the climatological wave-2, implying they are also expected to efficiently contribute to linear interference effects.

2.3.6 Vertical wave structure and propagation

The spectra shown thus far are computed independently at each pressure and latitude and so do not convey a sense of the vertical or meridional structure of the waves. Thus, although Fig. 2.6 shows a general westward tilt with height of the crests and troughs of the standing wave-1, we have no guarantee that individual standing waves indeed span these vertical levels and have such a tilt. In this section we further explore these structures and their time dependence by employing the time-lagged wave amplitude and phase correlation statistics of Randel (1987); see also Shaw et al. (2010). This method computes the spatially remote time-lagged coherence and relative phase of a certain wavenumber.

The required information for the analysis is the time-dependent spatial Fourier amplitudes and phases of geopotential height, which we compute from our already-calculated 2D Fourier coefficients, $\hat{z}_{k,j}$. See Section 2 of Randel (1987) for details of the computation of the correlation coherence and phase. We separately calculate the correlations based on the total wave anomaly ($\hat{z}_{k,j}$), the standing part ($\hat{z}^{\mathrm{St}}_{k,j}$), the westward travelling part ($\hat{z}^{\mathrm{Tr}}_{k,j}, j > 0$) and the eastward travelling part ($\hat{z}^{\mathrm{Tr}}_{k,j}, j < 0$). However, we will omit the eastward travelling wave coherence plot below because the eastward travelling signal is very weak in the troposphere (see Fig. 2.4) and we are computing the correlations referenced to 500hPa. We make the calculations for both wave-1 and wave-2. Equations 2.19

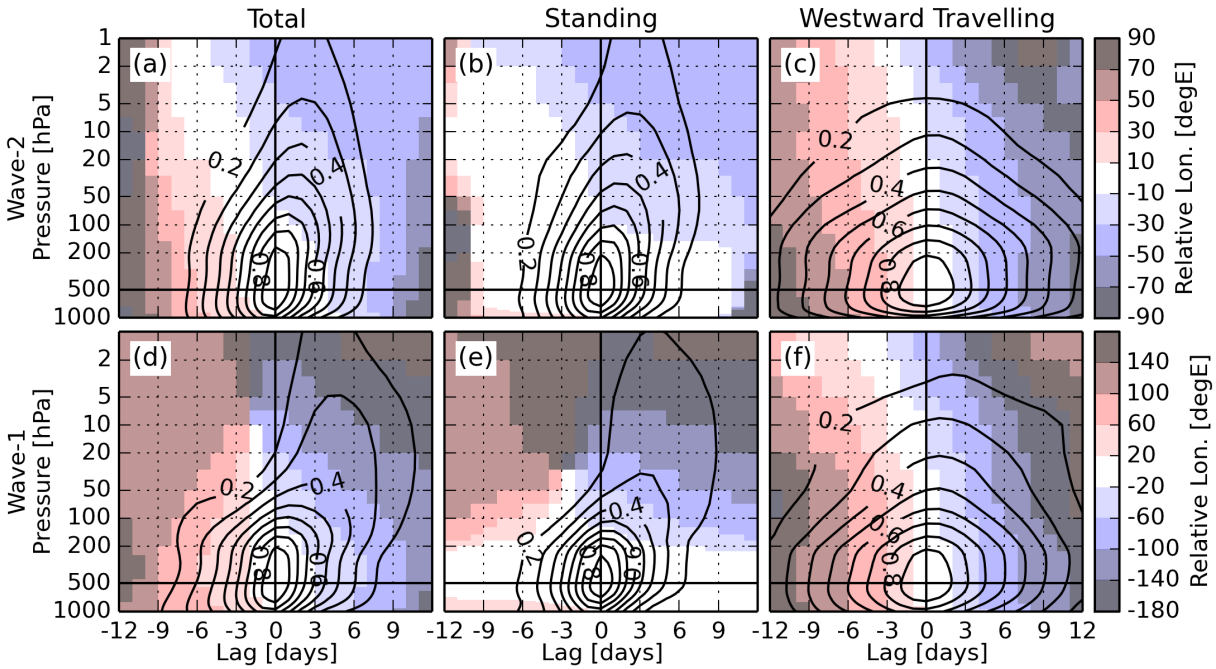

Figure 2.7: The correlation coherence (contours) and phase (shading) of wave-1 (bottom row) and wave-2 (top row) geopotential height anomalies during NDJFM at 60°N as a function of pressure and lag with respect to 60°N and 500hPa. The columns from left to right, correspond to correlations computed using the total wave anomaly, only the standing part, and only the westward travelling part (see Eqs. 2.19 and 2.20). The coherence is plotted at intervals of 0.1, starting from 0.2. The phase is plotted in degrees denoting the longitudinal separation of the two wave crests: positive phase means the distant (away from 0-day lag and 500hPa) wave is eastward of the reference wave.

and 2.20, below, give the precise definitions of the standing and westward travelling parts of the wave anomaly for some particular wavenumber k'.

Figure 2.7 shows a pressure versus lag cross-section at 60°N of the wave-1 and wave-2 correlation coherence and phase with respect to 60°N and 500hPa for the total wave anomaly (left column), the standing wave (middle column) and westward travelling wave (right column). Shaw et al. (2010), using a shorter dataset and hence fewer degrees of freedom, estimate that coherences above 0.18 are statistically significant at the 99% level. We only plot coherences of 0.2 or above, and are thus assured that the coherences shown are all significant at least at the 99% level. Focusing first on the total wave-1 anomalies (Fig. 2.7d), we see evidence for the well-known upward propagation of wave-1: for positive 3- to 6-day lags, there is a strong (>0.3) coherence between wave amplitudes at 10hPa and the reference point at 500hPa. Furthermore, at 0-day and positive lags the wave-1 has a westward tilt with height throughout the upper troposphere and stratosphere, further evidence for the upward propagation of the wave. There is a suggestion of downward propagation for negative lags in the phase diagram (eastward phase tilt

with height) but no such indication in the coherence diagram. This is partially due to using the entire NDJFM period to compute the correlations: as shown in Shaw et al. (2010), wave reflection has a strong seasonal cycle, and peaks in strength in JFM. Furthermore, stronger couplings to the stratosphere, both upward and downward, are seen if a meridional average (e.g. from 45°N to 80°N as in Shaw et al., 2010) is performed before computing the correlations. We choose to perform the correlations based on the 60°N latitude for easy comparison with results we have already shown based solely on this latitude, e.g. in Figs. 2.3 and 2.4. Last, we note the clear tendency of westward propagation of wave-1 throughout the troposphere, as seen in the steadily decreasing phase with lag in Fig. 2.7d. Generally the same conclusions can be reached for the total wave-2 signal (Fig. 2.7a) except that the timescale for upward propagation is faster (2 to 3 days) and there is no eastward phase tilt with height at negative lags.

Now we examine the correlations separately for the standing and westward travelling parts of the wave-1 and wave-2 geopotential height anomalies, which are specifically given by (for some wavenumber k'):

$$z^{\mathrm{St}}_{k'}(\lambda,t) = \frac{2}{NT}\sum_{j=-T_2}^{T_2} Z^{\mathrm{St}}_{k',j}\cos\left(k'\lambda+\omega_j t+\phi_{k',j}\right) \tag{2.19}$$

$$z^{\mathrm{TrW}}_{k'}(\lambda,t) = \frac{2}{NT}\sum_{j=1}^{T_2} Z^{\mathrm{Tr}}_{k',j}\cos\left(k'\lambda+\omega_j t+\phi_{k',j}\right). \tag{2.20}$$

Here, $Z^{\mathrm{St}}_{k',j}$ and $Z^{\mathrm{Tr}}_{k',j}$ are respectively the wave-k' standing and travelling amplitudes of the geopotential height anomaly at frequency ω_j and $\phi_{k',j}$ is the wave-k' phase at frequency ω_j. Note that in Eq. 2.20 we sum over only positive j in order to isolate the westward travelling waves.

Examining Fig. 2.7e, we see that for wave-1 the standing wave coherence is similar to the total wave coherence, but with generally smaller coherences throughout. The correlation phase for the standing wave is analogous to that for the total wave, but without the westward propagation in the troposphere. In addition, the westward and eastward phase tilts with height for positive and negative lags tend to be more extreme for the standing wave as compared to the total wave. As expected from the definition of the standing wave, at 500hPa we see essentially no change in the phase of the wave with time for the lags shown, although at approximately ± 14 days (not shown) there is a sharp 180° jump in phase, which would be in accordance with a standing wave with a 28-day period. For wave-2 (Fig. 2.7b) there is a very close correspondence between the

coherence plots of the standing and wave and the total wave, and there is no change in phase until lags of ± 10 days.

The westward propagating wave-1 and wave-2 anomalies (Figs. 2.7c and f) are vertically deep signals, spanning the troposphere and up to the mid-stratosphere at 0-day lag, with an equivalent barotropic structure in the troposphere and weak westward phase tilts with height in the stratosphere. Furthermore they have a much longer coherence timescale (0.2 coherence up to ±13 days at 500hPa for wave-1) compared to the total wave in both in the troposphere and in the stratosphere. The correlation phases show the expected consistent phase propagation, with a 360° revolution at 500hPa being made in about 28 days for wave-1, roughly in accordance with the westward travelling wave-1 spectral peak seen in the left panel of Fig. 2.4. These results agree with the vertical structure of Northern Hemisphere high-latitude westward propagating wave-1 features identified by previous authors, e.g. Fig. 11 of Branstator (1987) or Fig. 7 of Madden and Speth (1989). The eastward travelling signals (not shown) are strongly trapped in the troposphere and the progression of phase is not as consistent as for the westward travelling wave.

Note that largely the same conclusions can be reached by picking a reference point in the stratosphere, for example at 60°N and 10hPa (not shown). The standing wave amplitudes here are preceded by anomalies in the troposphere about 3 to 6 days before for wave-1 (less for wave-2), and the westward propagating waves fill the depth of the stratosphere and troposphere with a barotropic structure in the troposphere and a slight westward tilt with height in the stratosphere. The eastward waves referenced to the stratosphere do not penetrate into the troposphere.

2.3.7 Standing and travelling waves in the tropics

The results in Sections 2.3.1 to 2.3.6 were included in Watt-Meyer and Kushner (2015a). In this section, additional unpublished results documenting the spectral characteristics of waves in the tropics analyzed with the standing-travelling wave decomposition are shown. While the primary focus of this thesis is on extratropical dynamics, atmospheric motions in the tropics exhibit a wide variety of coherent wave-like behaviours and thus are an interesting testbed for the standing-travelling wave decomposition developed in this chapter. The pioneering work of Matsuno (1966) computed the dispersion relations associated with the equatorial beta-plane linearized shallow water equations. This anal-

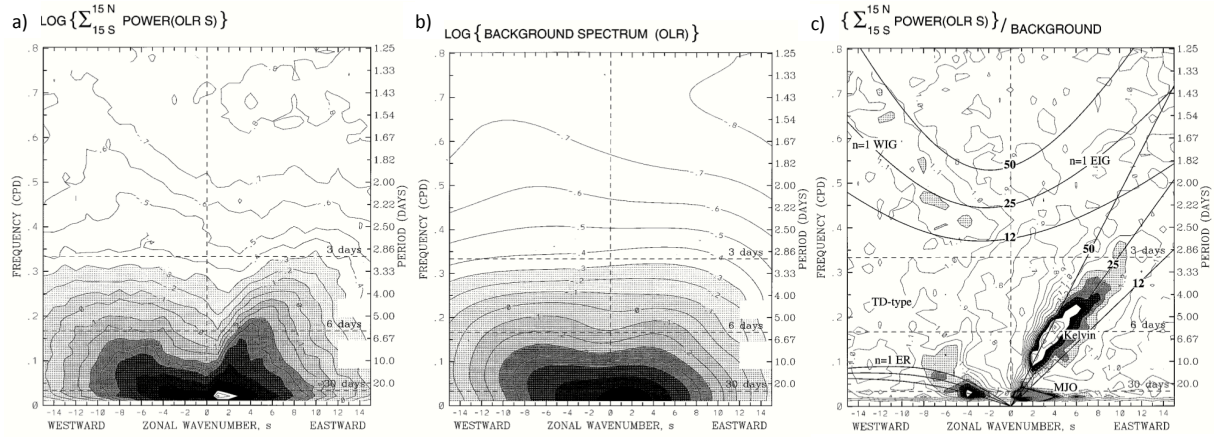

Figure 2.8: a) The zonal wavenumber-frequency power spectrum of the symmetric component of OLR. The power has been summed over 15°S-15°N latitude, and the base-10 logarithm taken for plotting. b) Zonal wavenumber-frequency spectrum of the base-10 logarithm of the "background" power calculated by averaging the individual power spectra of the antisymmetric and symmetric OLR and smoothing many times with a 1-2-1 filter in both wavenumber and frequency. c) The symmetric OLR power of a) divided by the background power of b). Superimposed are the dispersion curves of the odd meridional mode-numbered equatorial waves for the three equivalent depths of h=12, 25 and 50 m. Panels a), b) and c) are reproduced from, respectively, Figs. 1, 2 and 3 of Wheeler and Kiladis (1999).

ysis identified Rossby, Kelvin and inertio-gravity waves as eigenmodes of the equations, and calculated the circulation patterns expected for each of them. Early observational studies confirmed the existence of some of these wave types, in particular in the tropical lower stratosphere (e.g. Yanai and Maruyama, 1966; Wallace and Kousky, 1968). The studies of Takayabu (1994) and Wheeler and Kiladis (1999) clearly demonstrated the existence of these waves by computing wavenumber-frequency spectra of relatively long records of brightness temperature and outgoing longwave radiation near the equator. A key advance of Wheeler and Kiladis (1999) that facilitated the clear identification of the dispersion relations predicted by Matsuno (1966) was the removal of a red "background" spectrum which was meant to represent non-periodic processes in the tropics (this will be discussed further below). However, the construction of this background spectrum was done rather heuristically (see also Hendon and Wheeler, 2008) and so in this section we explore the possibility of isolating wave modes using the standing-travelling decomposition instead of using the removal a background spectrum.

The data analyzed is twice-daily outgoing longwave radiation (OLR) on a 2.5° grid over the period of 1979-2013 (Liebmann and Smith, 1996). OLR is often used as a proxy for deep precipitating convection in the tropics (e.g. Arkin and Ardanuy, 1989) and thus can be used to track convectively-coupled waves. The data is analyzed as follows, generally following the procedure of Wheeler and Kiladis (1999). A daily climatology, com-

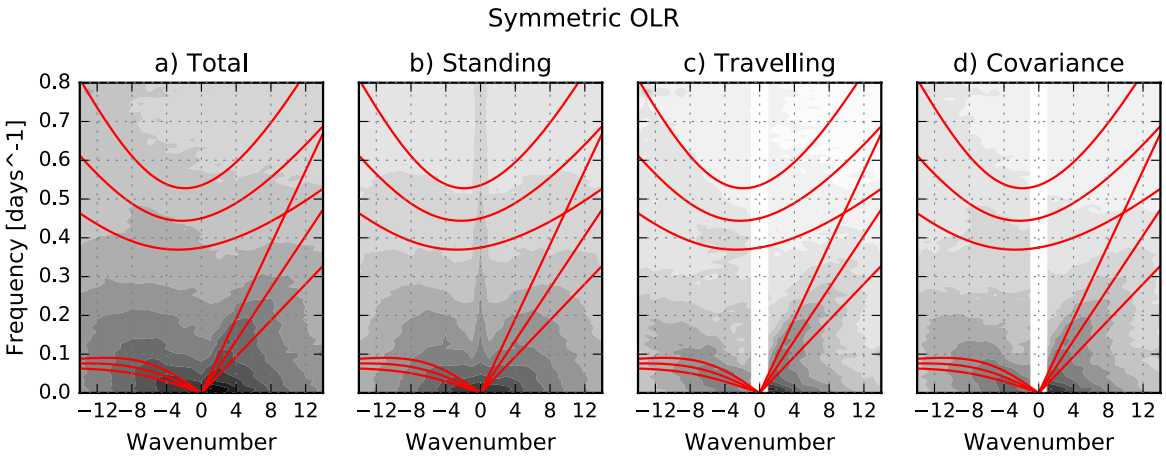

Figure 2.9: The logarithm of (a) the total, (b) the standing component, (c) the travelling component and (d) the covariance component of the wavenumber-frequency spectrum of OLRS, summed between 15°S and 15°N. Contour intervals are the same in all panels. The red curves indicate the dispersion relations for $n = 1$ eastward and westward inertio-gravity waves, $n = 1$ equatorial Rossby waves and Kelvin waves, using equivalent depths of $H = 12, 25, 50$m, as in Fig. 3b of Wheeler and Kiladis (1999).

puted by a simple average over all years, is first removed from the data. Because linear waves of the equatorial shallow water equations are either symmetric or antisymmetric about the equator, the OLR data is separated into its symmetric and antisymmetric parts. That is, $\mathrm{OLR}(\phi) = \mathrm{OLRS}(\phi) + \mathrm{OLRA}(\phi)$, where $\mathrm{OLRS}(\phi) = [\mathrm{OLR}(\phi) + \mathrm{OLR}(-\phi)]/2$ and $\mathrm{OLRA}(\phi) = [\mathrm{OLR}(\phi) - \mathrm{OLR}(-\phi)]/2$. Then, the wavenumber-frequency analysis of Section 2.2.1 is applied to sequential 96-day segments of OLRS and OLRA and then the total power spectrum, and the standing, travelling and covariance components, are averaged over all segments. Finally, the spectra are summed from 15°S to 15°N. Before showing the results of our computation of the spectra, some results from Wheeler and Kiladis (1999) are reproduced in Fig. 2.8. Figure 2.8a shows the total spectra of the symmetric component of OLR. Wheeler and Kiladis then construct a "background" spectrum by averaging the OLRS and OLRA power spectra, and then heavily smoothing the result (see Fig. 2.8b). The OLRS spectrum with the background removed is shown in Fig. 2.8, and it clearly shows peaks in the spectrum associated with linear equatorial waves. Below, the possibility of using the standing-travelling decomposition to identify these peaks will be explored.

Figures 2.9 and 2.10 show the wavenumber-frequency spectra and its components for, respectively, the symmetric and antisymmetric components of the OLR. Figures 2.9a and 2.10a are analogous to Fig. 1a and 1b of Wheeler and Kiladis (1999), although here are calculated using data from a longer record. The dominant characteristic of

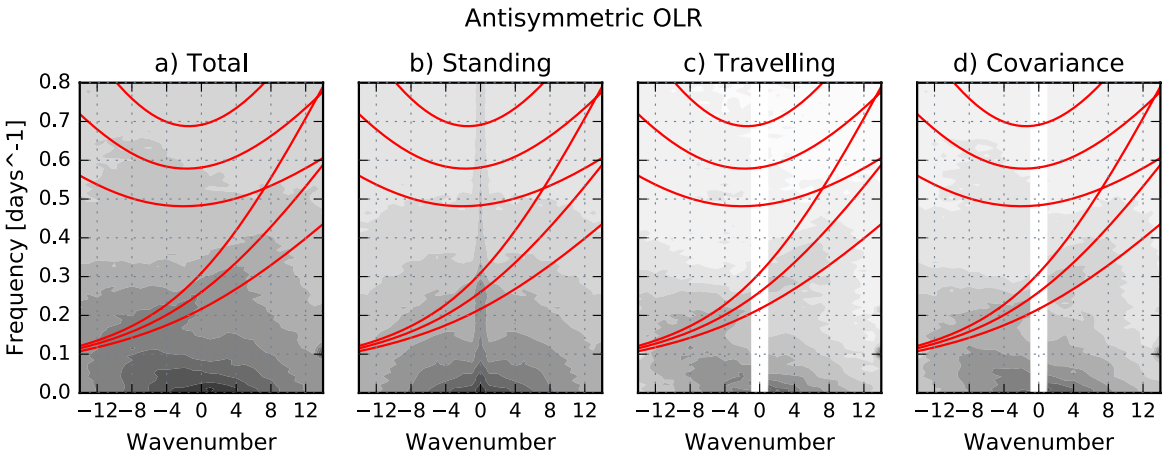

Figure 2.10: As in Figure 2.9 but for OLRA. Contour intervals are the same. The red curves indicate the dispersion relations for $n = 0$ eastward inertio-gravity waves, mixed Rossby-gravity waves, and $n = 2$ eastward and westward inertio-gravity waves, using equivalent depths of $H = 12, 25, 50$m, as in Fig. 3a of Wheeler and Kiladis (1999).

both spectra is their generally red nature, with higher power at lower wavenumbers and frequencies. However, on top of this red background, there is clear evidence of ridges in the power spectra that indicate preferred length and timescales, and these regions tend to be roughly aligned with the theoretical dispersion relations computed from the linearized beta-plane equatorial shallow water equations (which are indicated by the red lines in Figs. 2.9 and 2.10). These ridges are the features that Wheeler and Kiladis (1999) isolated by dividing each spectrum by a smoothed background, and identified with the dispersion relations of linear equatorial waves. Instead of following such a procedure, here the standing-travelling wave decomposition is applied to the OLR spectra, and in the remaining panels of Figs. 2.9 and 2.10, the logarithm of standing, travelling and covariance components of the wavenumber-frequency spectra are shown. Unlike the other analyses of this thesis, here the zonal mean is not removed prior to analysis. However, the standing-travelling wave analysis will exclusively place any zonal mean variability into the standing component, because the time-spectrum of the zonal mean is symmetric with respect to frequency as a consequence of the zonal mean being real (as opposed to the wave components which have an amplitude and phase). This is the reason for the sharp jump in the standing wave spectrum at wavenumber-0 seen in Figs. 2.9b and 2.10b. The decomposition of OLR into standing and travelling components indicates the following. For the symmetric OLR, the standing power is generally red, except for a range of frequencies (about $0.1\,\text{days}^{-1}$ to $0.3\,\text{days}^{-1}$) where the power is highest for wavenumbers 5-7. The antisymmetric OLR standing power is in general more smoothly red across

wavenumbers and frequencies. The travelling components of the spectra (Figs. 2.9c and 2.10c) show clear evidence of the ridges in the spectrum that are hinted at in the total spectra. Finally, as was found in Sections 2.3.3 and 2.3.4, the covariance part of the spectrum is in general similar in structure to the travelling part of the spectrum.

A particularly interesting part of the OLR spectra is the ridge associated with Mixed Rossby-Gravity and $n = 0$ Eastward Inertio-Gravity waves in the antisymmetric spectrum (i.e. the ridge from approximately $k = -4$ and $\omega = 0.2$ days^{-1} to $k = 8$ and $\omega = 0.4$ days^{-1} in Fig. 2.10a). It is unique in that it is the only dispersion relation that crosses the wave-0 line, and thus is a mix of standing power (close to $k = 0$, where there is nearly equal power for negative and positive wavenumbers) and eastward and westward travelling power further from $k = 0$. In fact, the relationship between these wave types, and whether they primarily consist of standing or travelling variability is a topic of current research (Kiladis et al., 2016; Dias and Kiladis, 2016). Future work could provide a new perspective on this issue by using the standing-travelling decomposition developed here.

In summary, this section demonstrates that the standing-travelling wave decomposition is applicable to convectively-coupled waves in the tropics, and that the travelling wave part of the spectrum emphasizes the parts of the spectrum corresponding to theoretically predicted dispersion relations.

2.4 Summary

In this chapter a novel decomposition of longitude- and time-dependent signals into standing and travelling components was introduced. Unlike previous techniques, this method explicitly provides the covariance between the standing and travelling waves, and permits reconstruction of the standing and travelling signals. The decomposition was applied to geopotential height anomalies in the Northern Hemisphere winter. Focusing on planetary waves 1 to 3, we found that at 60°N the standing wave explains the largest portion of the variance in wave anomalies, especially at low frequencies. There are exceptions for wave-1 and to a lesser extent wave-2, which have substantial westward travelling anomalies in the troposphere with periods around 25 days. In the stratosphere standing waves generally dominate, except for a small peak in eastward travelling wave-2 with a period of about 16 days.

We have also shown that planetary wave-1 and wave-2 standing wave anomalies have preferred longitudinal positions and that their antinodes generally align with the maximum and minimum of the climatological wave, especially in the lower- and mid-stratosphere. This implies that the standing waves should be an efficient driver of LIN, which is the anomalous vertical flux of Rossby wave activity linearly dependent on the climatological wave pattern. This point will be examined in more detail in Chapter 3. Next, we examined the vertical and time-lagged structure of the standing and travelling wave-1 and wave-2 signals with respect to 60°N and 500hPa. We found that the standing waves have a similar structure to the total wave with a tendency for upward propagation from the troposphere to the stratosphere with a timescale of 3 to 6 days (2 to 3 days) for wave-1 (wave-2). On the other hand, the westward travelling wave-1 and wave-2 are deep signals spanning the troposphere and stratosphere with relatively little phase tilt.

The separation of wave anomalies into standing and travelling parts is helpful for distinguishing the wave events which originate in the troposphere and drive stratospheric variability. Although, as we have shown, the westward propagating wave-1 is a strong feature in the high-latitude troposphere and lower stratosphere, because of its lack of phase tilt we do not expect it to strongly contribute to the vertical flux of wave activity. On the other hand, we have isolated standing waves and shown that they have a tendency to strengthen and weaken the climatological wave. In addition the phase tilts and time-lagged coherences of the standing wave contributions are suggestive of upward propagation, and one would expect them to be responsible for the upward communication of wave activity anomalies from the troposphere to stratosphere. Chapter 3 will quantify the contributions of the standing and travelling waves to wave activity flux variability over a range of timescales.

Moving beyond planetary waves in the Northern Hemisphere extratropics, Section 2.3.7 computed the spectral characteristics of convectively coupled waves in the tropics. It was shown that the standing-travelling wave decomposition is capable of isolating the spectral signatures corresponding to the dispersion relations of various theoretically predicted linear equatorial waves.

Chapter 3

Standing wave contributions to persistent upward wave activity flux anomalies

3.1 Introduction

The predictability of extreme stratospheric polar vortex events in the Northern Hemisphere winter is a topic of current research (e.g. Tripathi et al., 2015) due to their significant impact on tropospheric weather on the timescales of weeks to months (Baldwin and Dunkerton, 2001; Thompson et al., 2002; Sigmond et al., 2013). Weakening and strengthening of the polar vortex is known to be preceded by, respectively, persistent positive and negative anomalies of upward wave activity flux in the lower stratosphere (Newman et al., 2001; Polvani and Waugh, 2004). A number of studies have emphasized the sensitivity of mean-flow variability in the stratosphere to the timescale of wave activity pulses (Harnik, 2009; Sjoberg and Birner, 2012, 2014). In particular, Harnik (2009) showed that shorter pulses of upward wave activity resulted in wave reflection in the upper stratosphere, and no long-lasting deceleration of the polar vortex, while longer pulses forced a sudden stratospheric warming (SSW) like response, with a downward propagation of zonal mean wind anomalies through the stratosphere. Sjoberg and Birner (2012, 2014) explored the importance of the duration of wave activity pulses in driving weakenings in the strength of the polar vortex. They showed both in reanalysis and through simple modeling experiments that the stratosphere is especially responsive to

positive anomalies of wave activity flux of duration 10 to 20 days. This suggests that understanding the mechanisms that tend to drive pulses of this longer timescale is essential for improving the prediction of SSWs.

As introduced in Section 1.4, the linear interference framework is a useful way to understand the drivers of upward wave activity flux pulses. Smith and Kushner (2012) documented the relative contributions of the LIN and NONLIN terms to the overall variability of upward wave activity flux in the lower stratosphere. It was found that the LIN term is more persistent than either the NONLIN or total heat flux, and given the work outlined in the paragraph above, this suggests it may be more important for driving changes in the strength of the stratospheric polar vortex. This will be addressed in more detail in this chapter. Furthermore, a question outstanding from Smith and Kushner (2012) was whether the LIN term is primarily driven by standing waves with fixed nodes and varying amplitude or by travelling waves moving in and out of phase with the climatology. This chapter uses the statistical technique that was described in Chapter 2 to decompose wave variability into standing and travelling components. This method is an improvement on classical techniques (Hayashi, 1971, 1977, 1979; Pratt, 1976) because it properly accounts for the covariance between the standing and travelling waves, and because it easily allows for the reconstruction of the real-space signals. Chapter 2 applied the decomposition to Northern Hemisphere planetary waves and showed that standing waves explain the largest portion of geopotential height variance at low frequencies and planetary wavenumbers. An exception is for wave-1 in the high-latitude troposphere, where a large portion of the geopotential height variance is in a low-frequency westward travelling wave. Furthermore, Chapter 2 showed that the standing waves have preferred longitudes for their crests and troughs, and that at most levels and latitudes these tend to align with the extremes of the climatological wave. This suggests that these standing waves should be efficient drivers of the LIN term.

Our current study makes a quantitative decomposition of the LIN term into contributions from standing and travelling waves. We show that on timescales greater than about 15 days, that is, on the timescales most important for the driving of polar vortex strength by upward wave activity flux, standing waves explain the majority of the variance of the LIN term. Furthermore, we show that because the standing waves are dominated by low frequencies they are more persistent than the other components of the heat flux. We explore the implications of this for the predictability of extreme stratospheric polar vortex events. We show that polar vortex strength anomalies are preceded

by persistent LIN heat fluxes in the troposphere and stratosphere that are primarily driven by standing waves. It is verified that climate models, particularly those with sufficient resolution of the stratosphere, are capable of capturing this connection between different components of the wave driving and polar vortex strength changes. Finally, we show that displacement sudden stratospheric warmings (SSWs) are primarily driven by standing waves forcing LIN heat flux, while split SSWs have shorter-lived heat flux precursors.

3.2 Data and methods

3.2.1 Data and notation

As in Chapter 2, we use 1979-2013 daily-mean geopotential height, meridional wind and temperature data from the ERA-Interim reanalysis (Dee et al., 2011). The data are on a $1.5^\circ \times 1.5^\circ$ latitude-longitude grid, with 37 vertical levels from 1000hPa to 1hPa. Daily climatologies are computed as an average over all 35 years of the dataset for each day of the year and are denoted as A_c for some arbitrary variable A. Anomalies from the climatology are written as $A' = A - A_c$. Zonal means are written as $\{A\}$ and deviations therefrom as $A^* = A - \{A\}$. Note that unlike in Chapter 2, we do not linearly detrend or remove the time-mean of each winter season before computing the spectral analysis. The reason for this is that the goal of this chapter is to separate the LIN heat flux into standing and travelling components, while the primarily goal of Chapter 2 was to estimate the wavenumber-frequency spectra of planetary waves.

We will focus on the heat flux anomalies averaged, with a cosine of latitude weighting, between 45°N and 75°N. We use this latitude range because this is where strong positive anomalies of upward wave activity flux occur before events of a weak stratospheric polar vortex (e.g. Fig. 3 of Limpasuvan et al., 2004) and because it has been used in many previous studies (e.g. Polvani and Waugh, 2004). Some of our results will examine the meridional eddy heat flux at 100hPa, as a proxy for upward wave activity flux from the troposphere to the stratosphere (Polvani and Waugh, 2004), while others show the heat flux anomalies at all levels. We will use the normalized polar cap geopotential height anomaly, north of 65°N, as a proxy for the Northern Annular Mode (NAM, Baldwin and Thompson, 2009), noting that this quantity has the opposite sign as the typically defined NAM. Sudden stratospheric warmings (SSWs) are identified using the

criteria of Charlton and Polvani (2007), including the categorization into displacement and split events. Central dates are identified by the day on which the zonal mean wind at 60°N and 10hPa falls below zero. The categorization into split and displacement events is done according to the first column in Table 1 in Hitchcock et al. (2013), which is based on the NASA Global Modeling and Assimilation Office MERRA reanalysis. The agreement between reanalysis products in the Northern Hemisphere for the satellite era (after 1979) is such that it is acceptable to use a classification applied to a different reanalysis product (for example, compare the two columns of Table 1 in Hitchcock et al. (2013)). We additionally include the split event of January 6, 2013 (e.g., Tripathi et al., 2015), which occurred after the study period of Hitchcock et al. (2013). Note that the results do not differ in a qualitative sense if the event categorization from Table 1 of Cohen and Jones (2011) is used, which is based on the NCEP-NCAR reanalysis.

Part of our interest in the results described in this study is due to their implications for potential improvements in climate prediction on seasonal and longer timescales. For this reason, we verify the ability of so-called high-top and low-top climate models with different vertical resolutions in the stratosphere to capture this variability (Gerber et al., 2010). In particular, we analyze simulations with the Canadian Middle Atmosphere Model (CMAM) (Scinocca et al., 2008). These experiments were examined by Shaw et al. (2009) in order to understand the importance of momentum conservation in gravity wave drag parameterizations. Briefly, they consist of 40-year high-top (model lid at 0.001 hPa with 71 vertical levels) and low-top (model lid at 10hPa with 41 vertical levels) simulations.[1] CMAM is an atmosphere-only model, and in these runs interactive chemistry is turned off. Results from a model lid height comparison experiment with the Centre National de Recherches Meteorologiques climate model, CNRM-CM5 (Voldoire et al., 2013), will also be shown.

3.2.2 Linear interference decomposition

As shown in Section 1.4, using the expansion of the meridional wind and temperature zonal eddies into their climatological and anomaly components, $v^* = v_c^* + v^{*\prime}$ and $T^* = T_c^* + T^{*\prime}$, the anomalous meridional heat flux can be written as (e.g. Smith and Kushner,

[1] These correspond to the HIGH_C and LOW_C experiments of Shaw et al. (2009).

2012),

$$\begin{aligned}\{v^*T^*\}' =& \{v^{*\prime}T^*_c\} + \{v^*_c T^{*\prime}\} + \{v^{*\prime}T^{*\prime}\}' \\ =& \text{LIN} + \text{NONLIN}\end{aligned} \tag{3.1}$$

where

$$\text{LIN} = \{v^{*\prime}T^*_c\} + \{v^*_c T^{*\prime}\} \tag{3.2}$$

$$\text{NONLIN} = \{v^{*\prime}T^{*\prime}\} - \{v^{*\prime}T^{*\prime}\}_c = \{v^{*\prime}T^{*\prime}\}'. \tag{3.3}$$

Briefly, the LIN term, which has a linear dependence on the wave anomaly, represents the contribution to heat flux from wave anomalies reinforcing or attenuating the background climatological wave. It is primarily controlled by the relative phase of the anomaly and the climatology. The NONLIN term has a quadratic dependence on the wave anomaly, and is largely determined by the anomaly amplitude and its vertical tilt. The variance of $\{v^*T^*\}'$ can be separated into contributions from LIN and NONLIN, and the covariance between them, using the general statistical relationship $\text{var}(A+B) = \text{var}(A) + \text{var}(B) + 2\text{cov}(A,B)$. That is,

$$\text{var}(\{v * T*\}') = \text{var}(\text{LIN}) + \text{var}(\text{NONLIN}) + 2\text{cov}(\text{LIN}, \text{NONLIN}). \tag{3.4}$$

3.2.3 Standing-travelling wave decomposition

The spectral decomposition defined in Section 2.2.1 is used to separate variables into standing and travelling components. In particular, as described in Section 2.3.2, given the decomposition in Eq. 2.4 of the Fourier coefficients of some signal into standing and travelling parts, one can use Eq. 2.2 to reconstruct the real-space standing and travelling parts of the signal. Applying the decomposition to the meridional wind and temperature anomalies one can then separate the LIN term into contributions from standing and travelling wave anomalies as:

$$\text{LIN} = \text{LIN}_{\text{St}} + \text{LIN}_{\text{Tr}} \tag{3.5}$$

where

$$\mathrm{LIN}_{\mathrm{St}} = \{v^*_{\mathrm{St}}{}' T^*_c\} + \{v^*_c T^*_{\mathrm{St}}{}'\} \tag{3.6a}$$

$$\mathrm{LIN}_{\mathrm{Tr}} = \{v^*_{\mathrm{Tr}}{}' T^*_c\} + \{v^*_c T^*_{\mathrm{Tr}}{}'\}. \tag{3.6b}$$

3.3 Results

3.3.1 Northern Hemisphere wintertime heat flux variance

Figure 3.1 shows the wintertime interannual variance of $\{v^*T^*\}'$ at 100hPa and averaged between 45°N and 75°N, as well the variance decomposition of the heat flux anomaly into the LIN and NONLIN terms (see Eq. 3.4), and the decomposition of the LIN term into its standing and travelling parts. The top panel shows the NDJFM-mean of the daily interannual variance of the heat flux and its components. The LIN term explains about 65% of the variance of the total heat flux anomaly, the NONLIN term about 50%, and there is a negative contribution of 15% from the covariance of the LIN and NONLIN terms. This demonstrates that on daily timescales, the LIN term is the most important contributor to the variability of heat flux anomalies, but that the NONLIN term also makes a substantial contribution. On the other hand, if, as in Smith and Kushner (2012), we first compute monthly averages of the heat fluxes before computing the interannual variance (bottom panel of Fig. 3.1), then the LIN term explains about 82% of the variance, the NONLIN term 49% and there is a larger negative contribution of -31% from the covariance. Thus, for monthly heat flux anomalies, the LIN terms makes a substantially larger contribution to the variance and this is compensated by a larger negative covariance. This suggests that the LIN term is more important on longer timescales. Section 3.3.3 will examine in more detail the dependence of the LIN and NONLIN terms as a function of length of integration.

Figure 3.1 also shows the variance decomposition of the LIN term into its standing and travelling parts. This shows that standing wave anomalies are the primary drivers of variability of the LIN term. The bottom panel of Fig. 3.1 shows this is particularly true on the longer (i.e. monthly) timescales where the LIN term dominates. This is expected because the standing waves have their peak spectral power at lower frequencies than the travelling waves (recall Fig. 2.4). We also expect the standing waves to efficiently contribute to the LIN term because their antinodes align well with the extremes of the

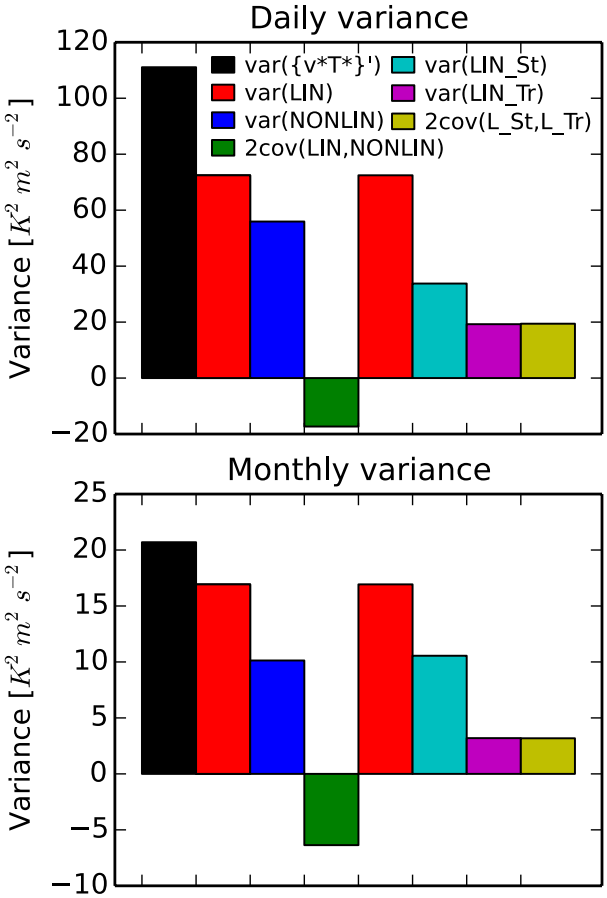

Figure 3.1: The NDJFM-mean interannual variance of $\{v^*T^*\}'$ and its various components. The heat fluxes are all at 100hPa and averaged between 45°N and 75°N. Top: interannual variance of daily heat fluxes is computed, then averaged over NDJFM. Bottom: interannual variance of monthly heat fluxes is computed, then averaged over NDJFM.

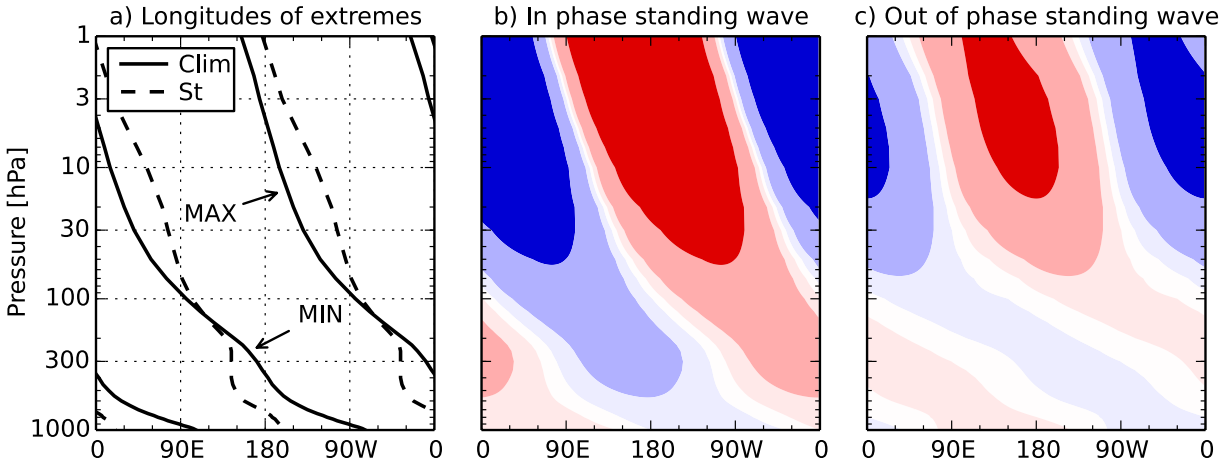

Figure 3.2: a) Solid: the longitudes of the extremes of the NDJFM-averaged wave-1 Z_c^* at 60°N, dashed: longitudes of the zonal maxima of the time-variance over all NDJFM days of wave-1 $Z_{\mathrm{St}}^{*\prime}$ at 60°N. b) The sum of the NDJFM-averaged wave-1 Z_c^* and a wave-1 mode representing a standing wave in phase with the climatology. c) As in b) except for an out of phase standing wave. See text for details. The contours for b) and c) are ±20m, ±80m, ±320m.

climatological wave at 100hPa. This is shown for wave-1, the dominant wavenumber for the LIN term, in Fig. 3.2a (see also Fig. 2.6). Overall, the standing wave-1 anomalies tend to be more barotropic than the climatology, with their extremes shifted to the west in the troposphere, and shifted to the east in the stratosphere. However, near 100hPa, there is very close alignment between the standing waves and the climatology and they are able to efficiently drive the LIN term. To illustrate the impact of the standing waves more explicitly, Figs. 3.2b-c show the sum of the NDJFM-averaged wave-1 Z_c^* at 60°N and a wave-1 mode which represents a typical standing wave in phase (Fig. 3.2b) and out of phase (Fig. 3.2c) with the climatology. This standing wave mode is constructed as follows: the phase is one of the longitudes of the extremes of the time-variance, which are given as the dashed lines in Fig. 3.2a. For the in (out of) phase standing wave the dashed line closer to the maximum (minimum) of the climatological wave is selected. The amplitude of the standing wave at each level is given by the zonal maximum of the standard deviation over all NDJFM days of $Z_{\mathrm{St}}^{*\prime}$ at that particular level. Figures 3.2b-c demonstrate that the standing waves primarily drive changes in the amplitude of the climatological wave, and additionally modify the baroclinicity of the climatological wave in the lower stratosphere and troposphere.

The greater dominance of LIN and $\mathrm{LIN}_{\mathrm{St}}$ on monthly timescales seen in Fig. 3.1 suggests that they should have longer autocorrelation timescales than the total heat flux anomaly. Smith and Kushner (2012) showed that indeed the LIN term has a longer autocorrelation timescale than the total heat flux anomaly. The next section will explore

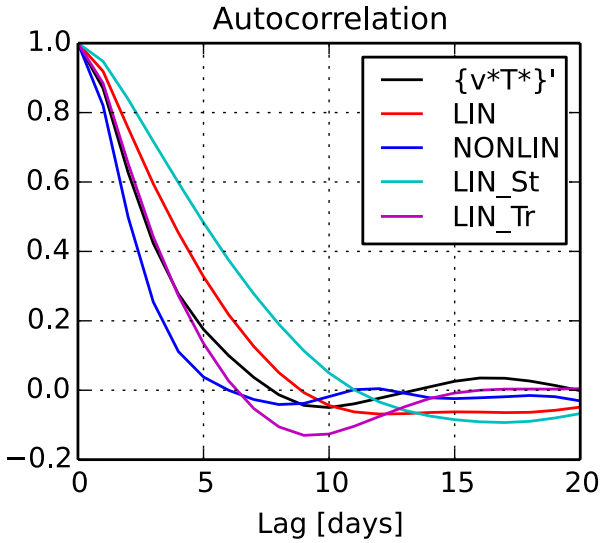

Figure 3.3: The NDJFM autocorrelation of various parts of heat flux anomaly at 100hPa and averaged between 45°N and 75°N. The autocorrelation is computed separately for each winter season, and then averaged over all years.

the drivers of the persistence of the LIN term.

3.3.2 Persistence of LIN heat flux anomalies

We show the autocorrelation of various components of the heat flux anomaly at 100hPa and 45°N-75°N in Fig. 3.3. As was shown by Smith and Kushner (2012), the LIN heat flux is more persistent than the total heat flux anomaly, which is in turn more persistent than the NONLIN heat flux. Figure 3.3 additionally shows that the autocorrelation of the $\mathrm{LIN}_{\mathrm{St}}$ term is longer than the LIN term. The $\mathrm{LIN}_{\mathrm{Tr}}$ term has an autocorrelation similar to the $\{v^*T^*\}'$ term, that is, less persistent than the LIN term. These results support what was found in Fig. 3.1: the LIN and $\mathrm{LIN}_{\mathrm{St}}$ terms explain a larger portion of the variance of the total upward wave activity flux on monthly timescales because they are more persistent than NONLIN and $\mathrm{LIN}_{\mathrm{Tr}}$ respectively.

Smith and Kushner (2012) attributed the persistence of the LIN term to the long persistence of the phase of wave-1 $Z^{*\prime}$ (see their Fig. 6b). However, the standing-travelling wave decomposition used in this study provides a different view. It demonstrates that the slow decay of autocorrelation for the phase of wave-1 at 60°N and 100hPa is actually primarily driven by the presence of a strong westward travelling wave in this region. This somewhat counter-intuitive result will be explained below. First, the autocorrelations of the phase of the total, standing and travelling parts of the wave-1 $Z^{*\prime}$ are

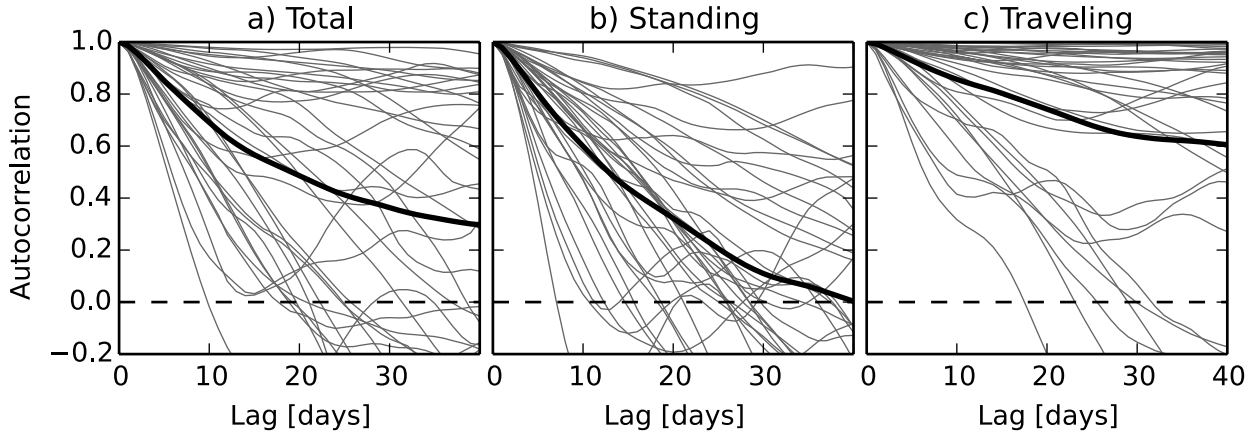

Figure 3.4: NDJFM autocorrelation of the phase of wave-1 $Z^{*\prime}$ at 60N and 100hPa, (left) the total $Z^{*\prime}$, (middle) the standing part of $Z^{*\prime}$ and (right) the travelling part of $Z^{*\prime}$. Thin grey lines are the individual autocorrelations computed over each winter season, and the thick black line is the average of the autocorrelations over all winter seasons.

shown in Fig. 3.4. In order to compute the autocorrelation of phase, we first "unwrap" each winter's timeseries of the phase so that there are no discontinuities greater than π.[2] We then compute the autocorrelation of this unwrapped timeseries. Years which have a coherent wave consistently travelling in one direction will have an unwrapped phase timeseries that is steadily decreasing (for a westward travelling wave) or increasing (for an eastward travelling wave). Since the autocorrelation of a timeseries with a pure linear trend is identically equal to 1 for any lag, this is what leads to the many winters where the autocorrelation of phase of the travelling wave-1 (Fig. 3.4c) has values near 1.0 for lags of up to 40 days. Similarly, it is what contributes to the apparent long persistence of the phase of the total wave-1 (Fig. 3.4a). However, since the persistence of the phase is due to coherent travelling waves, this means it will not necessarily enhance persistence in heat flux related to the LIN term. As an extreme case, consider a steady westward travelling wave-1 anomaly with a period of 25 days and constant amplitude. This would give a phase autocorrelation of 1.0 for any lag, but the LIN term would vary sinusoidally with the 25-day period (assuming the climatology has constant amplitude and phase). Thus, we cannot simply attribute the longer persistence of the LIN term in Fig. 3.3 to the long phase persistence seen in Fig. 3.4a.

Nevertheless, despite the discussion above, Fig. 3.4b shows that the standing wave anomaly still has a relatively long phase persistence, with an autocorrelation value of

[2]This is done as follows: proceeding through the timeseries by day, we first check if the difference between the next day and the current day is greater than π or less than $-\pi$. If the former, then we subtract 2π from all the days after the current day. If the latter, we add 2π to all the days after the current day. If neither, we do nothing and proceed to the next day.

about 0.3 after a lag of 20 days. This is substantially longer than the autocorrelation of the amplitude of wave-1 anomalies (c.f. Fig. 6b of Smith and Kushner, 2012). The standing wave phase autocorrelation is representative of how long standing anomalies tend to be fixed in place, and it shows that the low-frequency standing waves are driving the persistence of the LIN heat flux.

3.3.3 Sensitivity of vertical wave activity flux to pulse duration

Figure 3.5 shows the average heat flux anomaly and the LIN and NONLIN terms during periods of extreme heat flux anomaly, as a function of integration length. For a given integration length N, we find the periods of most extreme $\{v^*T^*\}'$ averaged over N days for each NDJFM season. We then compute the average over all winter seasons of $\{v^*T^*\}'$, LIN, NONLIN, LIN_{St} and LIN_{Tr} during these periods. This shows the contribution of different terms during periods of extreme heat flux anomaly of differing lengths. The left column in Fig. 3.5 shows the actual heat fluxes during the events, while the right column shows various components of the heat flux normalized by the total heat flux anomaly. For the daily ($N = 1$) composites, the average positive heat flux anomaly is about 30 K m s^{-1} while the average negative heat flux anomaly is about -23 K m s^{-1}. This difference is due to the positive skewness of the heat flux distribution, which will be discussed further in Chapter 4. As the averaging period becomes longer, the mean heat flux during the average period decreases in an absolute sense for both the positive and negative heat flux events. The daily (i.e. $N = 1$) heat flux events have equal contributions from the LIN and NONLIN terms for the positive events, while there is a greater contribution from the LIN term for the negative events. As the integration length increases to 20 days, a larger portion of the heat flux comes from the LIN term. This occurs for both the positive and negative heat flux events, but the change is greater for the negative events: for an integration length of 17 days, 85% of the heat flux anomaly is contributed by the LIN term. The positive heat flux events generally have at most 65% of their value contributed by the LIN term. Between 20 days and 40 days, the relative portions explained by the LIN and NONLIN terms stay roughly constant, with a slight decrease in the LIN term for the negative events. The changes in the LIN heat flux as the integration length changes are primarily driven by the standing portion of the LIN term. The travelling wave part remains constant at around 20-25% over all integration lengths.

These changes in the relative importance of the components of the heat flux as a

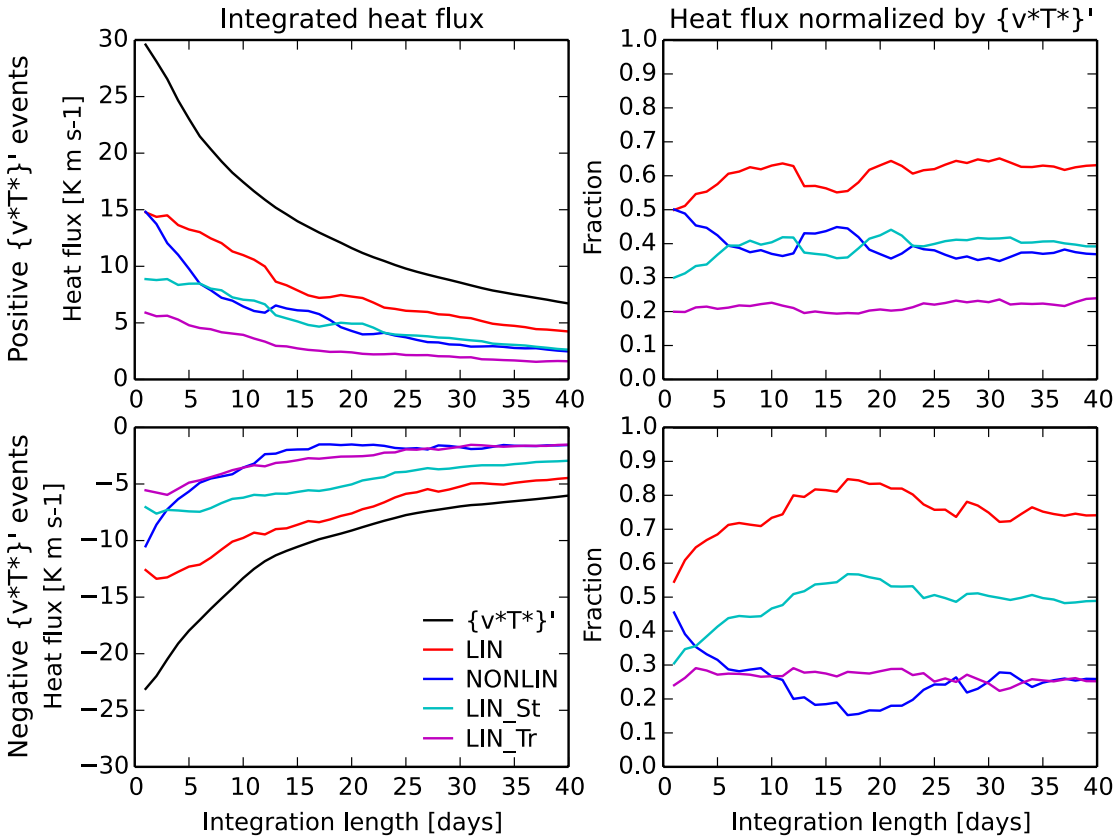

Figure 3.5: The average heat flux anomaly over the most extreme N-day running mean of each winter. For each winter season we compute an N-day running mean of $\{v^*T^*\}'$ then find the days of the most extreme positive and negative anomalies. The values of $\{v^*T^*\}'$, LIN, NONLIN, LIN_{St} and LIN_{Tr} are then composited over each winter's extreme event. Top: extreme positive heat flux anomalies, bottom: extreme negative heat flux anomalies. Left: actual mean heat flux during period, right: heat flux normalized by total heat flux anomaly.

function of pulse duration confirm what was seen in Fig. 3.1. There we saw that the LIN and LIN_{St} terms explain a larger portion of the variance of the total heat flux on monthly timescales than on daily timescales. Figure 3.5 confirms that for extreme events the same holds true: on longer (> 15 day) timescales, the LIN and LIN_{St} terms are a larger portion of heat flux pulses, at the expense of the NONLIN term. The decomposition of extreme heat flux pulses into LIN and NONLIN terms for $N = 40$ was previously examined in Smith and Kushner (2012), who showed that, in agreement with our results, negative heat flux anomalies are more driven by the LIN term than positive heat flux anomalies (see their Fig. 3).

3.3.4 Polar vortex strength connection to upward wave activity flux

We now show the connection between different components of the heat flux anomaly and polar vortex strength, as diagnosed by the NAM at 10hPa. Given that LIN_{St} is the most persistent part of the heat flux anomaly, we expect it to be most well-correlated with changes in the stratospheric NAM. This follows from the fact that polar vortex strength changes are driven by relatively long-lasting pulses of upward wave activity (Polvani and Waugh, 2004; Sjoberg and Birner, 2014). Figure 3.6 shows the lag-correlations of various quantities with the NAM at 10hPa, as a function of pressure. Focusing first on the correlation of the NAM with itself (Fig. 3.6a) we see the well-known slow downward propagation of NAM anomalies through the stratosphere, with persistent connections to the surface. Figure 3.6b shows that a weakened (strengthened) stratospheric polar vortex is typically preceded by anomalously high (low) upward wave activity flux in the stratosphere for a period of about 40 days. There is a weaker opposite signed response in the upward wave activity flux for positive lags. The total heat flux correlations for negative lags are primarily confined to the stratosphere (above 200hPa).

Comparing Figs. 3.6c-d shows that the correlations of the LIN and NONLIN terms with the stratospheric NAM have very different structures. In general the LIN correlations are similar to the total heat flux anomaly correlations, suggesting that the connection between upward wave activity flux and polar vortex strength is primarily driven by waves amplifying or attenuating the background climatology. Furthermore, the LIN term also has significant positive correlations in the troposphere for lags of up to -30 days, while the NONLIN term only has positive correlations above about 200hPa.

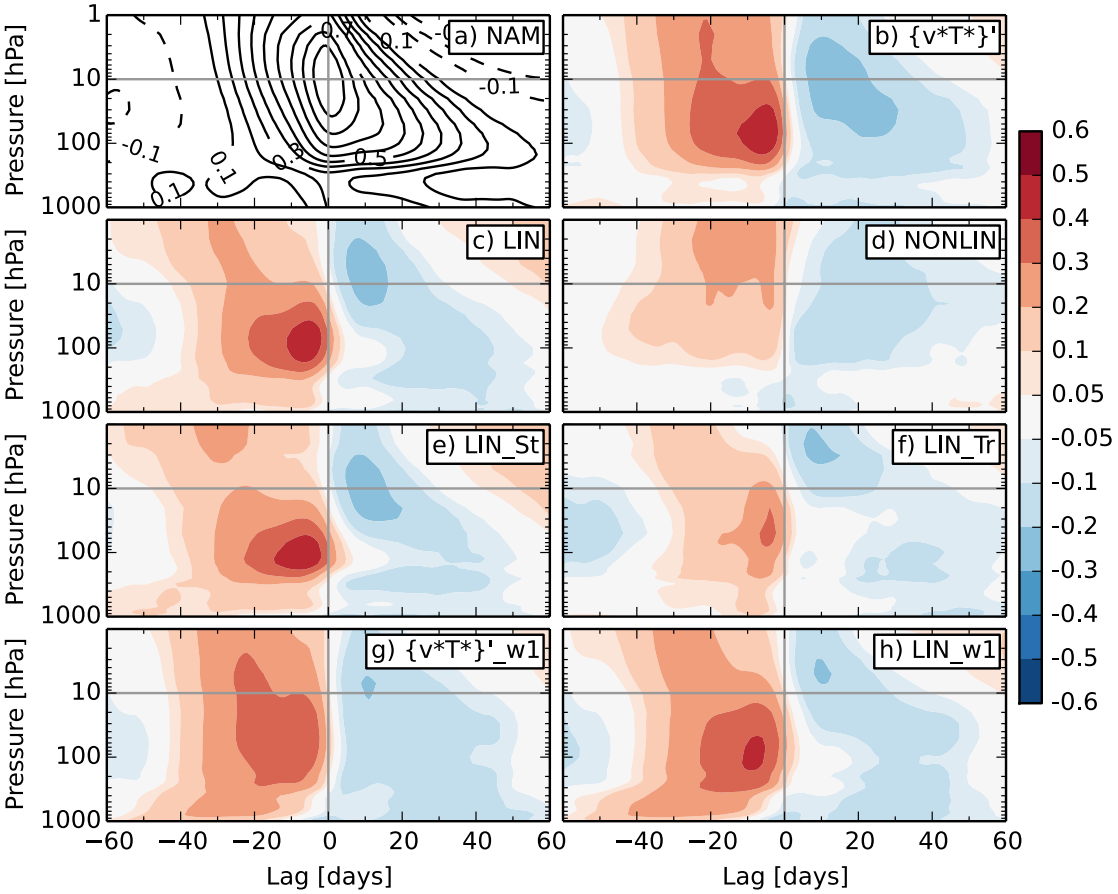

Figure 3.6: Lag-correlation as a function of height of various quantities with the NAM at 10hPa in the ERA-Interim reanalysis. Computed from all NDJFM 1979-2013 days. a) lag-correlation of NAM at various heights with the NAM at 10hPa, contour intervals are 0.1, with the zero contour omitted. All other panels are the lag-correlation of different components of heat flux anomaly at various heights with the NAM at 10hPa. In particular: b) total heat flux anomaly, c) LIN, d) NONLIN, e) $\mathrm{LIN}_{\mathrm{St}}$, f) $\mathrm{LIN}_{\mathrm{Tr}}$, g) wave-1 heat flux anomaly, h) wave-1 LIN.

This shows that the LIN term is responsible for driving the connection between upward wave activity flux generated in the troposphere and polar vortex strength. Finally, the correlations of the LIN term are dominated by the standing wave contribution. This is seen in Figs. 3.6e and 3.6f: the $\mathrm{LIN_{St}}$ correlation pattern is very similar to the total LIN pattern, while the $\mathrm{LIN_{Tr}}$ correlations are more short-lived and weaker.

Figure 3.6b showed that correlations between tropospheric heat flux and stratospheric polar vortex strength are very weak to nonexistent. However, we know from Charney and Drazin (1961) that only waves with the largest horizontal scales are able to propagate from the troposphere to stratosphere during typical winter conditions. For this reason, we additionally show the correlations for the wave-1 component of $\{v^*T^*\}'$ and LIN in Figs. 3.6g-h. A stronger (> 0.2) correlation is now seen between tropospheric heat flux and the 10hPa NAM, especially for lags of -15 to -40 days. There is also a weak positive correlation in the troposphere at a lag of more than a month, before the peak stratospheric signal. The correlations of the wave-1 component of LIN are very similar to the total wave-1 heat flux anomaly. The NONLIN correlations are weak throughout for wave-1 and the wave-1 LIN correlations are primarily due to the standing wave part (not shown).

We estimate the statistical significance of the preceding lag-correlations using a method described in Lau and Chan (1983). This technique calculates a confidence interval by assuming each timeseries is a first-order Markov process and computing their autocorrelation timescales. Thus, the statistical significance of the correlations will vary depending on the predictor variable, and also be a function of height and lag (since for greater lags there are fewer data points with which to compute the correlations). See Lau and Chan (1983) for details of the computation. Broadly speaking, the lag-correlations of the NAM with itself (Fig. 3.6a) are significant at the 95% level at values of 0.10 to 0.13 in the troposphere and upper stratosphere, and at 0.12 to 0.16 in the lower stratosphere where the NAM is most persistent. The lag-correlations between the heat fluxes and the NAM (Figs. 3.6b-h) are significant at 95% for lower values of the correlation because the heat flux is less persistent than the NAM. The total heat flux anomaly correlations (Fig. 3.6b) are significant for values of about 0.05 to 0.07 in the troposphere, and 0.07 to 0.10 in the stratosphere. The other correlations are significant at approximately the same values for the NONLIN term, and at slightly higher values for LIN and wave-1 components since they are more persistent.

3.3.5 Vortex strength connection to wave activity flux in models

Figures 3.7 and 3.8 show the same diagnostics as Fig. 3.6 for, respectively, the high-top and low-top versions of the CMAM model. It is apparent that the simulations with the high-top version of the model (Fig. 3.7) broadly capture the same lag-correlation structure seen in the ERA-Interim reanalysis. The primary difference is that the heat flux correlations are slightly higher in the CMAM simulations for lags of -20 to 0 days. This is especially for the $\mathrm{LIN_{Tr}}$, which causes the correlations for $\mathrm{LIN_{St}}$ and $\mathrm{LIN_{Tr}}$ to be more similar for CMAM as compared to ERA-Interim. This is in accordance with the fact that $\mathrm{LIN_{Tr}}$ explains a slightly larger portion of the variance of LIN in the high-top CMAM compared to ERA-Interim, and that the $\mathrm{LIN_{St}}$ and $\mathrm{LIN_{Tr}}$ terms have more similar persistences timescales in the model simulations (not shown). On the other hand, the lag-correlations in the low-top version of the CMAM model (Fig. 3.8) are markedly different from those seen in the reanalysis. In general the heat flux correlations for negative lags are too large and begin at earlier lags than in ERA-Interim. This is particularly true for the LIN and $\mathrm{LIN_{St}}$ terms, and less so for the $\mathrm{LIN_{Tr}}$ term. Furthermore, there is no significant correlation between NONLIN and the stratospheric NAM for negative lags. And finally, there is a lack of negative correlations between the heat flux and NAM for positive lags, except for the NONLIN term. This comparison of high-top and low-top simulations demonstrates the importance of simulating the stratosphere for properly representing the influence of upward wave activity flux on the polar vortex strength. It also shows that the connections found in the ERA-Interim reanalysis can be reasonably well represented by a model with a well-resolved stratosphere.

Figure 3.9 shows the lag-correlations of various heat flux components and the stratospheric NAM as above but for simulations with the CNRM-CM5 model (Voldoire et al., 2013).[3] These unpublished runs were originally performed in order to investigate the dependence of decadal predictability on stratospheric resolution. The high-top version has 91 vertical levels up to 0.01hPa, and the low-top version has 62 vertical levels to 5hPa. Both have a horizontal resolution of T63. Ten realizations were run for 10 years each, starting 1 January 1981, 1986, 1991, 1996, and 2001. Thus, 450 complete ND-JFM winter seasons which span the years 1981-2010 are available for each version of the model. Figure 3.9 shows the lag-correlations between various components of the heat

[3]Note the experiments analyzed were not run with the same resolution as the simulations discussed in Voldoire et al. (2013).

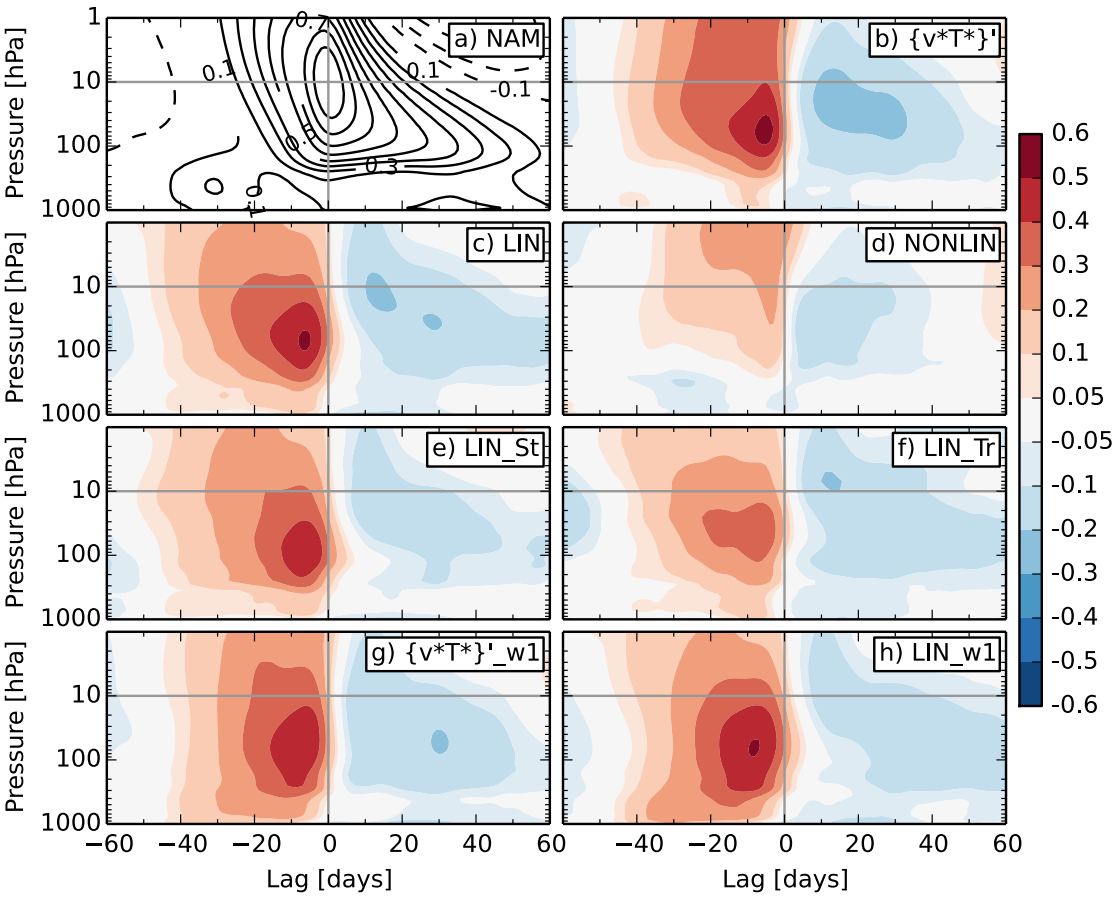

Figure 3.7: Lag-correlation as a function of height of various quantities with the NAM at 10hPa in the high-top version of the CMAM model. Computed from 40 years of NDJFM days. Panels as in Fig. 3.6.

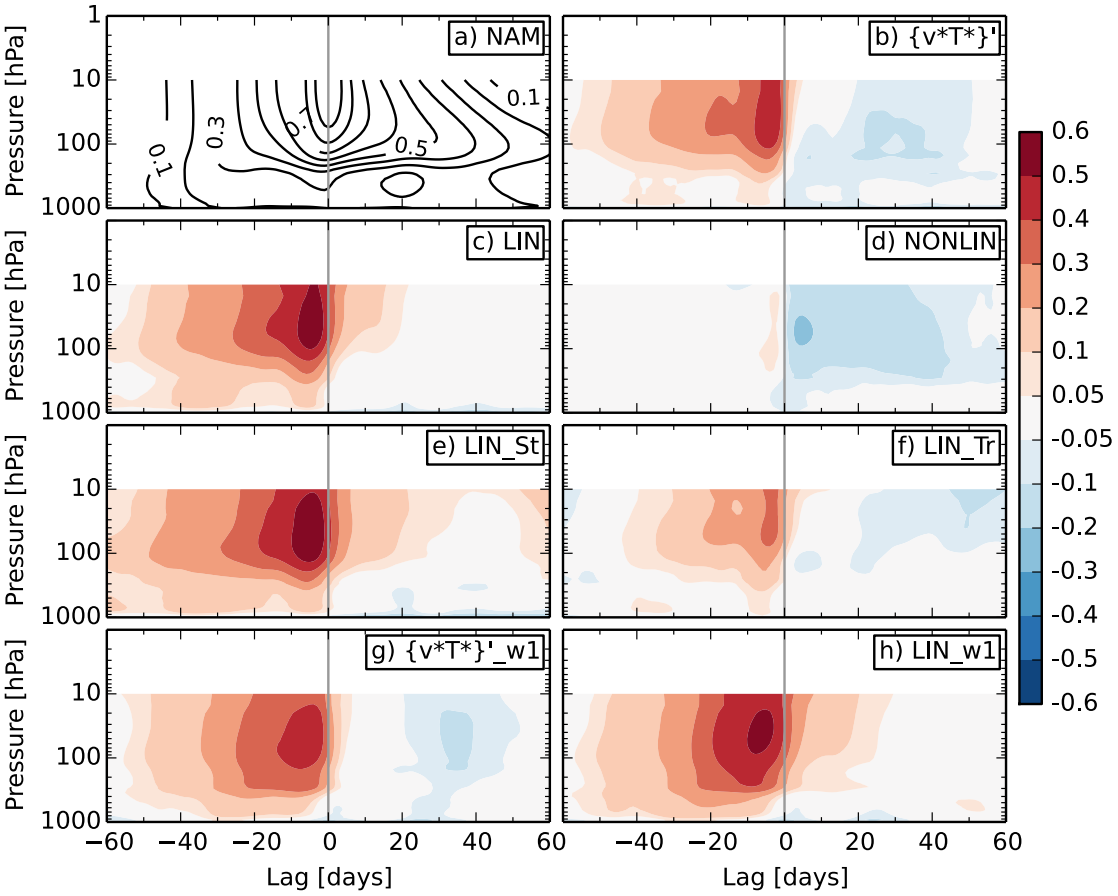

Figure 3.8: Lag-correlation as a function of height of various quantities with the NAM at 10hPa in the low-top version of the CMAM model. Computed from 40 years of NDJFM days. Panels as in Fig. 3.6.

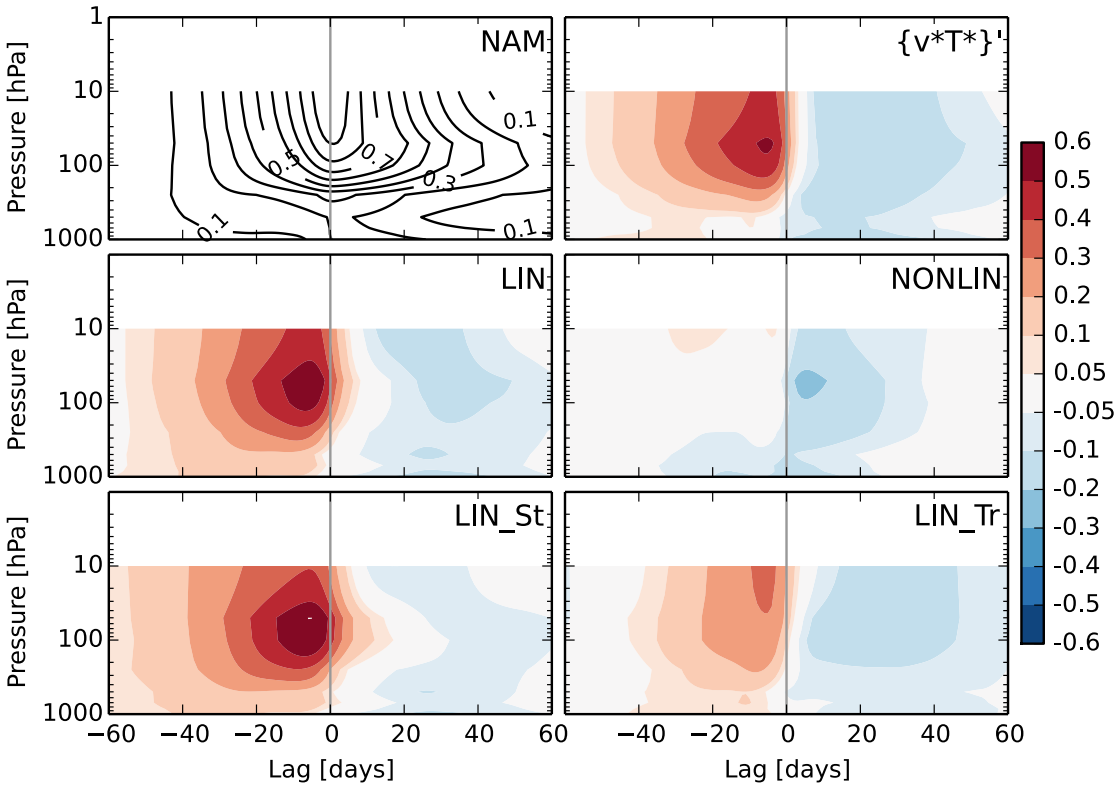

Figure 3.9: Lag-correlation as a function of height of various quantities with the NAM at 10hPa in the CNRM-CM5 high-top model. Computed from 450 NDJFM seasons spanning 1981-2010. Top left: lag-correlation of NAM at various heights with the NAM at 10hPa, contour intervals are 0.1, with the zero contour omitted. All other panels are the lag-correlation of different components of heat flux anomaly at various heights with the NAM at 10hPa. Although this model had a top at 0.01hPa, output was only saved on levels up to 10hPa.

flux anomaly and the NAM at 10hPa for the high-top version of the model. Compared to the ERA-Interim reanalysis, the correlations between the total heat flux anomaly and the NAM are similar, but in general slightly too strong and also begin at too large of a negative lag. This also holds for the LIN and $\mathrm{LIN_{St}}$ correlations. As well, there is no significant correlation between the NONLIN term and the NAM for negative correlations in the stratosphere, which is markedly different than the results for the reanalysis, and the high-top version of CMAM. This suggests that despite the good stratospheric resolution in the high-top version of CNRM-CM5, it is still not properly representing some aspect of the large-scale dynamics. Finally, the LIN correlations are strongly dominated by the $\mathrm{LIN_{St}}$ component, whereas the $\mathrm{LIN_{Tr}}$ correlations are much weaker and shorter-lived. The low-top version of the CNRM-CM5 model has very similar results, with just slightly stronger correlations seen for negative lags for the total heat flux anomaly and the LIN terms (not shown).

3.3.6 Linear interference and SSWs

It is particularly important to be able to predict the extremes of stratospheric variability because they tend to be followed by persistent anomalies in the troposphere (e.g. Sigmond et al., 2013). In this section we show the heat flux precursors to sudden stratospheric warmings (SSWs) in the reanalysis for 1979-2013. This was shown for the LIN and NONLIN terms in Smith and Kushner (2012), and here we extend the analysis to the $\mathrm{LIN_{St}}$ and $\mathrm{LIN_{Tr}}$ components.[4] We make separate composites over displacement and split SSWs as discussed in Section 3.2.1. Figure 3.10 shows the composite of the NAM and various components of the heat flux at all levels, from 30 days preceding to 30 days following displacement and split SSWs. The NAM panels show the strong deceleration of the polar vortex, with NAM values exceeding 3 and 3.5 standard deviations for the displacement and split composites, respectively. As expected, preceding the SSW events are anomalously large values of upward wave activity flux for lags of up to 25 days, throughout the stratosphere and intermittently in the troposphere. The displacement events show a persistent anomaly exceeding one standard deviation for about 25 days before the event, and a stronger positive anomaly of up to two standard deviations in the lower stratosphere for lags of -5 to 0 days. The split events on the other hand have weaker precursors from lags of -25 to -10 days, but are preceded by heat flux anomalies of

[4]Smith and Kushner (2012) showed composites over SSW events in the 1958-2009 period in the NCEP/NCAR reanalysis.

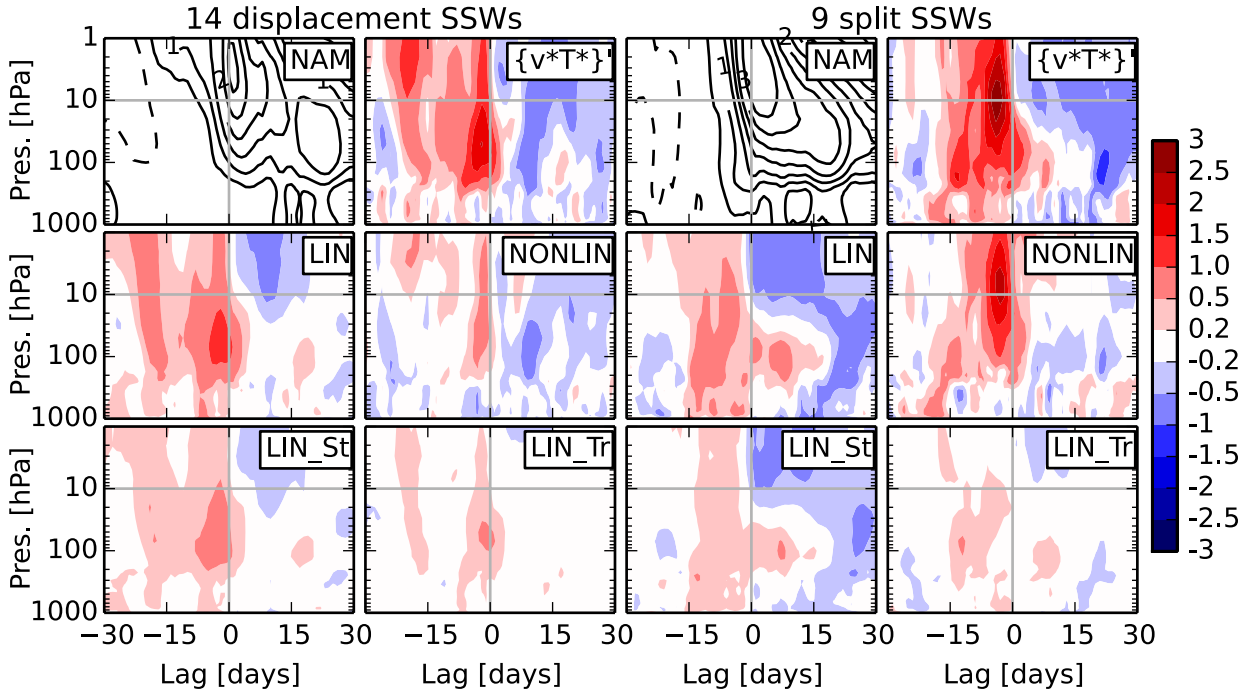

Figure 3.10: Composite of NAM and heat fluxes over 14 displacement SSWs (left) and 9 split SSWs (right) in the 1979-2013 ERA-Interim reanalysis. All of the heat fluxes are normalized by the level-dependent standard deviation of $\{v^*T^*\}'$, computed over all NDJFM days. The contour intervals for the NAM panels are 0.5, with the zero contour omitted.

above two standard deviations throughout lower to mid stratosphere from -8 to -2 days lag.

The second row of Fig. 3.10 shows the LIN and NONLIN signatures associated with the displacement and split SSWs. The persistent heat flux anomaly preceding displacement events is largely made up of the LIN term, with a short contribution from the NONLIN term just before lag-0. The split events have a weaker LIN signature for negative lags, in agreement with the weaker total heat flux precursors at longer lags associated with the split events, but have a much larger contribution from the NONLIN term for about 7 days preceding the events. The third row of Fig. 3.10 shows the composites of $\mathrm{LIN_{St}}$ and $\mathrm{LIN_{Tr}}$ during the SSW events. This demonstrates that the positive LIN anomaly preceding displacement SSWs is primarily driven by standing waves. Overall, Fig. 3.10 shows that displacement events have longer lead-time heat flux precursors, which consist of an amplification of the climatological wave by a standing wave anomaly. On the other hand, split events have a stronger but short-lived heat flux signature, which is a result of the wave anomaly interacting with itself (i.e. the NONLIN term). This suggests that displacement events may be more predictable than split events, and that tracking the standing wave field would be important for the prediction of displacement

SSWs.

3.4 Conclusion and discussion

This chapter examined whether standing or travelling waves primarily drive the linear interference effect. It was shown that standing waves explain the largest portion of the variance of the LIN term, an effect that is enhanced at lower frequencies where standing wave variability dominates. This is because the standing waves are well-aligned with climatology, and hence can efficiently drive amplification and attenuation of the climatological wave. The standing waves are also dominated by low frequencies, and have a long-lived phase persistence. As a consequence of this, the standing part of the LIN term has a longer autocorrelation timescale than the other components of the upward wave activity flux. Consequently, it also explains a larger portion of the variance on monthly timescales than on daily timescales. This also holds for extreme heat flux anomalies: as the duration of wave activity pulses increases, a larger portion is explained by the LIN and $\mathrm{LIN}_{\mathrm{St}}$ terms.

The fact that standing waves drive the most persistent part of the wave activity flux suggests that they should be primarily responsible for the connection between wave driving and stratospheric polar vortex strength. This is confirmed in reanalysis data, and it is verified that an atmospheric model with a well-resolved stratosphere is able to simulate this connection well. Furthermore, the correlations between the LIN term and the polar vortex strength in the reanalysis data show clear tropospheric precursors preceding polar vortex strength by about a month. This connection is dominated by the wave-1 component of the LIN term. Finally, the upward wave activity flux precursors of SSWs are computed. As expected, weakening of the polar vortex is preceded by anomalously large upward wave activity flux. However, the duration and form of this flux depends on the type of SSW. Displacement events have longer-lived precursors which are primarily driven by the LIN term being forced by standing waves. On the other hand, split SSWs have shorter wave activity flux precursors, and they are dominated by the NONLIN term.

Some previous studies have considered the impact of travelling waves interfering with a stationary or "quasi-stationary" background wave (Madden, 1975; Holton and Mass, 1976; Lindzen et al., 1982; Salby and Garcia, 1987). They have used theory, mech-

anistic models and observational data to understand this effect, but are actually studying a somewhat different phenomenon than the focus of this work. Here, we decompose the wave anomaly into standing and travelling components, and quantify how each of these terms interfere with the climatology and drive the LIN term. The studies cited above take a different approach: they consider just the separation of waves into a stationary (either a climatological or a time-mean component) part and an anomaly that is assumed to be travelling with some fixed phase speed. However, as we have shown, typical wave anomalies in the atmosphere consist of standing-type variability and travelling-type variability. Hence, we believe our analysis is more complete, and is applicable to understanding the linear interference phenomenon as discussed in the introduction. Nevertheless, it would be interesting to apply the standing-travelling wave decomposition to the total wave fields (climatology + anomaly) and directly investigate the role of each of these wave types without invoking interference between the climatology and anomalies.

A practical implication of the results shown in this study is the potential for longer-range prediction of polar vortex strength changes, and consequently the sub-seasonal prediction of the wintertime tropospheric NAM. Clear tropospheric precursors in upward wave activity flux have been found to lead NAM changes in the stratosphere by a month. These precursors are dominated by standing waves driving the LIN term. This suggests that dynamical prediction systems must accurately represent the climatological wave structure and the standing wave anomalies to properly model this coupling. In addition, monitoring of the LIN term and the standing wave structure may be helpful for predicting polar vortex strength changes. To make such a scheme practical operationally, additional technical work is needed to extract standing/travelling signals using a digital filter in the time domain rather than in the frequency domain.

Chapter 4

Why are winter polar stratospheric temperatures and heat fluxes positively skewed?

4.1 Introduction

Since early work documenting the variability of the Northern Hemisphere stratospheric polar vortex, it has been known that the distribution of temperatures in the wintertime vortex is positively skewed (e.g. see Fig. 2 of Labitzke (1982) and Fig. 4.1).[1] The typical explanation for a positively skewed distribution in winter temperatures is that dynamical wave driving can force relatively large positive anomalies in temperature (and coincident weakening in the stratospheric circulation) while there is a firm lower bound on temperatures set by radiative cooling (Gillett et al., 2001). However, recent work has shown that wave driving can also force vortex accelerations and negative temperature anomalies in the polar stratosphere (Shaw and Perlwitz, 2013, 2014; Dunn-Sigouin and Shaw, 2015). In addition, as will be shown in this chapter, the upward wave activity flux distribution is itself positively skewed in the lower stratosphere. Given the strong connection between upward wave activity flux in the lower stratosphere and polar vortex temperatures (Newman et al., 2001; Polvani and Waugh, 2004), these two facts suggest that it is possible that the positive skewness of the temperature distribution is actually

[1]Throughout this chapter, the skewness is calculated as the scaled third moment of the distribution, i.e. using the formula $s = \mathrm{E}[(x-\mu)^3]/\sigma^3$, where μ is the mean and σ the standard deviation of the given distribution x (e.g. Section 2.6.7 of von Storch and Zwiers, 1999).

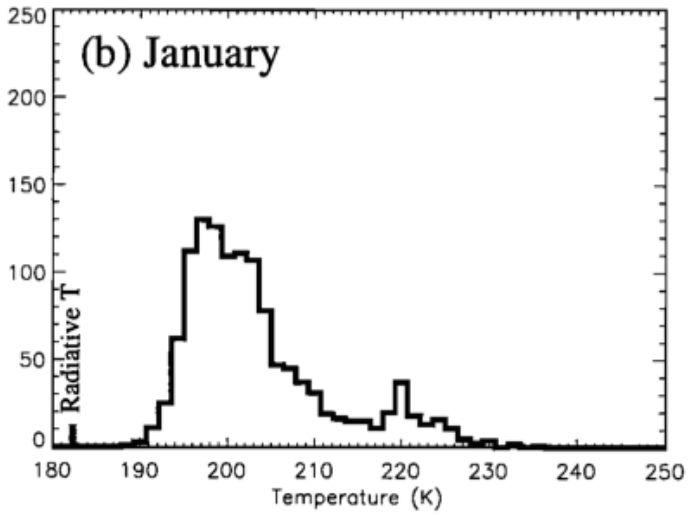

Figure 4.1: Histogram of daily January National Centers for Environmental Prediction (NCEP) 70-hPa North Pole temperature over the period 1958-1997. The corresponding radiatively determined temperature is shown for comparison. Reproduced from Fig. 6 of Gillett et al. (2001).

more dynamically controlled than typically thought.

There are a number of reasons why it is important to understand the distribution of temperatures in the stratosphere. First of all, the lower (cold) end of the distribution is fundamental for ozone chemistry, and in particular photochemical ozone loss, in the stratosphere. Some winters with extended anomalously cold temperatures, like the 2010/11 one, have led to substantial amounts of ozone loss in the Northern Hemisphere (e.g. Manney et al., 2011). Second, the extreme warm conditions in the polar stratosphere are associated with weak polar vortex events, which tend to be followed by a persistent negative NAM signature in the troposphere (see Section 1.3). Because of this, knowledge of the conditions determining stratospheric circulation extremes can improve predictability of tropospheric weather.

Although our ultimate goal is to explain the distribution of temperatures in the stratosphere, as a first step we will here focus on simply explaining the positive skewness of the upward wave activity flux distribution. This chapter will develop a simple model for this distribution, appealing to the ideas of linear interference introduced in Section 1.4 and discussed in more detail in Chapter 3. We will begin by outlining the observed distributions of temperature and upward wave activity flux in the stratosphere. Next we will show a novel result that, when examined by individual wavenumber, there is a clear nonlinear relationship between LIN and NONLIN. An argument based on wave anomaly tilts is proposed to explain this relationship, and it is used to provide an explanation for

the positive skewness of upward wave activity flux. Finally, a simple model of wave interference is developed in order to explore the key parameters that set the positive skewness of the wave activity flux distribution. It is shown that highly simplified distributions of the wave anomalies can be used, but that for the wave-1 Northern Hemisphere heat flux distribution, the westward tilt with height of the climatological wave is essential. While this analysis focuses on the Northern Hemisphere's largest horizontal scale, planetary wave-1, Section 4.3.6 will briefly describe the distributions for wave-2 heat flux and the Southern Hemisphere.

4.2 Data and methods

4.2.1 Data

As in Chapters 2 and 3, the 1979-2013 daily-mean geopotential height, meridional wind and temperature data on a $1.5° \times 1.5°$ grid from the ERA-Interim reanalysis are used (Dee et al., 2011). Furthermore, the same notation for deviations from the climatology and zonal mean are used. Differently than Chapter 3, we will focus on the heat flux anomaly at 60°N, not averaged between 45°N and 75°N. We do this because we will ultimately be aiming to explain the heat flux distribution by appealing to simple properties of the wave anomaly such as its amplitude, phase and tilt. These properties are defined at a single latitude, and thus we focus on just 60°N. Regardless, the correlation between 100hPa $\{v^*T^*\}'$ at 60°N and that averaged between 45°N and 75°N, computed over all DJF days, is 0.97 for wave-1 and 0.98 for wave-2, and so we would not expect a major qualitative change in the results if we were to use the meridionally averaged heat flux. In general, our focus will be on the wave-1 component of the heat flux, since this is the dominant term in the lower stratosphere, but a comparison with wave-2 will be discussed in Section 4.3.6. The focus will be on active stratosphere-troposphere coupling seasons, that is, December-February (DJF) in the Northern Hemisphere (Fig. 2 of Smith and Kushner (2012)), and September-November (SON) in the Southern Hemisphere (Fig. 9 of Smith and Kushner (2012); see also Thompson and Wallace (2000)).

4.2.2 Toy model of wave interference

In Section 4.3.4 a simple model of wave interference will be used to examine the importance of various aspects of the climatological wave and of the wave anomaly distribution for the positive skewness of the heat flux distribution. Here, the model is described. We consider the geopotential height anomaly and climatology and use hydrostatic and geostrophic balance to compute the corresponding temperature and meridional wind, and thus heat flux. We will consider one wavenumber at a time. Because we are interested in the heat flux at one particular latitude and pressure level, we just need the amplitude, phase and tilt of the wave anomaly and of the climatology at that level (the tilt is necessary in order to compute the temperature from the geopotential height). The observed distributions of these three parameters for wave-1 in the high-latitude lower stratosphere will be shown in Section 4.3.3. Expressions for the heat flux, as well as the LIN and NONLIN terms, as a function of the wave amplitude, phase and tilt are derived now. It is assumed the wave at some particular latitude and time takes the form

$$Z^*(\lambda, p) = A(p)\cos\left[k\lambda - \theta(p)\right] \tag{4.1}$$

where $A(p)$ is the pressure-dependent wave amplitude, k is the zonal wavenumber and $\theta(p)$ the pressure-dependent wave phase. Given the typical scaling of the wave amplitude as the square root of density (e.g. Eq. 4.2.3a of Andrews et al. (1987)) we will assume that

$$A(z) = A_0 e^{z/2H} \tag{4.2}$$

with $A_0 = A(z_0)$, $z = H\ln(p_0/p)$ and H a density scale height. This can be shown to imply

$$A(p) = A(p_0)\sqrt{\frac{p_0}{p}} \tag{4.3}$$

and

$$\frac{dA}{d\ln p} = -H\frac{dA}{dz} = -\frac{A}{2}. \tag{4.4}$$

Figure 4.2 tests how well Eq. 4.3 holds for wave-1 in the lower stratosphere by plotting the actual amplitudes at levels adjacent to 100hPa (that is, at 125hPa and 70hPa) against estimates of the amplitude at these levels computed using the true amplitude at 100hPa and Eq. 4.3. The high correlations ($r = 0.97$ and $r = 0.95$) between the estimated and true amplitudes, and the fact that their relationship falls on the one-to-one line (Fig. 4.2) indicates the appropriateness of the assumption of wave amplitude being proportional to

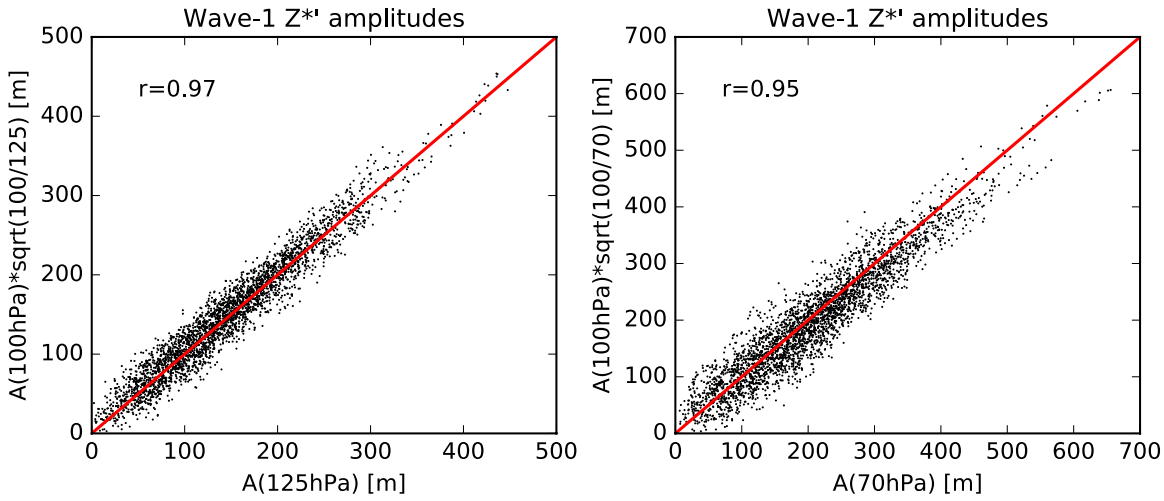

Figure 4.2: The amplitude of wave-1 $Z^{*\prime}$ at 60°N and (left) 125hPa (right) 70hPa versus the estimated amplitudes at each of these levels calculated with Eq. 4.3. The 1-to-1 line is plotted in red. Correlations are shown in the upper-left of each plot.

the square root of density. Equation 4.4 will be used below when deriving an expression for the temperature in terms of the phase, amplitude and tilt of the geopotential height wave.

Next, hydrostatic balance (e.g. Eq. 1.1.4 of Andrews et al. (1987)) is used to compute the temperature from Eq. 4.1:

$$\begin{aligned} T^*(\lambda, p) &= -\frac{g}{R}\frac{\partial Z^*}{\partial \ln p} \\ &= -\frac{g}{R}\frac{dA(p)}{d\ln p}\cos\left[k\lambda - \theta(p)\right] - \frac{g}{R}A(p)\frac{d\theta(p)}{d\ln p}\sin\left[k\lambda - \theta(p)\right]. \end{aligned} \tag{4.5}$$

And substituting in Eq. 4.4:

$$T^*(\lambda, p) = \frac{g}{R}A(p)\left(\frac{1}{2}\cos\left[k\lambda - \theta(p)\right] - \frac{d\theta(p)}{d\ln p}\sin\left[k\lambda - \theta(p)\right]\right). \tag{4.6}$$

In the above equation, $\frac{d\theta(p)}{d\ln p}$ is the tilt of the wave. It is positive for a westward tilting wave (since phase increases for increasing pressure) and negative for an eastward tilting wave. Now applying the assumption of geostrophic balance to compute the meridional

wind (e.g. Eq. 5.2.4 of Andrews et al. (1987)), we find

$$\begin{aligned} v^*(\lambda,p) &= \frac{g}{f}\frac{1}{a\cos(\phi)}\frac{\partial Z^*}{\partial \lambda} \\ &= -\frac{kg}{f}\frac{1}{a\cos(\phi)}A(p)\sin\left[k\lambda-\theta(p)\right] \end{aligned} \tag{4.7}$$

where g is the acceleration due to gravity, a is the radius of the Earth, ϕ is the latitude and f is the Coriolis frequency. Using Eqs. 4.6 and 4.7, the total heat flux for a single wavenumber perturbation is

$$\begin{aligned} \{v^*T^*\} &= \frac{1}{2\pi}\int_0^{2\pi} v^*(\lambda,p)T^*(\lambda,p)\,d\lambda \\ &= \frac{kg^2A^2}{2\pi f Ra\cos(\phi)}\left[-\frac{1}{2}\int_0^{2\pi}\cos(k\lambda-\theta)\sin(k\lambda-\theta)d\lambda \right. \\ &\qquad \left. +\frac{d\theta}{d\ln p}\int_0^{2\pi}\sin^2(k\lambda-\theta)d\lambda\right] \\ &= \frac{kg^2A^2}{2fRa\cos(\phi)}\frac{d\theta}{d\ln p}. \end{aligned} \tag{4.8}$$

The NONLIN term (recall Eq. 1.13) can be calculated from the above by using the wave anomalies instead of the total wavefields. That is,

$$\text{NONLIN} = \frac{kg^2(A')^2}{2fRa\cos(\phi)}\frac{d\theta'}{d\ln p} - \left[\frac{kg^2(A')^2}{2fRa\cos(\phi)}\frac{d\theta'}{d\ln p}\right]_c \tag{4.9}$$

where A' and $\frac{d\theta'}{d\ln p}$ are the amplitude and tilt of the anomalous wave. The second term in Eq. 4.9 guarantees that the NONLIN term has zero climatological mean. Equation 4.9 explicitly shows that the NONLIN term has a quadratic dependence on the amplitude of the wave anomaly, and a linear dependence on the phase tilt. In particular it will be greater for a westward tilting wave, and smaller for an eastward tilting wave.

For the LIN term we must consider the fact that the wave phases, tilts and amplitudes will be different for the climatology versus the anomaly. Below an expression for the LIN term in terms of the anomaly amplitude, phase and tilt and climatology amplitude, phase and tilt is derived. With the anomaly and climatology geopotential heights given by

$$Z^{*\prime}(\lambda,p) = A'(p)\cos\left[k\lambda-\theta'(p)\right], \quad Z^*_c(\lambda,p) = A_c(p)\cos\left[k\lambda-\theta_c(p)\right], \tag{4.10}$$

and making the same assumptions for the amplitude height dependence and geostrophic and hydrostatic balance as above, it can be shown that

$$\begin{aligned}\{v_c^* T^{*\prime}\} &= \frac{1}{2\pi}\int_0^{2\pi} v_c^* T^{*\prime} d\lambda \\ &= \frac{g^2 k A_c A'}{2\pi f a R\cos(\phi)}\left[-\frac{1}{2}\int_0^{2\pi}\sin(k\lambda-\theta_c)\cos(k\lambda-\theta')d\lambda \right. \\ &\qquad \left. + \frac{d\theta'}{d\ln p}\int_0^{2\pi}\sin(k\lambda-\theta_c)\sin(k\lambda-\theta')d\lambda\right] \\ &= \frac{g^2 k A_c A'}{2 f a R\cos(\phi)}\left[-\frac{1}{2}\sin(\theta'-\theta_c) + \frac{d\theta'}{d\ln p}\cos(\theta'-\theta_c)\right]. \end{aligned} \tag{4.11}$$

And similarly,

$$\begin{aligned}\{v^{*\prime} T_c^*\} &= \frac{1}{2\pi}\int_0^{2\pi} v^{*\prime} T_c^* d\lambda \\ &= \frac{g^2 k A_c A'}{2\pi f a R\cos(\phi)}\left[-\frac{1}{2}\int_0^{2\pi}\sin(k\lambda-\theta')\cos(k\lambda-\theta_c)d\lambda \right. \\ &\qquad \left. + \frac{d\theta_c}{d\ln p}\int_0^{2\pi}\sin(k\lambda-\theta')\sin(k\lambda-\theta_c)d\lambda\right] \\ &= \frac{g^2 k A_c A'}{2 f a R\cos(\phi)}\left[\frac{1}{2}\sin(\theta'-\theta_c) + \frac{d\theta_c}{d\ln p}\cos(\theta'-\theta_c)\right]. \end{aligned} \tag{4.12}$$

Thus,

$$\begin{aligned}\mathrm{LIN} &= \{v_c^* T^{*\prime}\} + \{v^{*\prime} T_c^*\} \\ &= \frac{g^2 k A_c A'}{2 f a R\cos(\phi)}\left(\frac{d\theta'}{d\ln p} + \frac{d\theta_c}{d\ln p}\right)\cos(\theta'-\theta_c). \end{aligned} \tag{4.13}$$

Equation 4.13 explicitly demonstrates the dependence of the LIN term on the difference between the phase of the wave anomaly and the climatological wave. Assuming that both the anomalous and climatological waves have a westward tilt with height, that is, $\frac{d\theta'}{d\ln p} > 0$ and $\frac{d\theta_c}{d\ln p} > 0$, then the sign of LIN is determined by the relative phases of the climatological and anomalous waves. It will be positive if $|\theta' - \theta_c| < \pi/2$ and negative otherwise. Furthermore, Eq. 4.13 shows the LIN term has a linear dependence on the anomaly amplitude, and depends on the sum of the tilts of the climatological and anomalous wave. If the anomalous wave has an eastward tilt with height that is of comparable magnitude to the climatology's westward tilt, the LIN term will be close to zero. Because of this, a strongly positive or negative LIN is an indication of a westward

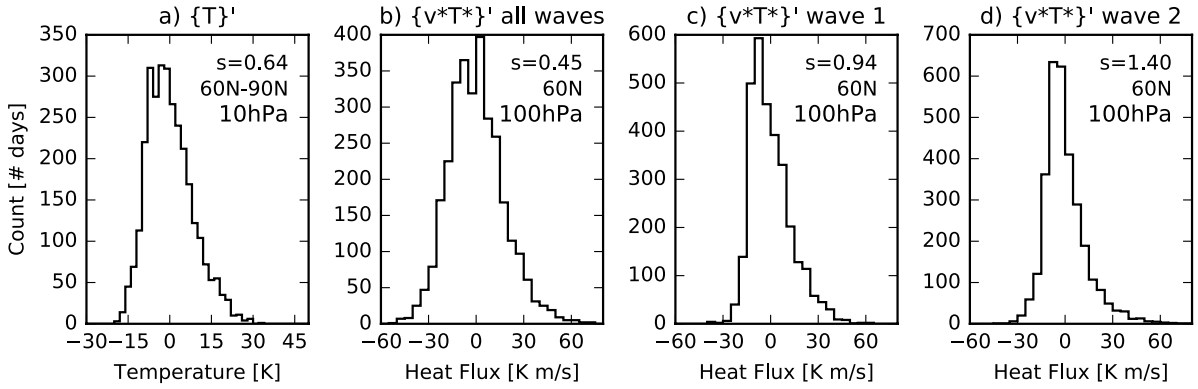

Figure 4.3: Daily histograms over all DJF days of a) $\{T\}'$ at 10hPa and averaged from 60°N to 90°N with a cosine of latitude weighting, b) $\{v^*T^*\}'$, c) wave-1 $\{v^*T^*\}'$ and d) wave-2 $\{v^*T^*\}'$ all at 100hPa and 60°N. The skew of each distribution is written in the top-right of each panel.

tilted anomalous wave.

The dependencies of the LIN and NONLIN terms on the wave amplitudes, tilts and phases has been noted qualitatively by previous authors (e.g. Smith and Kushner, 2012) but until now have not been demonstrated explicitly analytically.

4.3 Results

4.3.1 Temperature and heat flux distributions

Polar stratospheric temperatures in the Northern Hemisphere winter are known to be positively skewed (Labitzke, 1982; Gillett et al., 2001). This section documents the temperature distributions and additionally shows that the lower-stratospheric heat flux distribution is positively skewed. Figure 4.3 shows the daily histograms of DJF polar-cap temperature in the mid-stratosphere, and high-latitude heat flux in the lower stratosphere. The polar-cap stratospheric temperature anomalies have a range of approximately -20K to 30K, and have a skew of 0.64 (Fig. 4.3a). The heat flux at 100hPa and 60°N is also positively skewed, with values of 0.45, 0.94 and 1.40 for the total, wave-1 and wave-2 components respectively. Section 4.3.2 will propose an explanation for the positive skewness of the wave-1 and wave-2 heat flux based on the ideas of linear interference.

Before showing the relationship between the LIN and NONLIN terms, the individual distributions of these components of the heat flux are shown for wave-1 (Fig. 4.4). As discussed in Smith and Kushner (2012), the LIN heat flux is weakly negatively skewed

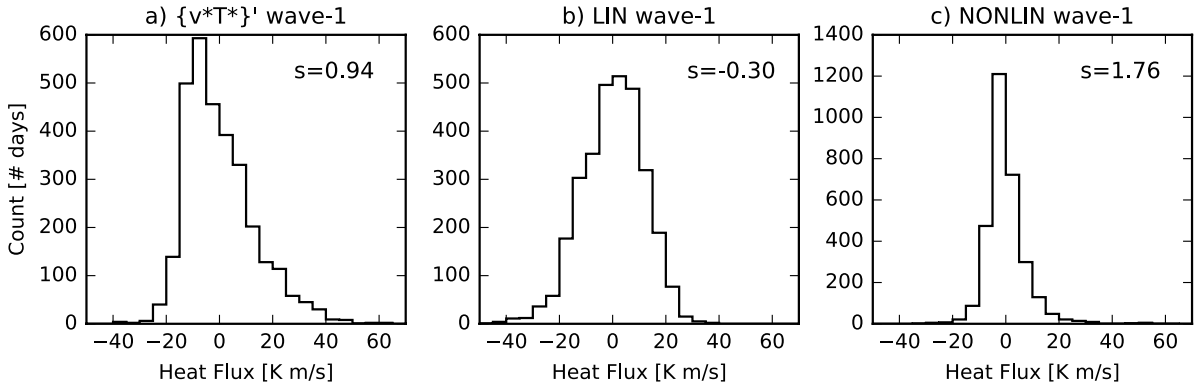

Figure 4.4: Daily histograms over all DJF days of wave-1 a) $\{v^*T^*\}'$, b) LIN and c) NONLIN at 100hPa and 60°N. The skew of each distribution is written in the top-right of each panel.

while the NONLIN heat flux is positively skewed. This is in accordance with the fact that positive and negative heat flux anomaly events tend to be driven more by the NONLIN and LIN terms, respectively (see Fig. 3a-b of Smith and Kushner (2012) and Fig. 3.5). The properties of the wave anomaly parameter distributions that are responsible for skewness of the LIN and NONLIN distributions will be discussed in Section 4.3.3.

4.3.2 LIN and NONLIN relationship

Previous work has suggested a weak negative covariance between the LIN and NONLIN terms in the Northern Hemisphere winter (e.g. see Fig. 2 of Smith and Kushner (2012) and Fig. 3.1). However, these results were based on the total (that is, all wavenumber) LIN and NONLIN fluxes. In this section it is shown that when examined for individual wavenumbers, there is a clear but nonlinear relationship between the LIN and NONLIN terms for wave-1 and wave-2. An argument based on the wave anomaly tilts will be made to explain the relationship, and it will be used to explain the positive skewness of wave-1 and wave-2 heat flux in the Northern Hemisphere.

Figure 4.5 shows 2D histograms of LIN versus $\{v^*T^*\}'$ and LIN versus NONLIN for all wavenumbers, wave-1 and wave-2. Focusing first on the LIN versus NONLIN distributions, note that for when including all wavenumbers (Fig. 4.5d) there is no strong relationship between the variables, although the slight tendency for days to fall in the second quadrant (i.e. negative LIN and positive NONLIN) leads to a weak negative correlation of $r = -0.13$ between the two. However, when the heat fluxes are filtered for just wave-1 (Fig. 4.5e), a nonlinear relationship between the two terms becomes

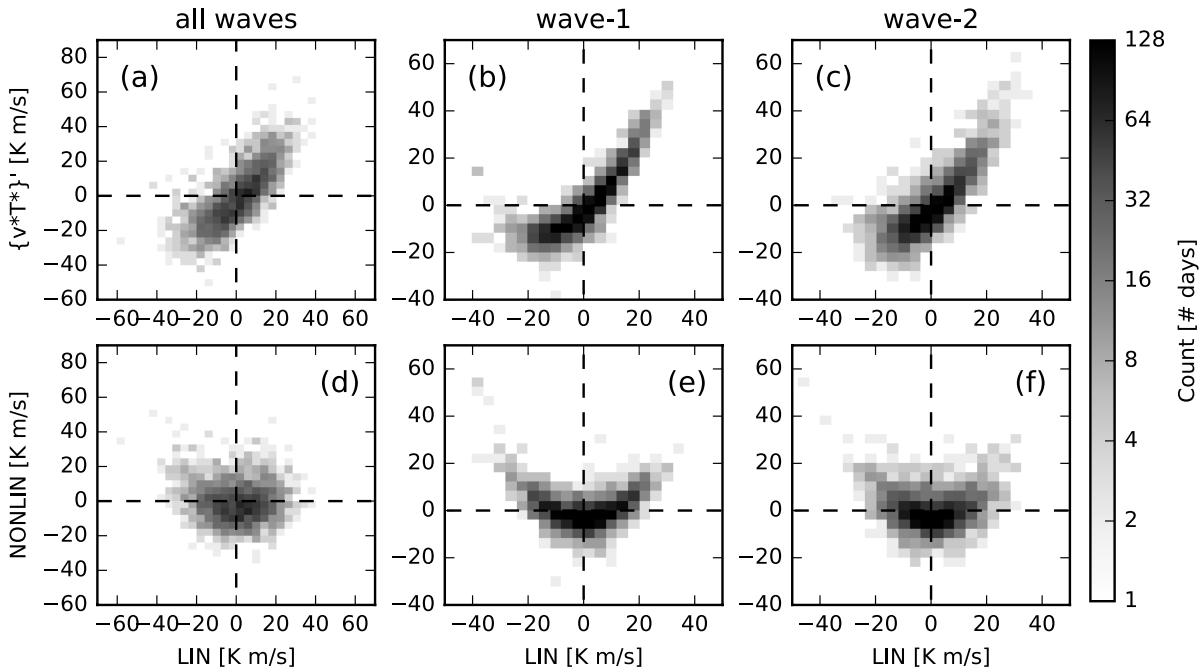

Figure 4.5: 2D histograms of various components of heat flux at 60°N and 100hPa over all DJF days. For (a)-(c), histograms are for LIN versus $\{v^*T^*\}'$ and for (d)-(f) they are for LIN versus NONLIN. From left to right, the three columns are for all wavenumbers, wave-1 and wave-2. The color scale is logarithmic and the same in all plots.

immediately apparent. Essentially, when the LIN term is either negative or positive, the NONLIN term tends to be positive. For wave-2 (Fig. 4.5f) there is a suggestion of a similar relationship, but it is noisier. The dependence between these terms implies that they will tend to cancel each other when LIN is negative and amplify each other when LIN is positive. We will show that this additive effect is a primary reason why the distribution of heat flux is positively skewed. Experiments with the toy statistical model in Section 4.3.4 will show that the negative and positive skews of, respectively, the wave-1 LIN and wave-1 NONLIN terms (recall Fig. 4.4) are not necessary requirements for the positive skewness of the total wave-1 heat flux anomaly.

The association between the LIN and NONLIN terms seen in Figs. 4.5e-f can be understood as follows. Given that the wave-1 and wave-2 components of the Northern Hemisphere stationary wave (i.e. Z_c^*) at 60°N have a westward tilt with height throughout the troposphere and stratosphere, a strongly positive or negative LIN term implies that the wave anomaly will also have a westward tilt with height and be either in phase or out of phase with the climatology (Eq. 4.13). However, since the NONLIN term does not depend on the phase of the wave anomaly, but does depend on the tilt of the wave anomaly (Eq. 4.9), for either the negative or positive LIN case, we expect a positive

NONLIN term. This is precisely what is seen in Figs. 4.5e-f. The relationship between LIN and NONLIN is clearer for wave-1, so we will primarily focus on this wavenumber and delay the discussion of wave-2 until Section 4.3.6.

4.3.3 Observed wave anomaly parameter distributions

In the next section, a statistical model based on the distributions of three parameters of the wave anomaly (amplitude A', phase θ' and tilt $\frac{d\theta'}{d\ln p}$) will be used to understand the distributions of the different components of the heat flux and the relationship between the LIN and NONLIN terms. Before outlining the model results, in this section the observed distributions of the wave anomaly parameters are shown. Furthermore, the relationships between the different parameters are also described. It will be argued that some of the dependencies between wave anomaly parameters are responsible for the skews of the LIN and NONLIN distributions (Figs. 4.4b-c), a fact that will be confirmed with the toy model in the next section.

Figure 4.6 shows the distributions of the observed DJF wave-1 amplitude, phase and tilt at 60°N and 100hPa, as well as the joint distributions between these parameters. Note that for the tilt parameter, the quantity plotted here and in subsequent figures is simply the difference between phases at the levels above and below 100hPa, that is, $\theta(125\text{hPa}) - \theta(70\text{hPa})$. This is used as a proxy for the actual slope in phase, $\frac{d\theta}{d\ln p}$. Figure 4.6 demonstrates a number of important points. First, the wave anomaly amplitudes are not small: more than 62% of days have an anomaly amplitude greater than the amplitude of the climatology (Fig. 4.6a). Second, there are certain phases that wave-1 anomalies more frequently have (note the two peaks separated by about 180° in Fig. 4.6b), and they are roughly in or out of phase with the climatology. This can be attributed to the standing wave-1 at this level and latitude, which typically has antinodes near the longitudes of the maximum and minimum of the wave-1 climatology (recall Fig. 2.6 and Fig. 3.2). Finally, the majority of days have a westward tilted anomaly (i.e. $\frac{d\theta'}{d\ln p} > 0$), although usually the anomaly is not as tilted as the climatology (Fig. 4.6c). This is consistent with the relatively weak baroclinic tilt of wave-1 standing waves at 60°N (e.g. Fig. 3.2).

When constructing distributions of the amplitude, phase and tilt for the statistical model in Section 4.3.4, simplified versions of the observed distributions will be used in order to test which of the features of the observed distributions of these parameters

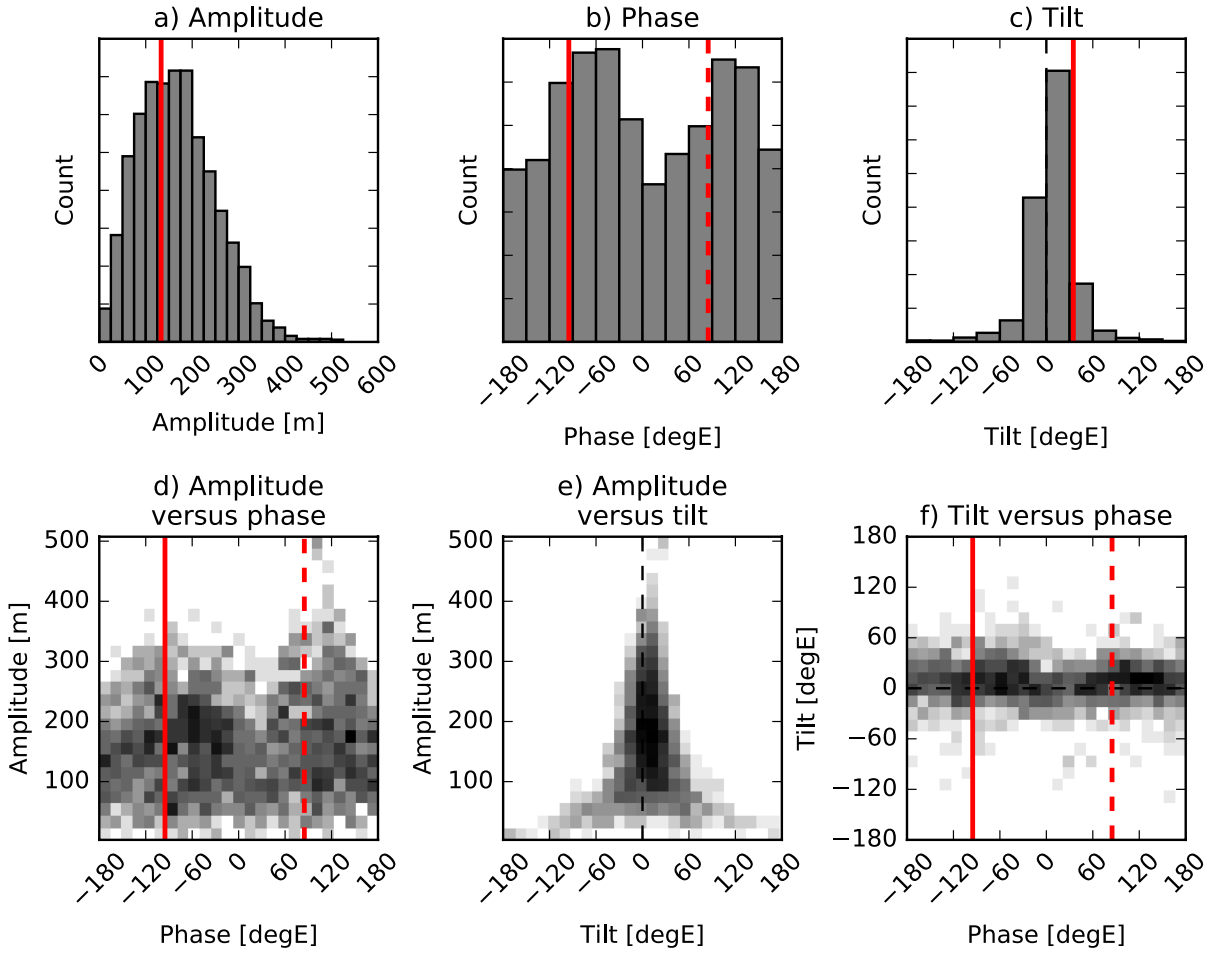

Figure 4.6: a)-c) Histograms of the three parameters of the geopotential height wave-1 anomaly at 60°N and 100hPa for all DJF days. a) The wave amplitudes ($A(p)$ in Eq. 4.1), b) the wave phase ($\theta(p)$ in Eq. 4.1) and c) the wave tilt (phase at 125hPa minus phase at 70hPa). d) - f) 2D histograms of d) amplitude versus phase, e) amplitude versus tilt and f) tilt versus phase. The values of each parameter for the DJF-mean climatological wave are marked by the vertical red lines. The dashed red lines in b), d) and f) mark the phase of the minimum of the climatological wave.

are required to obtain a realistic distribution of the heat flux and its components. For example, a uniform distribution in phase and a symmetric distribution with zero mean in tilt will be used.

The distributions of the three parameters shown in Figs. 4.6a-c are not sufficient to fully describe the distribution of wave-1 anomalies at 60°N and 100hPa. This is because the parameters are not independent of each other. Figures 4.6d-f shows the observed joint distributions for the three possible combinations of parameters. Figure 4.6d suggests that there is a tendency for wave anomalies out of phase with the climatology (that is, with phases of around 100°E) to be of larger amplitude than those that are roughly in phase with the climatology. Although it is not known at this point why that is, it explains the negative skewness of the LIN term (Fig. 4.4b), since out of phase anomalies correspond to negative LIN. It will be confirmed in Section 4.3.4 that if this relationship between phase and amplitude does not exist, then the LIN distribution is symmetric. Figure 4.6e shows that there is also a strong relationship between amplitude and tilt: the larger the anomaly amplitude, the closer to barotropic the wave anomaly tends to be. In addition to this, the largest amplitude waves are more likely to be westward tilted with height than eastward tilted. This latter relationship is responsible for the positive skewness of the NONLIN term. This will be confirmed in the next section by constucting a symmetric tilt distribution and showing that this leads to a symmetric NONLIN distribution. Finally, there is no clear relationship between tilt and phase (Fig. 4.6f).

4.3.4 Toy model results

As described in Section 4.2.2, using hydrostatic and geostrophic balance, the heat fluxes can be calculated using the amplitude, phase and tilt parameters (and the amplitude, phase and tilt of the climatological wave). Three versions of the toy model will be discussed in this section. The first version creates artificial distributions of all three parameter distributions and shows that symmetric LIN and NONLIN distributions can still give rise to a positively skewed $\{v^*T^*\}'$ distribution. The other two versions change only either the phase or the tilt distributions. These are constructed to demonstrate the causes of the non-Gaussianity of the LIN and NONLIN distributions. Importantly, in all cases the toy model generates a relationship between LIN and NONLIN that is qualitatively similar to the observed one (recall Fig. 4.5e) and a positively skewed $\{v^*T^*\}'$ distribution. Table 4.1 summarizes the parameter distributions used for each version of the toy model,

Observed distributions

Hemisphere	Wave-number	Amplitude	Phase	Tilt	$\{v^*T^*\}'$ skew	LIN skew	NONLIN skew
NH	1	Obs	Obs	Obs	0.94 ± 0.11	-0.30 ± 0.10	1.76 ± 0.46
NH	2	Obs	Obs	Obs	1.40 ± 0.22	-0.01 ± 0.14	1.61 ± 0.27
SH	1	Obs	Obs	Obs	0.79 ± 0.11	-0.20 ± 0.16	0.84 ± 0.22
SH	2	Obs	Obs	Obs	0.75 ± 0.16	-0.20 ± 0.19	0.93 ± 0.18

Modeled distributions

Model Number	Wave-number	Amplitude	Phase	Tilt	$\{v^*T^*\}'$ skew	LIN skew	NONLIN skew
1	1	Log normal	Uniform	Symm.	1.03 ± 0.16	0.02 ± 0.04	0.03 ± 0.25
2	1	Obs	Uniform	Obs	1.64 ± 0.09	0.02 ± 0.03	1.88 ± 0.12
3	1	Obs	Obs	Symm.	0.41 ± 0.08	-0.18 ± 0.03	0.00 ± 0.19

Table 4.1: Summary of skewness of heat flux distributions for observations and for three versions of the toy model. NH corresponds to 60°N and 100hPa during DJF, and SH corresponds to 60°S and 100hPa during SON (SH heat fluxes are multiplied by -1). For model number 1, artificial distributions are generated for all three parameters. For model number 2, the amplitude and tilts are chosen from the observed distributions, but the phase is chosen from a uniform distribution. For model number 3, the amplitude and phase are chosen from the observed distributions, while the tilt is forced to have a symmetric distribution. See text for details. In all cases, uncertainties are given as 95% confidence intervals and are computed by bootstrapping: the heat flux distributions are resampled with replacement 10,000 times and the uncertainty provided is twice the standard deviation across this distribution of skews.

and the skews of the LIN, NONLIN and $\{v^*T^*\}'$ distributions for observations and for the models. The details of the construction of the parameter distributions are described below.

Figure 4.7 shows the distributions and joint distributions for the amplitude, phase and tilt used in the toy model number 1. The amplitude distribution is a log-normal distribution with a location parameter $\mu = 4.85$ and a scale parameter $\sigma = 0.42$. The phase distribution is uniform with limits of -180° and 180°. The tilt distribution is constructed to have a similar relationship between amplitude and tilt as that found in observations. That is, there should be a larger spread in tilt for smaller amplitudes (Fig. 4.6e). This is done as follows: once the amplitude distribution is constructed, for each value of amplitude A, a corresponding tilt is selected from a normal distribution with a mean of zero and a standard deviation of $200/\sqrt{A}$. This causes the tilt to have a greater spread at lower amplitudes (see Fig. 4.7e). The ensemble size of each of the parameter distributions is $N = 50,000$.

Given the parameter distributions described above and shown in Fig. 4.7, and using the assumptions of hydrostatic and geostrophic balance, the heat flux and LIN and NONLIN terms are computed. The observed relationship between wave-1 LIN and NONLIN

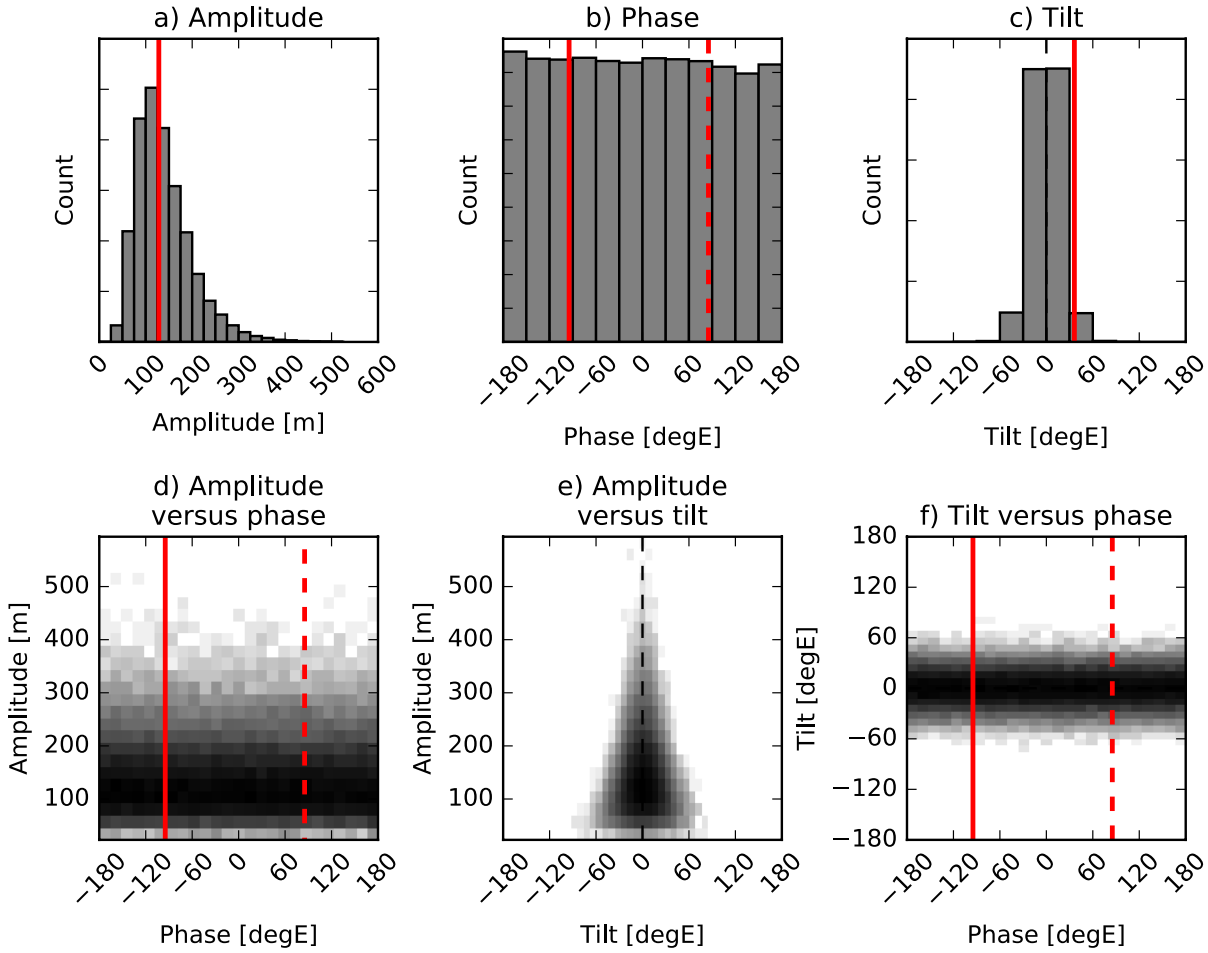

Figure 4.7: a)-c) Histograms of the three parameters of the geopotential height wave-1 anomaly for the toy model number 1. a) The wave amplitudes ($A(p)$ in Eq. 4.1), b) the wave phase ($\theta(p)$ in Eq. 4.1) and c) the wave tilt (phase at 125hPa minus phase at 70hPa). d) - f) 2D histograms of d) amplitude versus phase, e) amplitude versus tilt and f) tilt versus phase. The values of each parameter for the climatological wave are marked by the vertical red lines. The dashed red lines in b), d) and f) mark the phase of the minimum of the climatological wave.

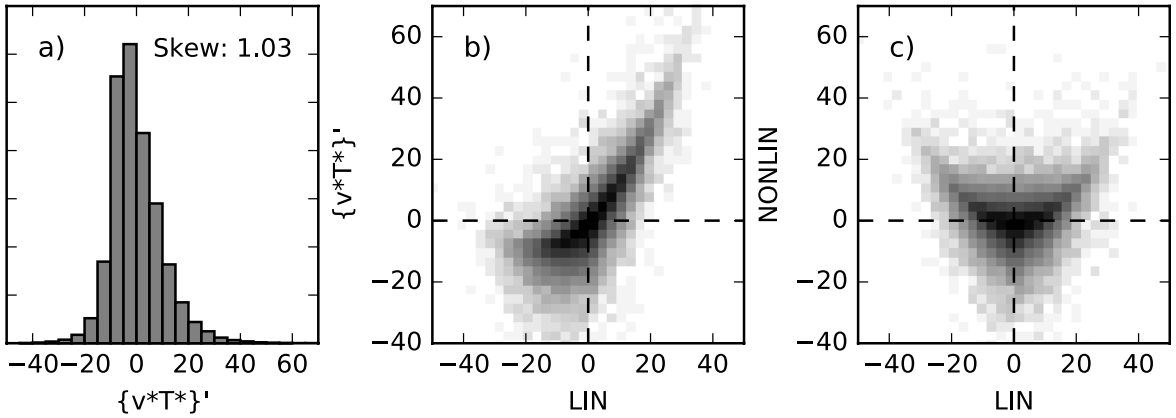

Figure 4.8: For toy model number 1 (see Table 4.1), a) histogram of $\{v^*T^*\}'$, b) 2D histogram of LIN versus $\{v^*T^*\}'$ and (b) LIN versus NONLIN as computed from the toy model. The color scale is logarithmic in b) and c).

is qualitatively reproduced by the toy model (compare Fig. 4.8c to Fig. 4.5e). The skew of the heat flux anomaly distribution for the toy model is 1.03 ± 0.16 (see Fig. 4.8a), similar to the observed skewness of wintertime wave-1 heat flux of 0.94 ± 0.11. Importantly, the toy model is capable of reproducing the observed relationship between LIN and NONLIN, and the positive skewness of the total heat flux anomaly, despite the fact that the parameter distributions have been simplified in comparison to the observed distributions. In particular, it is apparent that the bimodal structure of the observed phase distribution (Fig. 4.6b; indicating that wave-1 anomalies tend to constructively or destructively interfere with the stationary wave) and non-zero mean of the observed tilt distribution (Fig. 4.6c; indicating the preference for upward propagating wave anomalies) are not necessary to recover the skewness of the total heat flux distribution.

Despite the fact that the total heat flux anomaly's positive skewness is well-represented by the model, its LIN and NONLIN distributions have skews that are not significantly different from zero. This is different from the observed LIN and NONLIN distributions which are negatively and positively skewed, respectively. We claim that this difference arises from the fact that the toy model 1) has no dependence between amplitude and phase, and 2) has a symmetric tilt distribution in which the dependence of amplitude on tilt is the same for positive and negative tilts. In order to show this, two additional versions of the parameter distributions are constructed (model numbers 2 and 3 in Table 4.1). Model number 2 samples from the observed distributions of amplitude and tilt, but uses an independent uniform distribution for phase. It results in a LIN distribution that is not significantly different from zero. This explicitly demonstrates point 1 from above: the skewness of LIN is due to the observed relationship between phase and am-

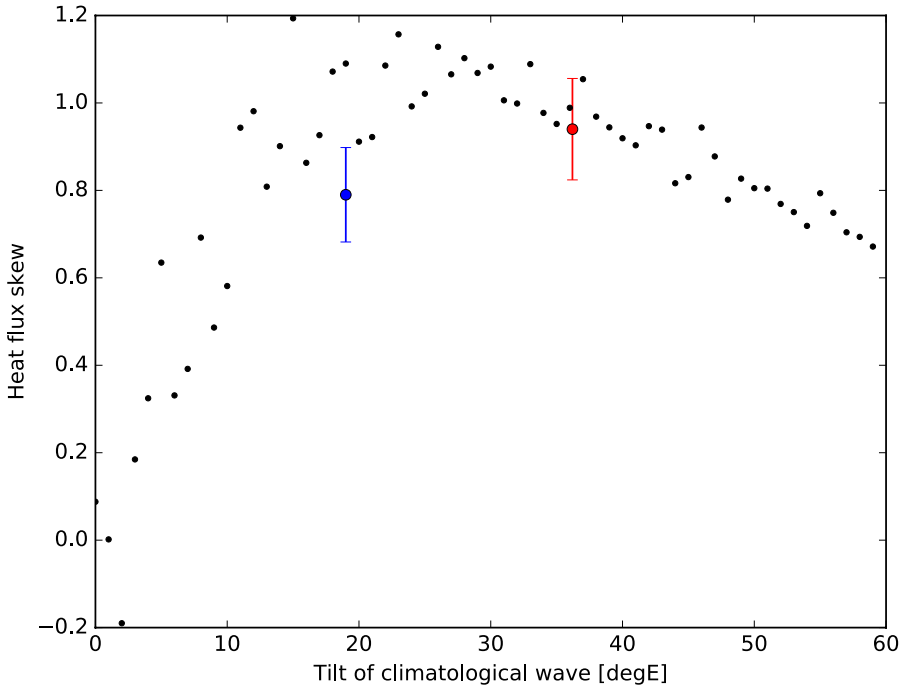

Figure 4.9: The heat flux anomaly distribution's skew for the toy model as computed with varying tilts in the climatological wave (black points). For all the toy model runs, the anomaly parameter distributions are constructed as for model number 1 (see Table 4.1) and 50,000 member ensembles are created for each point. The red and blue points mark the observed heat flux skews and climatological wave tilts in the Northern Hemisphere (at 60°N and 100hPa, for DJF) and Southern Hemisphere (at 60°S and 100hPa, for SON) respectively. Error bars represent 95% confidence intervals calculated using a bootstrap approach (see Table 4.1). The Southern Hemisphere heat flux is multiplied by −1.

plitude. Model number 3 samples from the observed amplitude and phase distributions, but forces the tilt distribution to be symmetric about zero. This is implemented as follows: for each amplitude and phase selected from the observed distributions, two sets of parameters are generated: one with the observed tilt for that day, and one with the negative of the observed tilt. This preserves the main relationship between amplitude and tilt (i.e. lower magnitude of tilt for larger amplitude) but forces the tilt distribution to be symmetric. For this set of anomaly parameters (i.e. model number 3) the NONLIN distribution has near zero skew, confirming point 2 from above.

4.3.5 Skew dependence on stationary wave tilt

It was claimed in the introduction that the westward tilt of the stationary wave is the essential property that leads to the positive skewness of the upward wave activity flux

distribution. Here we will explicitly show this and explore in more detail the dependence of the heat flux distribution skew on the stationary wave tilt. To begin with, its importance can be seen from Eq. 4.13: since $\frac{d\theta_c}{d\ln p} > 0$ for a westward tilted climatology, this means that the most extreme positive or negative LIN days will tend to also have a westward tilted anomaly ($\frac{d\theta'}{d\ln p} > 0$) either in or out of phase with the climatology. The westward tilted anomaly means the NONLIN term will be positive. In turn, this relationship means that the LIN and NONLIN terms will tend to cancel when LIN is negative, but amplify each other when LIN is positive, and thus leads to a positively skewed heat flux distribution. In this section, this idea is tested by systematically changing the tilt of the climatological wave that is prescribed for the toy model. Figure 4.9 shows the heat flux anomaly skew as computed by the toy model for a range of climatological wave tilts from equivalent barotropic (no tilt) to a 60° difference in phase between levels above and below 100hPa. For all the toy model runs, the anomaly parameter distributions are constructed as for model number 1 in Table 4.1: that is, with a uniform phase distribution and with a symmetric tilt distribution centred at zero.

Figure 4.9 shows that the skew of the heat flux anomaly distribution has a strong dependence on the climatological wave tilt. In particular, it confirms that as the tilt goes to zero, the skewness also goes to zero. However, it also shows that the relationship between tilt and skew is non-monotonic: below about 20°, the skew quickly increases as a function of tilt, but for greater tilts the skew slowly decreases. The observed tilt and skew are shown on Fig. 4.9 for both the Northern Hemisphere during DJF and the Southern Hemisphere during SON. The wave-1 climatological wave is much less tilted in the Southern Hemisphere compared to the Northern Hemisphere. The skew is also somewhat smaller for the heat flux distribution in the Southern Hemisphere. However, the two observed tilts roughly span the part of the modelled heat flux skew / tilt relationship that is approximately flat (i.e. they are on either side of the tilt that corresponds to the maximum possible heat flux skew). Thus, we cannot confidently say that the difference in heat flux skew between the two hemispheres is due to the differences in stationary wave tilt. The Southern Hemisphere's heat flux distribution will be further discussed in the next section.

To confirm that the westward tilt of the climatological wave is responsible for the observed relationship between LIN and NONLIN, Fig. 4.10 plots 2D histograms between the two terms for three versions of the toy model. The first is the same as model number 1 described above, and it prescribes the observed climatological tilt of 38.2° (i.e. Fig. 4.10a

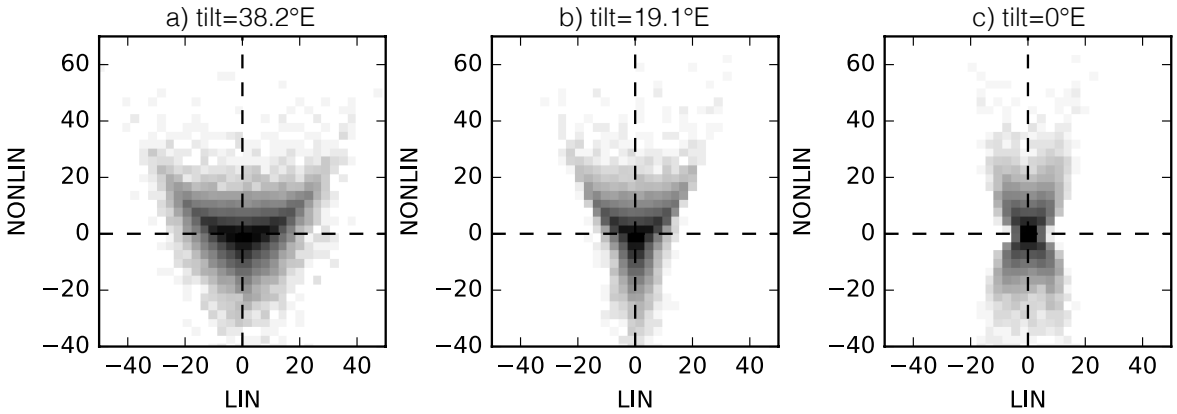

Figure 4.10: 2D histograms of LIN versus NONLIN as computed with the toy model with a climatological tilt of a) 38.2°E (the observed wave-1 tilt at 60°N and 100hPa for DJF), b) 19.1°E and c) 0°E.

is just reproducing Fig. 4.8c). The next version (Fig. 4.10b) prescribes half of the observed the tilt while the last (Fig. 4.10c) sets the climatological wave to be barotropic. Figure 4.10 shows that, qualitatively, the toy model with the observed climatological tilt has the LIN/NONLIN distribution that looks most like the observed relationship. Furthermore, it confirms that when the climatological wave is equivalent barotropic (i.e. $\frac{d\theta_c}{d\ln p} = 0$) there is no well-defined relationship between the LIN and NONLIN terms (except that when the NONLIN term is close to zero, the LIN term tends to be close to zero as well).

4.3.6 Additional results

Wave-2 heat flux distribution

The observed wave-2 DJF $\{v^*T^*\}'$ distribution at 60°N and 100hPa has a similar variance to the wave-1 distribution (compare Figs. 4.3c and 4.3d) and a somewhat larger positive skewness. Differently than for wave-1, the wave-2 LIN distribution has a skew that is not significantly different than zero, while the NONLIN wave-2 skew of 1.61 is not significantly different than the wave-1 NONLIN skew (see Table 4.1). In this section, we briefly analyze the wave-2 heat flux distributions.

It was argued in Section 4.3.4 that the cause of the negative skewness of the wave-1 LIN term was the tendency for anomalies out of phase with the climatology to be of larger amplitude than in phase anomalies. Since the observed wave-2 LIN distribution has a skew of nearly zero, this is a useful test case for that argument. Figure 4.11 shows

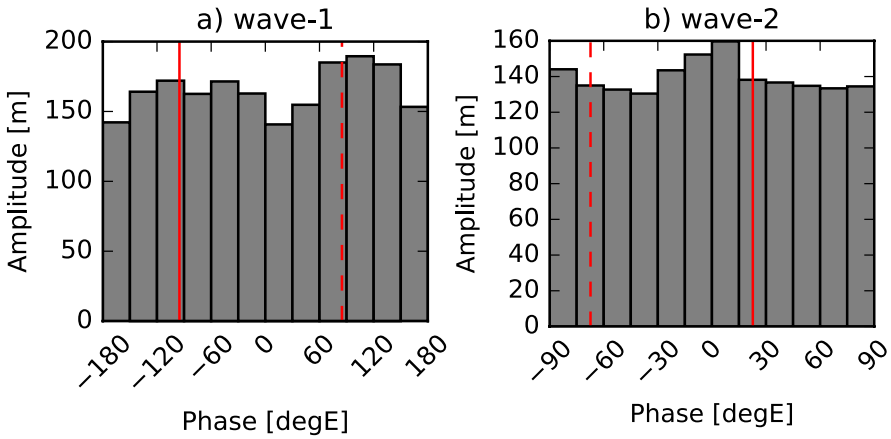

Figure 4.11: The average anomaly amplitude when the anomaly phase is within a given bin. Computed for a) wave-1 and b) wave-2 at 60°N and 100hPa, for all DJF days.

the average amplitude of observed wave anomalies as a function of their phase, for both wave-1 and wave-2. As was hinted at by Fig. 4.6d, wave-1 anomalies that are out of phase with the climatology tend to be of slightly higher amplitude than those that are in phase with the climatology (Fig. 4.11a). On the other hand, wave-2 anomaly amplitudes do not have a clear systematic dependence on phase (Fig. 4.11b). Given that wave-1 LIN has a negative skew but wave-2 LIN does not, this supports the argument that the skewness of the LIN term is determined by the relationship between wave anomaly amplitude and phase.

Southern Hemisphere

The Southern Hemisphere's polar vortex is known to be substantially less variable than the Northern Hemisphere's (e.g. Yoden et al., 2002) and only one sudden stratospheric warming has been observed to occur in the Southern Hemisphere (Newman and Nash, 2005). Nevertheless, it still has a substantial amount of upward wave activity flux variability, of which the majority is attributable to the LIN term during SON (Fig. 9 of Smith and Kushner (2012)). Furthermore, the climatological wave-1 in the Southern Hemisphere's lower stratosphere actually has a larger amplitude than the corresponding Northern Hemisphere stationary component: its amplitude is 203m at 60°S and 100hPa, averaged over SON, compared to 133m at 60°N and 100hPa averaged over DJF. Furthermore, the distribution of wave-1 heat flux at 60°S and 100hPa over all SON days has a skew of 0.79 ± 0.11 (Table 4.1). Overall, the wave-1 heat flux distribution in the Southern Hemisphere is similar to the Northern Hemisphere's distribution, the most sig-

nificant difference being that the NONLIN part has a skew of only 0.84 ± 0.22 compared to 1.76 ± 0.46 in the Northern Hemisphere.

The wave-2 heat flux distribution in the Southern Hemisphere also has a positive skew (with a value of 0.75 ± 0.16) but it is for a different reason than the cases discussed up until now. This is because the wave-2 stationary wave in the Southern Hemisphere has an amplitude of only 25m, compared to 157m in the Northern Hemisphere, and is nearly barotropic in the lower stratosphere. Because of the climatology's small amplitude, the NONLIN term explains nearly all of the variance of the wave-2 heat flux in the Southern Hemisphere (the correlation between the two is $r = 0.96$). Thus, the wave-2 heat flux distribution is essentially the same as the wave-2 NONLIN distribution, and the positive skewness can be attributed directly to the skewness of the NONLIN distribution, which is present because of the tendency of westward tilted wave anomalies to be of larger amplitude (see discussion in Section 4.3.4). This is distinct from the Northern Hemisphere wave-1 and wave-2, and Southern Hemisphere wave-1 distributions, where the westward tilt of the climatological wave is the most important contribution to the positive skewness of the total heat flux distribution.

4.4 Conclusions

This chapter investigated why the upward wave activity flux and the temperature distributions in the polar stratosphere are positively skewed. The motivation for doing so was to understand the distribution of temperatures in the stratosphere, which is essential for ozone chemistry and loss. The typical explanation for the positive skewness of temperature is that there is a lower bound on temperatures set by a radiative limit, while dynamical wave-driving can force large positive anomalies of temperature. Here, it was shown that the heat flux distributions themselves are positively skewed, and it was suggested that this may be at least partially a cause for the positive skewness of temperatures. The primary focus was on wave-1 heat flux at 60°N and 100hPa, during boreal winter.

The ideas of linear interference were used in order to understand the causes of the positive skewness of the heat flux distributions. First, expressions were derived for the LIN and NONLIN terms as a function of the wave anomaly amplitude, phase and tilt, as well as the climatology's amplitude, phase and tilt. It was shown that when the

heat fluxes are filtered by wavenumber, the LIN and NONLIN terms have a well-defined relationship. This can be understood as follows: because the climatological wave has a westward tilt with height, the largest positive and negative LIN days will occur when the anomalous wave also has a westward tilt with height and is either in or out of phase with the climatology. This means that the NONLIN term will tend to be positive and large when the LIN term is either negative or positive, leading to the observed relationship between the two terms. Because the total heat flux anomaly is equal to the sum of the LIN and NONLIN terms, this means that when the LIN term is negative, it will tend to cancel the NONLIN term, but when it is positive it will amplify the NONLIN term, leading to the positive skewness of the heat flux.

To confirm this argument, a simple toy model was constructed that computes the heat flux distribution given prescribed distributions for the wave anomaly amplitudes, tilts and phases, as well as values for the climatological wave amplitude, tilt and phase. By using this model we showed that 1) the skew of the LIN term is due to out of phase wave anomalies tending to be of larger amplitude, 2) the skew of the NONLIN term is due to the largest amplitude anomalies tending to be westward tilted, and 3) one can obtain a positively skewed total heat flux distribution without having a skewed LIN or NONLIN distribution, just because of the above-described relationship between the two terms. Furthermore, by using the toy model with a large range of prescribed climatological wave tilts, we explicitly showed that the heat flux skew has a strong dependence on the climatological tilt, and that it goes to zero when the climatological wave becomes barotropic.

Finally, the distributions of the wave-2 heat flux and Southern Hemisphere wave-1 and wave-2 heat fluxes were investigated. It was shown that Northern Hemisphere wave-2 and Southern Hemisphere wave-1 generally behave similarly to the wave-1 Northern Hemisphere distribution. That is, the westward tilted climatological wave causes the quadratic relationship between the NONLIN and LIN terms, which leads to the positively skewed total heat flux anomaly. On the other hand, for wave-2 in the Southern Hemisphere, the climatological wave is very weak and roughly barotropic. This means that the heat flux distribution there is nearly entirely driven by the NONLIN term. Thus, the positive skewness of the wave-2 heat flux in the Southern Hemisphere is caused by the relationship between tilt and amplitude that causes the asymmetry in the NONLIN term.

In summary, this chapter explains the positive skewness of the upward wave activity

flux by appealing to linear interference effects. Future work will aim to understand in more detail the connection between the upward wave activity flux distribution in the lower stratosphere and the temperature (or polar vortex strength) distribution in the mid-stratosphere. It is known that there is a strong correlation between time-integrated heat flux at 100hPa and polar vortex strength and temperature in the mid-stratosphere (Newman et al., 2001; Polvani and Waugh, 2004). However, the implications of this for the skewness of the temperature distribution are unclear. In particular, will a positively skewed upward wave activity flux distribution necessarily drive a positively skewed temperature distribution, and is it possible to have a positively skewed temperature distribution without a positively skewed upward wave activity flux distribution? Future work will address these questions by constructing a stochastic model of the relationship between temperature and upward wave activity flux, and driving it with various distributions of upward wave activity flux.

Chapter 5

Standing and travelling waves in the troposphere and cold North American winter weather

5.1 Introduction

The winter of 2013/14 over eastern North America featured persistent cold weather throughout the winter season and an extreme cold air outbreak that brought record low temperatures to many cities and regions on 7 January 2014 (Screen et al., 2015; Davies, 2015). This season and the subsequent 2014/15 winter became popularized in the media as being linked to a strongly distorted "Polar Vortex" (see Waugh et al., 2016, and references within) which manifested itself as a large amplitude west-to-east ridge-trough feature in the mid-tropospheric flow over North America, enhancing northerly advection and cold temperatures over central and eastern North America (see Figs. 5.1 and 5.2). It is a challenge to determine whether to attribute such circulation and temperature extremes to spontaneous internal atmospheric variability, internally or externally driven variability at the ocean and land surface, or other anthropogenic and natural forcings. For the recent winters, these extremes have been attributed, for example, to anomalous Pacific sea surface temperatures (Wang et al., 2014, 2015; Hartmann, 2015) and to impacts on the mid-latitudes from Arctic amplification associated with global warming and sea ice loss (Francis and Vavrus, 2012; Cohen et al., 2014; Kug et al., 2015; Lee et al., 2015). However, such events become more rare as a result of sea ice loss and

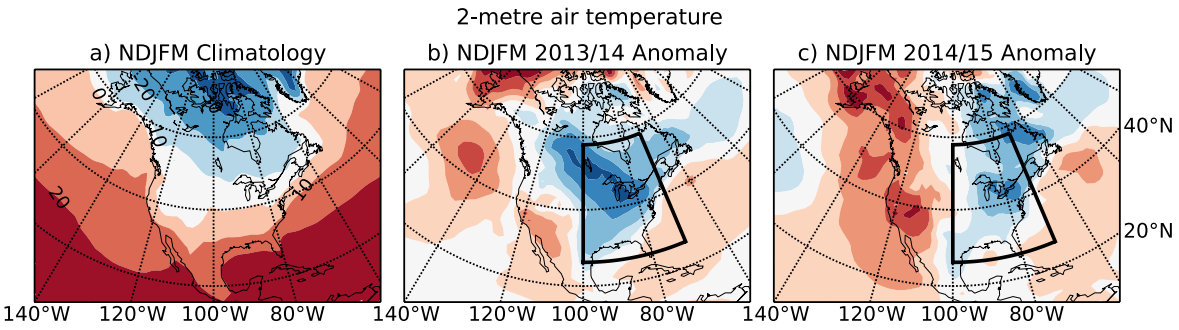

Figure 5.1: a) The climatological 2-metre air temperature averaged between November 1 and March 31. Contour intervals are 10°C. The anomalous 2-metre air temperature averaged between b) 1 November 2013 and 31 March 2014, and c) 1 November 2014 and 31 March 2015. Contours are at ±0.5°C, ±1.5°C, etc. in b) and c). The black lines in b) and c) outline the area taken for the CENA temperature average (see Section 5.2).

global warming in current climate model projections (Screen et al., 2015; Wolter et al., 2015), suggesting considerable uncertainty about the ultimate drivers of these events.

One challenge is that apparently similar climate extremes, such as the recent cold winters, might feature distinctive dynamics. For example, we will see in this chapter that the winters of 2013/14 and 2014/15 both featured extreme cold weather in eastern North America, but that the spatial and temporal character of the circulation in the two winters suggest distinctive atmospheric dynamical origins. To more precisely and robustly characterize the drivers of such events, and to put them in the context of longer-term climate variability, this chapter will examine subseasonal (1-100 day) variability in the mid-tropospheric flow and its connection to eastern North American temperatures. The spectral decomposition developed in Chapter 2 will be used to cleanly separate quasi-stationary standing waves from travelling synoptic weather systems across the Northern Hemisphere and to identify different drivers for each of these phenomena. The large-scale horizontal structures of the dominant standing and eastward travelling components will be shown. We will then focus on the ridge-trough mid-tropospheric flow over North America and its link to cold weather extremes at the surface.

This effort to separate flow variability with distinctive spatio-temporal characteristics and to bridge to the longer-term climate record work builds on other recent work in the synoptic variability literature (e.g. Davies, 2015). Here we focus on the North American cold extremes, with a particular examination of the winters of 2013/14 and 2014/15. We will separate the 500hPa geopotential height field into standing (i.e. quasi-stationary) and travelling waves to see how these waves are linked to surface temperature extremes. As justified below, we refer to the standing and eastward travelling components

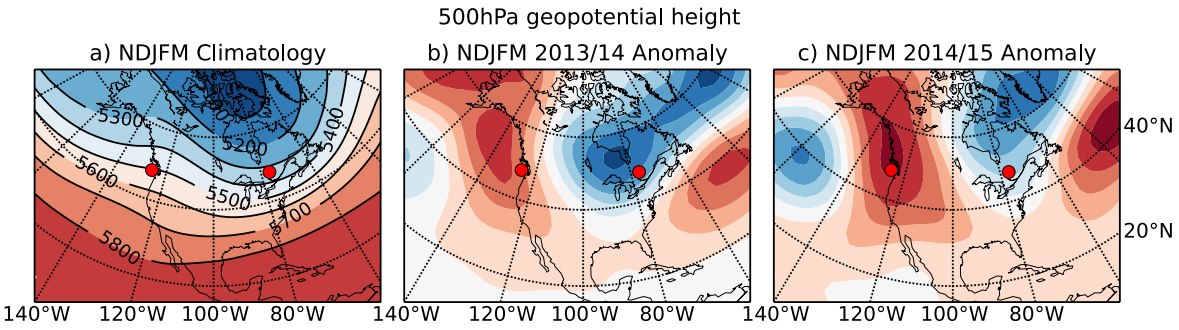

Figure 5.2: a) The climatological Z500 averaged between November 1 and March 31. Contour intervals are 100m. The anomalous (deviation from the climatology) Z500 averaged between b) 1 November 2013 and 31 March 2014, and c) 1 November 2014 and 31 March 2015. Contours are at ±10m, ±30m, etc. in b) and c). The red circles indicate the nodes of the DCI (see Section 5.2).

as, respectively, the slow and fast parts of the mid-latitude circulation variability.

5.2 Data and methods

Daily 2-metre air temperature and geopotential height at 500hPa (Z500) for 1958-2015 boreal winters (November 1 - March 31) from the NCEP-NCAR Reanalysis 1 are used (Kalnay et al., 1996). In this chapter the NCEP-NCAR Reanalysis is used instead of the previously used ERA-Interim Reanalysis in order to have a longer data record and thus be able to examine longer-term climatic variability. There is generally close agreement between the reanalyses during the overlap period in the Northern Hemisphere troposphere, and the analysis has been reproduced with the ERA-Interim Reanalysis with very similar results (not shown). Following the notation of previous chapters, geopotential height with its zonal mean removed is denoted Z*.

The decomposition of Z500 into standing, westward travelling and eastward travelling components for each winter season is performed according to the method described in Chapter 2. However, note that in Chapter 2, our aim was to look solely at the subseasonal variability and for this reason the climatological seasonal cycle and time-mean of each winter season was removed before applying the spectral analysis. On the other hand, in this chapter, we seek to better understand the evolution of the quasi-stationary flow across the season and so we apply the analysis to the total geopotential height including the time evolving climatological mean flow and the time-mean of each winter season, with only the zonal mean removed. In this chapter, we will refer to the sum of the stationary (i.e. time mean) and standing waves as the "standing" part. The travelling part, by

contrast, includes no time mean component.

As discussed in Section 5.1, later in this chapter the drivers of cold winter weather over eastern North America will be examined. Two quantities are defined here in order to make the connection between the large-scale circulation and cold surface conditions explicit. First, central eastern North America (CENA) temperature is defined as the area-weighted mean 2-metre air temperature of all land-occupied grid cells within 70-100°W and 26-58°N, as in Screen et al. (2015). Second, the dipole circulation index (DCI) is defined as the difference in Z500 between (47.5°N, 125°W) and (47.5°N, 77.5°W). When it is positive, this index represents a ridge over western North America and a trough over eastern North America. This index is constructed to directly link mid-tropospheric flow over North America with CENA temperatures. The positions of the dipole were thus deliberately chosen to maximize the absolute value of the Pearson correlation between the deseasonalized dipole circulation index and the deseasonalized CENA 2-metre temperature over all winter days, with the constraint that both nodes of the dipole be at the same latitude. This correlation is -0.61 ($p < 0.01$). The Pearson correlation between the winter-averaged dipole circulation index and winter-averaged CENA 2-metre temperature is -0.63 ($p < 0.01$). A similar dipole index was defined by Wang et al. (2014) in an attempt to explain the cause of winter-mean ridge over western North America during the 2013/14 winter. The authors found that the occurrence of such an atmospheric regime was related to a pattern of sea surface temperature anomalies that typically precede El Niño events. The index defined here is similar, but our focus is on understanding the sub-seasonal to seasonal variability of the dipole instead of the drivers of the seasonal-mean anomalies as in Wang et al. (2014). Finally, given the decomposition of the Z500 field into its standing and travelling components, note that it is straightforward to also separate the dipole circulation index into contributions from each of these terms.

5.3 Results

5.3.1 Standing and travelling waves in the extratropical troposphere

In Chapter 2, the spectral properties of Northern Hemisphere winter geopotential height anomalies were studied. Although the focus there was on the planetary waves involved in stratosphere-troposphere coupling, Fig. 2.5 demonstrated that in the troposphere there

are strong standing wave signals across the mid-latitudes, particularly for planetary length scales (wave-1 to wave-3). For wave-1, and to a lesser extent wave-2, there is also a significant westward travelling signal between roughly 60°N and 80°N. Finally, the shorter length scales (wave-5 and greater) are dominated by eastward travelling variability between 30°N and 60°N. In this section, we will describe in more detail the standing and travelling characteristics of mid-tropospheric variability, and show the connection of standing wave variability to classic teleconnection patterns (e.g. Wallace and Gutzler, 1981).

Figure 5.3 shows the variance over all winter days of the different components of Z500 as a function of longitude and latitude. This is the same metric as to what was shown in Fig. 2.6, except that here it is computed for all wavenumbers instead of just one wavenumber at a time. There are distinct longitudinal maxima in the variance of total Z500 in the North Pacific and North Atlantic regions (Fig. 5.3a), the contributions to which are dominated by the standing Z500 variance (Fig. 5.3b). The westward travelling and eastward travelling components of Z500 make smaller contributions to the total variance, but have very different spatial patterns than the standing variance. As expected from Fig. 2.5, the westward travelling variance peaks between 60°N and 80°N. It is also quite zonally symmetric, which is expected because the westward travelling component is largely dominated by wave-1.[1] Finally, the eastward travelling variance peaks at lower latitudes, with a maximum around 45°N, and has a highly non-uniform zonal structure, with maxima in the North Pacific and North Atlantic storm track regions (Blackmon, 1976; Lau and Wallace, 1979).

The differing spatial structures of the standing and eastward travelling wave variance in the troposphere are suggestive of distinct drivers for each of these components of the variability. To further explore this, one-point correlation maps of the total, standing, westward travelling and eastward travelling waves are computed. In this type of calculation, a base point is chosen and then the correlation of the given field at all other longitudes and latitudes with the value of that same field at the base point is computed (e.g. Wallace and Gutzler, 1981). Here, two particular base points are selected in order to emphasize the differences between the typical structures of the standing wavefield versus the eastward travelling wavefield. The first point is the maximum in the standing wave variance in the North Pacific (45°N, 165°W; see Fig. 5.3b) while the second point is the maximum in the eastward travelling variance in the North Atlantic storm track

[1]The time-variance of a single wavenumber travelling wave is exactly zonally symmetric (Eq. 2.11).

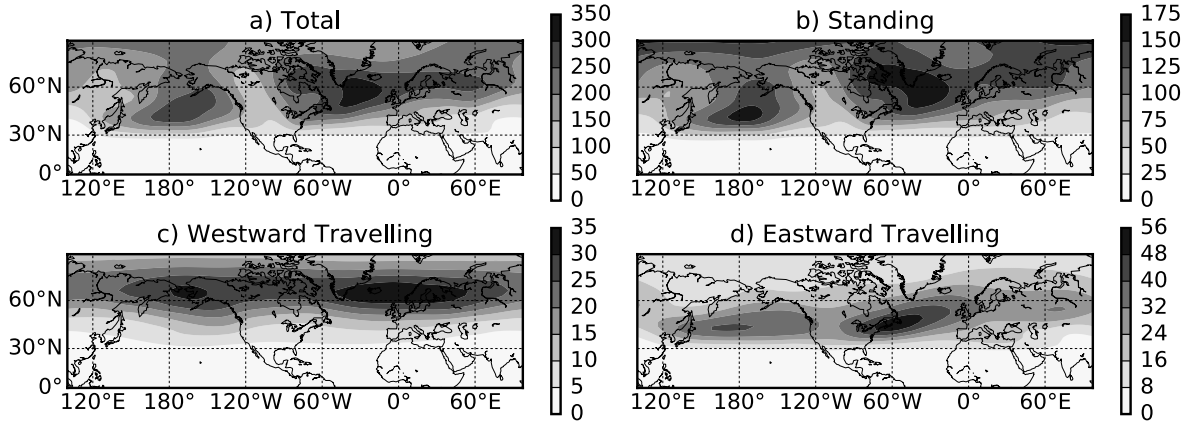

Figure 5.3: The variance over all winter days of a) the total, b) the standing, c) the westward travelling and d) the eastward travelling Z500. Units are $100\,\mathrm{m}^2$, and note the different contour intervals for each panel. Panels b) through d) do not add up to panel a) because there are positive covariances between the standing and travelling waves which are not shown.

(35°N, 50°W; see Fig. 5.3d). The correlations of Z500 at all points with Z500 at the respective base point, as well as this quantity for the various subcomponents of Z500, are shown in Fig. 5.4. This is similar to the metric computed by Wallace and Gutzler (1981), except that they only used the total Z500 and were computing correlations based on monthly data instead of daily data. Figure 5.4 reveals a stark contrast between the correlation structure of the standing and eastward travelling waves. For the standing Z500 with a base point in the North Pacific, the correlation structure has the form of the Pacific/North America pattern (c.f. Fig. 16b of Wallace and Gutzler (1981)). On the other hand, for the eastward travelling Z500 centred in the North Atlantic storm track, the correlation structure has a clear zonal wave train pattern with alternating positive and negative correlations extending east and west. Figure 5.4 also shows that the total Z500 correlation structure is dominated by the standing component (note the similarity between the first two rows of Fig. 5.4), but is still a conflation of both the standing variability and eastward travelling synoptic variability. For example, focusing on the North Pacific base point (left column of Fig. 5.4), the standing correlations show a stronger Pacific/North America pattern compared to the correlations computed with the total field. Wallace and Gutzler (1981) removed the influence of synoptic variability by using monthly averaged data, but here, by using the standing-travelling wave decomposition, we are able to do so without imposing an explicit time scale separation. The differing correlation patterns of the standing and eastward travelling waves will be kept in mind in the next section when interpreting the drivers of the dipole circulation index.

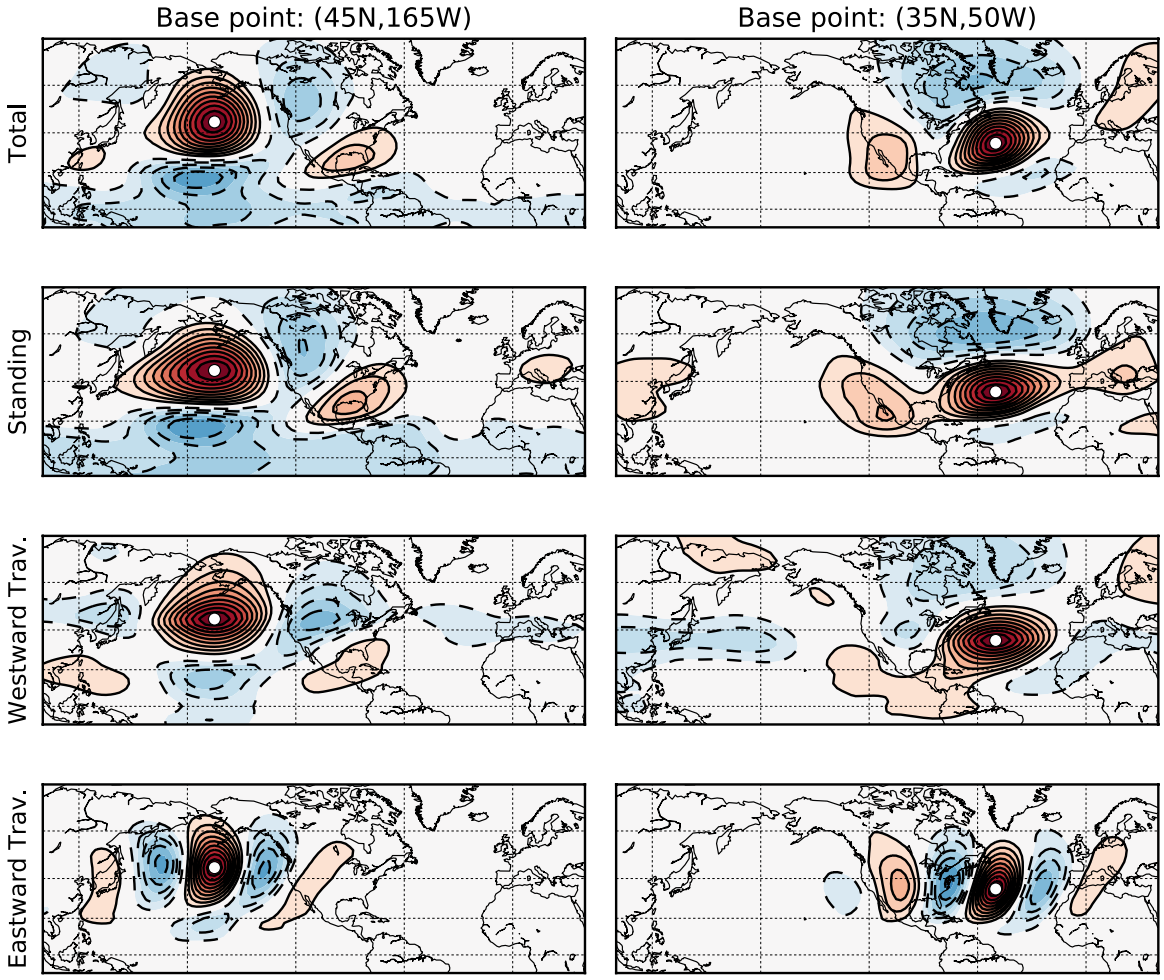

Figure 5.4: One-point correlations of various components of the Z500 field. The left column shows correlations computed with a basepoint at 45°N and 165°W, while the right column is for a basepoint at 35°N and 50°W. The basepoints are marked by white circles. The four rows are, from top to bottom, correlations computed with the total, standing, westward travelling and eastward travelling Z500 fields. The contour intervals are $\pm 0.1, \pm 0.2, \pm 0.3$, etc.

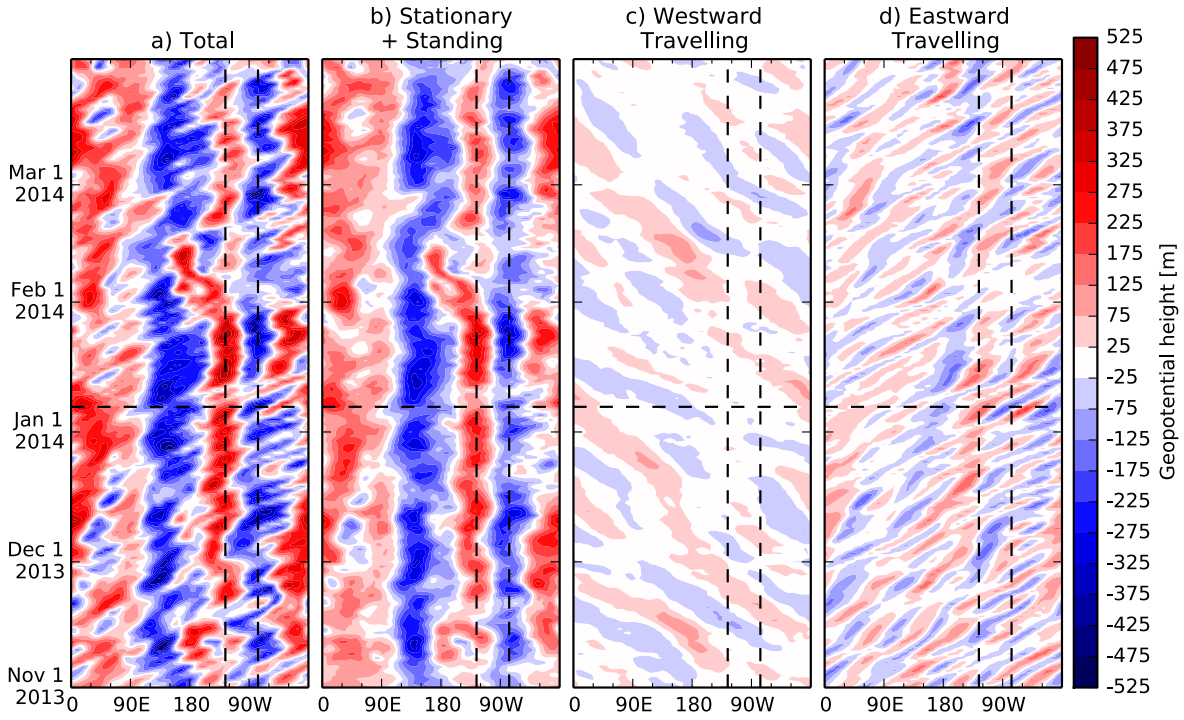

Figure 5.5: Z* at 500hPa and 47.5°N from 1 November 2013 to 31 March 2014. a) the total Z*, b) the standing part of Z*, c) the westward travelling part of Z*, d) the eastward travelling part of Z*. The vertical dashed lines show the centers of action of the DCI (see Section 5.2). The horizontal dashed line marks 7 January 2014.

5.3.2 The mid-latitude Z500 evolution during the 2013/14 winter

As an example of the time evolution of the mid-latitude tropospheric geopotential height field, Fig. 5.5 shows Hovmöller diagrams of Z500 and its standing and travelling components at 48°N for the 2013/14 winter season. The standing-travelling wave decomposition separates the geopotential height eddy field (Fig. 5.5a) into a standing wavefield (Fig. 5.5b), which is known to be driven by zonal asymmetries in surface topography and thermal forcing (Charney and Eliassen, 1949; Smagorinsky, 1953; Held, 1983) and shorter wavelength eastward travelling synoptic waves (Fig. 5.5d). The westward travelling wave field is relatively weak (Fig. 5.5c). The nodes of the DCI are marked by the vertical dashed black lines in Fig. 5.5. This makes it clear that the DCI was strong and positive throughout nearly the entire winter season, excepting periods in mid-November and mid-February. Furthermore, it is evident that around 7 January 2014 (marked by the horizontal dashed lines in Fig. 5.5) there was a strong eastward travelling wave which had the appropriate wavelength to drive the DCI. This event will be further explored in

Section 5.3.4.

As was discussed in Section 1.5, the seasonal or climatological mean of Z* is often taken as the quasi-stationary component driven by topography and thermal forcing. Figure 5.5b shows that our algorithm additionally includes subseasonal timescale variations, which are presumably related to transient variability in the thermal forcing, orographic forcing, and non-linear interactions between the mean field and the external forcing. The standing contribution to the dipole circulation index has an e-folding timescale (i.e. number of days after which the autocorrelation falls to a value of 1/e) of approximately 4.5 days which is about three times slower than that of the eastward travelling contribution (1.5 day e-folding timescale). This reflects the relatively greater spectral power of mid-tropospheric standing waves at the lowest frequencies (not shown). Thus, given the connection between the dipole circulation index and surface temperature, we refer to the standing and the eastward travelling waves as the slow and fast dynamical drivers of North American temperature variability.

5.3.3 Circulation-temperature connection

The dipole circulation index (DCI) defined in Section 5.2 links the mid-tropospheric atmospheric circulation over North America to the surface temperature anomalies in central eastern North America (CENA). When the DCI is positive, it indicates there is a ridge over western North America and a trough over eastern North America, leading to northerly geostrophic cold air advection over North America and thus the negative correlation between the DCI and CENA temperatures described in Section 5.2. During the winter of 2013/14, the average DCI was 293m and the average CENA temperature was -5.33°C, while during 2014/15 the DCI was 295m and the CENA temperature was -4.24°C (see also Figs. 5.1 and 5.2). These are two of the three highest winter-averaged DCIs since 1958/59. Furthermore, 2013/14 was the coldest winter and 2014/15 the 6th coldest since 1958/59 over the CENA region. Thus, in the seasonal average we can take the DCI as a good indicator of the large-scale atmospheric circulation's contribution to cold temperature fluctuations over CENA.

As expected from the discussion above, an anomalously positive DCI leads to significantly colder than normal temperatures over the eastern half of North America, and also warmer than normal temperatures over the northeast Pacific, Alaska and the west coast of North America (Fig. 5.6a). This temperature pattern is broadly similar to the

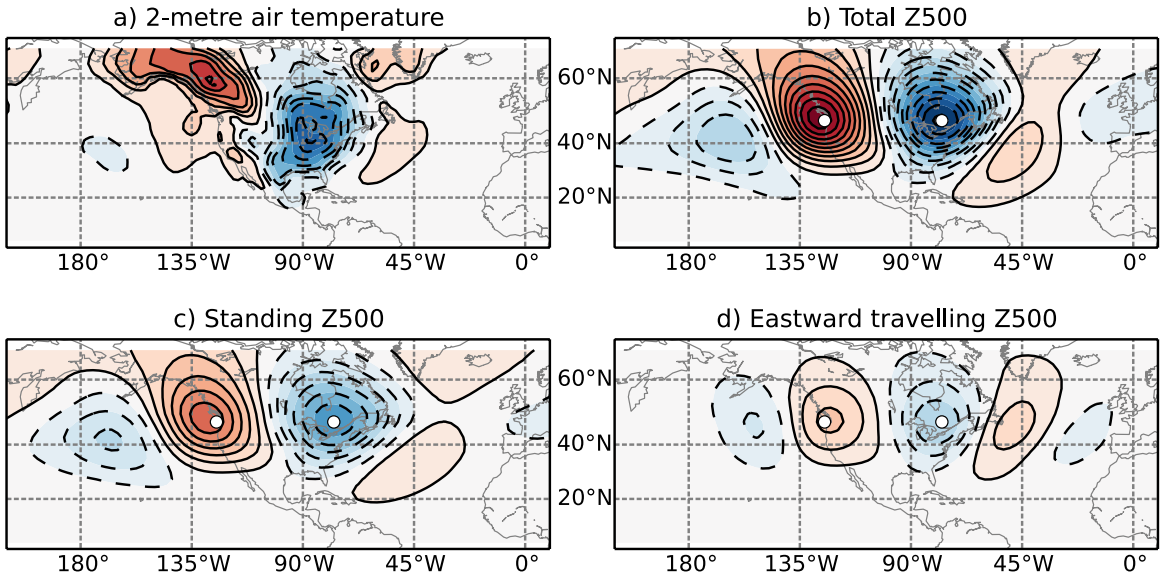

Figure 5.6: The regression of a) 2-metre air temperature; b) total Z500; c) standing part of Z500; and d) eastward travelling part of Z500 onto the normalized DCI. White circles indicate the centers of action of the dipole circulation index. Contours intervals are a) 0.25 K, 0.75 K, etc. and b)-d) 5m, 15m, etc. with positive values solid and negative values dashed. For all variables, the seasonal cycle is removed before regressions are computed. Statistical significance is computed following Lau and Chan (1983), accounting for autocorrelation in each timeseries. All regressions plotted are significantly different from zero at the 95% level or higher.

temperature anomalies seen over the 2013/14 and 2014/15 winters (Fig. 5.1). By construction, we expect strong positive and negative relationships between Z500 and the DCI at the western and eastern poles of the DCI, but Fig. 5.6b shows that the DCI is also connected to a large-scale wave train pattern that has connections to sub-tropical geopotential height variability. This pattern is reminiscent of the great circle wave trains resulting from sub-tropical thermal forcing (Hoskins and Karoly, 1981), and in particular is somewhat similar to the Pacific/North America pattern (see the left column of Fig. 5.4 and Wallace and Gutzler (1981)) although the centre of action in eastern North America is, by construction, shifted poleward. Separate regressions of the standing and eastward travelling parts of Z500 onto the DCI (Figs. 5.6c-d) elucidate the geographic structure of each of these components of the wave variability: the standing part drives the arcing connection with the sub-tropics while the eastward travelling part is a meridionally confined Rossby wave train of slightly shorter zonal scale. Figs. 5.6c-d also demonstrate that the standing wave field is the primary driver of the DCI (about 120m of geopotential height difference between the two centers of action per unit standard deviation of the DCI), while the eastward travelling wave typically makes contributions of smaller magnitude (about 60m of geopotential height difference). Generally, these conclusions are similar

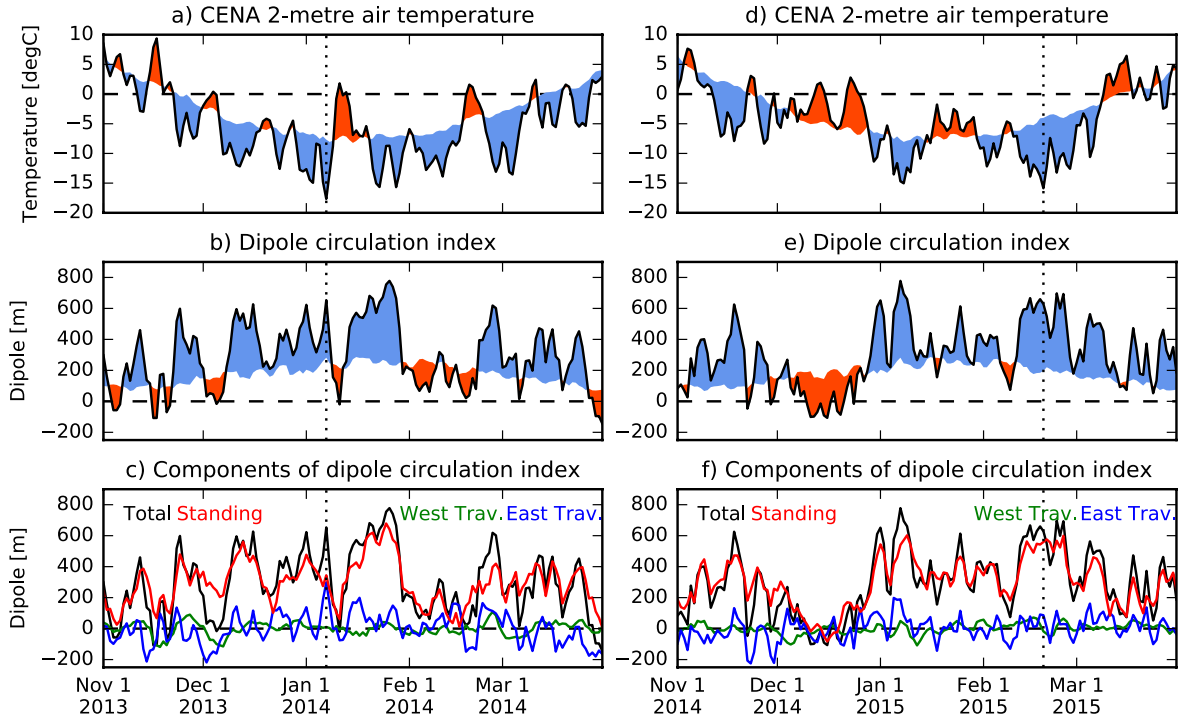

Figure 5.7: The 1 November 2013 to 31 March 2014 and 1 November 2014 to 31 March 2015 evolutions of a)/d) CENA 2-metre air temperature, b)/e) DCI and c)/f) the total (black), standing (red), westward travelling (green) and eastward travelling (blue) components of the DCI. In a), b), d) and e) the area between the climatological values and the 2013/14 or 2014/15 values are shaded in blue or red. 7 January 2014 and 19 February 2015 are marked by a vertical dotted line in panels a) to c) and d) to f) respectively.

to what was found in the single point correlation maps of Fig. 5.4. Finally, we note that the interpretation of the standing wave field's contribution to DCI being driven by subtropical variability is supported by the significant body of literature which demonstrates that variability, in particular anomalous convection and heating in the tropics, efficiently drives quasi-stationary extratropical wave patterns (Hoskins and Karoly, 1981; Wallace and Gutzler, 1981; Trenberth et al., 1998).

5.3.4 Circulation driven temperature anomalies during recent winters

CENA temperatures over the 2013/14 winter (Fig. 5.7a, which reproduces Fig. 1c of Screen et al. (2015)) were colder than normal for nearly the entire winter season. On 7 January 2014, they reached their lowest value of -17.7°C. As discussed by Screen et al. (2015), this event was extreme (the second coldest) in the context of the last 14 years, but a somewhat less rare event during previous decades. Figure 5.7b shows that through-

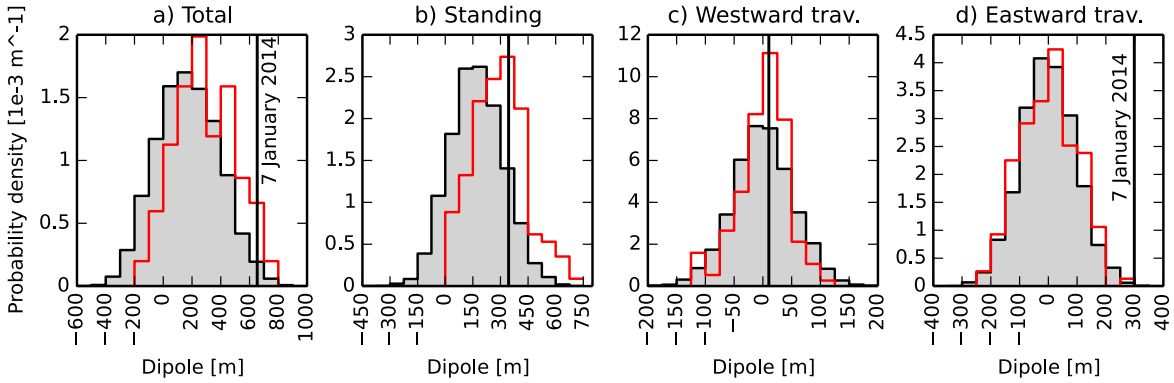

Figure 5.8: For all panels, in grey is the histogram of the DCI, or a component of it, over all winter days. In red is the histogram of the DCI over only 2013/14 winter days. The vertical black line marks the value of the DCI on 7 January 2014. a) Is the total DCI, b) the standing part, c) the westward travelling part and d) the eastward travelling part.

out most of the winter season, the DCI was larger than normal, consistent with cold-air northerly advection. On 7 January 2014, the DCI is anomalously large, but not exceptionally so: there are other days during the winter where the DCI reaches larger values. Given the correlation of -0.61 between the DCI and CENA temperatures, we cannot expect a one-to-one correspondence between extreme cold days and high DCI values, and other physical processes such as snow and lake ice cover have impacts on surface temperature which our circulation index does not capture. Figure 5.7c plots the contribution of the standing, eastward travelling and westward travelling waves to the DCI during the 2013/14 winter. Overall, the variability in the DCI is dominated by the standing wave component, with a smaller contribution from eastward travelling waves and an even smaller contribution from the westward travelling waves. However, on 7 January 2014, the eastward travelling wave has its largest value for the entire winter season while the standing wave contribution is moderate.

We now show the distribution of the DCI over the 2013/14 winter, and its value on 7 January 2014, in the context of the entire data record. Histograms of the DCI and its components over all winter seasons, and over just the 2013/14 winter (Fig. 5.8a) demonstrate that the distribution of the total DCI for 2013/14 is shifted towards more positive values. This confirms what was qualitatively seen in Fig. 5.7b, and is consistent with 2013/14 winter having the 3rd-largest seasonal mean DCI in the recent record. The overall positive shift in the total DCI is necessarily driven by the standing wave component (Fig. 5.8b) because the travelling components have zero seasonal-mean. Overall, the 2013/14 histograms of the westward and eastward travelling DCI are similar to the all-winters histograms. This suggests that in this winter, the overall fast dynamical vari-

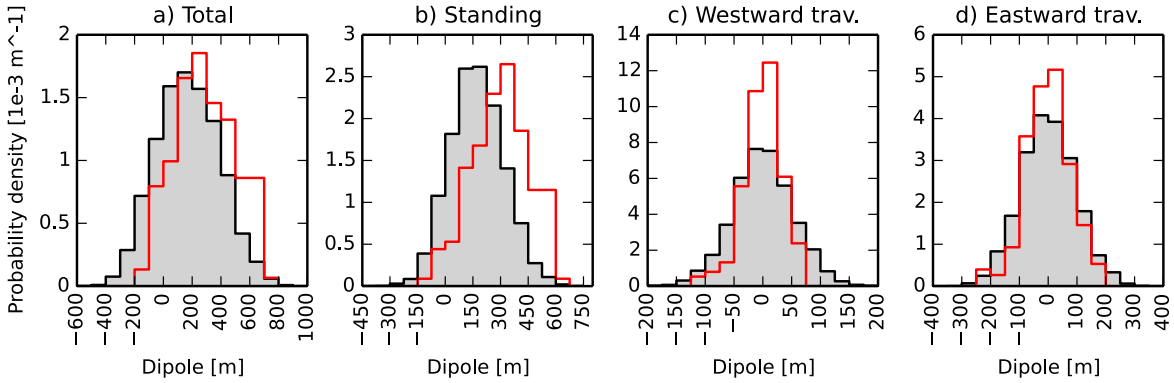

Figure 5.9: As in Fig. 5.8 but here the red histogram is for the 2014/15 winter.

ability was not exceptional compared to the climatological record. Figure 5.8 also shows the value of the DCI and its components on 7 January 2014, demonstrating that the total DCI on 7 January 2014 was quite anomalously positive: it is above the 98th percentile of all wintertime DCI values (95th percentile of 2013/2014 winter DCI values). This extreme value is attributable to the transient part of DCI variability: the standing wave part on 7 January 2014 is in the wings of the distribution, at the 88th percentile of all wintertime DCI values (64th percentile of 2013/2014 winter DCI values), but the eastward travelling part on 7 January 2014 is in the tail of the distribution, at the 99.96th percentile of all wintertime DCI values (and is the largest value of 2013/2014 winter DCI values). Thus, the travelling wave led to the rapidly intensifying extreme conditions on 7 January 2014. In summary, our analysis demonstrates that the climatological ridge-trough structure over North America was amplified throughout almost all of the 2013/14 winter season, and furthermore that the extreme cold-air outbreak of 7 January 2014 was driven by one of the strongest eastward travelling synoptic waves in the recent record, which reinforced this seasonal amplification.

The evolution of the CENA temperature and DCI over the more recent 2014/15 winter (Fig. 5.7d-f) is broadly similar to 2013/14: the temperatures are colder than normal and the DCI larger than normal throughout most of the winter season. However, there are important differences in the relative contributions of the standing wave and travelling wave components of the DCI compared to 2014/2015. There were no days with travelling wave DCI values during the 2014/15 winter that were as extreme as those found in 2013/2014 and both the westward travelling and eastward travelling components had less variance than normal over the 2014/15 winter (Fig. 5.9c,d). Consistently, the day with the largest negative anomaly of temperature over CENA, 19 February 2015, had its DCI almost entirely driven by the standing component (Fig. 5.7f). In addition,

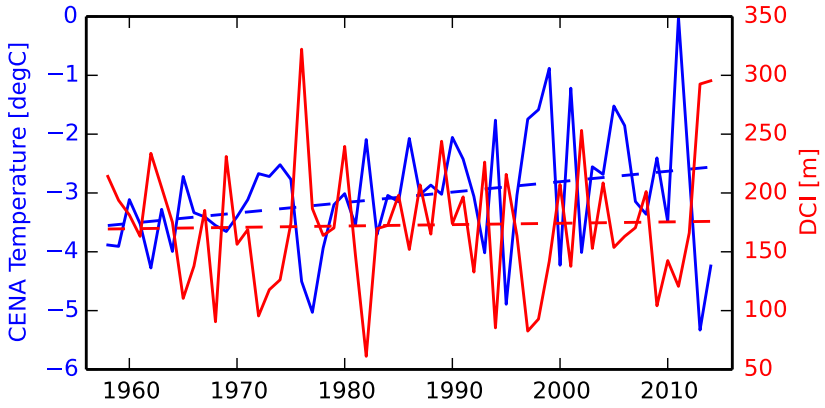

Figure 5.10: The winter-mean CENA temperature (blue) and DCI (red) from 1958/59 to 2014/15. The dashed lines are the trends computed with a least-squares best fit. The slope for the CENA temperature is 0.018°C/year, which is significantly different from zero with $p = 0.029$. The DCI slope is not statistically different from zero ($p = 0.79$).

the cold anomaly persisted for more than a week, which is stark contrast to the cold anomaly of 7 January 2014, which was followed on a few days later by a warm anomaly of almost the same magnitude, indicative of the fast synoptic driving of that event.

5.3.5 Long-term climate variability

Some recent studies have suggested that a possible increase in extreme weather events in the Northern Hemisphere mid-latitudes in the past decade (Coumou and Rahmstorf, 2012) may be due to increased wave amplitudes or changes in wave phase speed leading to more persistent weather patterns (Petoukhov et al., 2013; Screen and Simmonds, 2014; Coumou et al., 2014). Some authors have attributed these changes to sea-ice loss and Arctic amplification more generally (Francis and Vavrus, 2012; Cohen et al., 2014), while others have disputed the observational evidence for changes in wave amplitude (Screen and Simmonds, 2013; Barnes, 2013). While a detailed study of the impacts of climate change or other sources of long term climate variability on the standing and travelling wave fields is outside the scope of this chapter, in this section we do provide a short examination of the long-term variability in the DCI and its components.

Figure 5.10 shows the winter mean DCI and CENA 2-metre temperature from 1958/59 to 2014/15. The temperature shows a clear and statistically significant positive trend of 0.018°C/year. On the other hand, the DCI trend is not significantly different from zero. Thus, although there is an overall warming trend, we do not detect a trend in the reanalysis related to a change in the winter-mean zonally asymmetric part of the

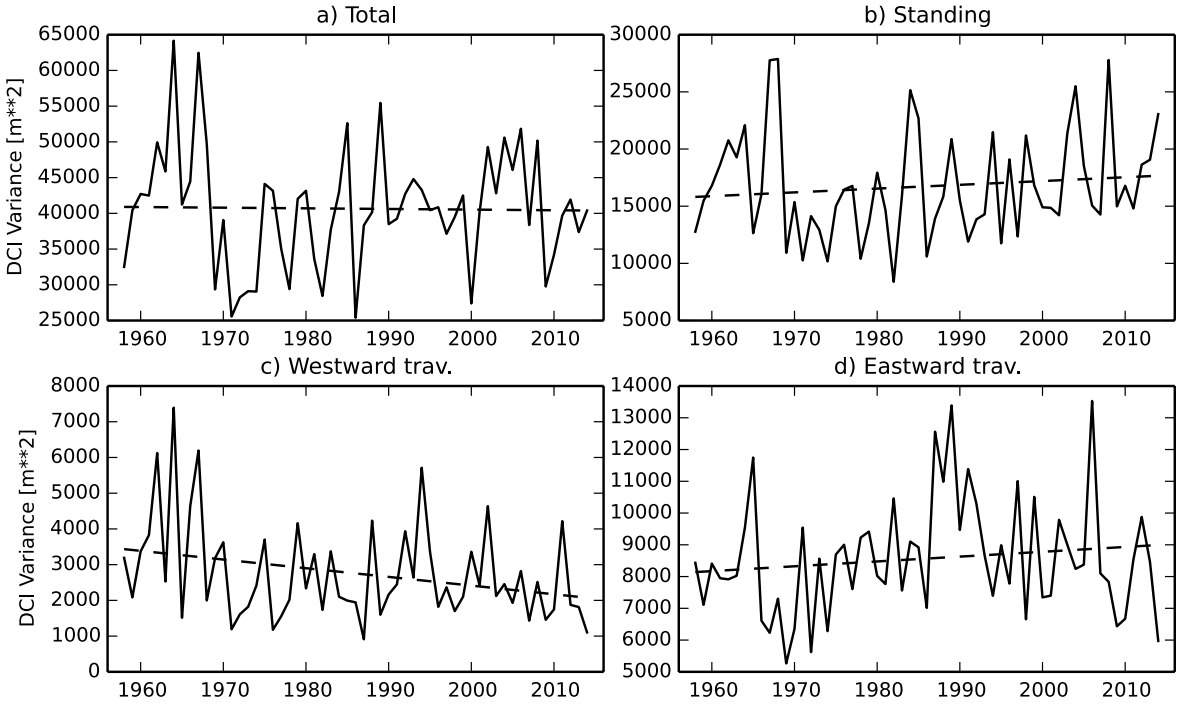

Figure 5.11: The variance of the DCI and its components over each winter season from 1958/59 to 2014/15. a) Is the total DCI, b) the standing part, c) the westward travelling part and d) the eastward travelling part. The westward travelling component is the only one with a statistically significant trend (-24 m^2 $year^{-}1$, $p = 0.027$).

circulation over North America over the last 55 years.

Beyond simply changes in the winter-mean circulation, it is possible that there have been changes in the intra-seasonal variability of the atmospheric circulation. To test this, we compute the variance of the DCI within each winter season, and plot this as a function of year (Fig. 5.11). The only component with a significant trend in variance (in this case decreasing) is the westward travelling DCI, but this component explains by far the least variance in the total DCI. For the more important standing and eastward travelling components, as well as the total, there is no significant trend in sub-seasonal DCI variance. Nevertheless, the DCI only captures the wave variability over a very particular part of the atmosphere, and it is possible that other regions or metrics would find robust changes in variability. For example, Blackport and Kushner (2016) found small but statistically significant changes in Z500 zonal wave amplitudes at 45°N during winter when sea-ice loss was imposed in a couple climate model. Applying the standing-travelling wave decomposition could be helpful in understanding the dynamical causes of the changes in amplitude in that context. This is planned future work and will be further discussed in Section 6.2.

5.4 Summary and conclusions

The standing-travelling wave analysis developed in Chapter 2 was applied here to the mid-tropospheric circulation in the extratropical Northern Hemisphere winter. It was shown that the spatial patterns of variability of the standing, westward travelling and eastward travelling waves are highly distinct, and that overall the standing wave explains the largest portion of variance of the variability of the total wavefield. It was confirmed that teleconnections such as the Pacific/North America pattern are captured by the standing wave component, while the eastward travelling wave variability is maximized in the storm track regions.

Next, a focus is made on the drivers of cold temperature extremes over central eastern North America. An index was constructed to capture the strength of the ridge-trough over North America, and it was shown to be related to temperatures over the central eastern North America region of interest. Using this index, it was found that the last two winters featured weather patterns that are anomalous in the context of the longer record, but the signature event of the 2013/2014 winter was the uniquely strong synoptic event of early January 2014, which led to rapid cooling of CENA. On the other hand, the cold anomalies of the 2014/15 winter, particular for the month of February 2015, were largely driven by a persistent standing wave anomaly. Note that some of the events that turn out to impact the 2013/2014 winter DCI were identified by Davies (2015) (see Figs. 1a,b and 2a of Davies (2015)), which demonstrated using trajectory analysis the high-latitude origin of air masses in the trough over eastern North America during these events. It would be of interest to extend our current work to see how the distinctive standing and travelling wave contributions to the flow in 2013/14 and 2014/15 would lead to different air mass transport in the two winters. In particular, our analysis suggests that synoptic systems can efficiently drive rapid cooling in the CENA region, and a trajectory analysis could help link this hypothesis to the polar origin of air masses on these short timescales.

Finally, no evidence of a connection to long-term climate variability has been found for the extreme synoptic event of early January 2014, nor has any evidence been found for statistically significant trends in the mean DCI or the variability of its main standing and eastward travelling components (Figs. 5.10 and 5.11). Future work is planned to study in more detail possible changes to the standing or travelling wave amplitudes outside the context of the North American ridge-trough dipole.

Chapter 6

Conclusions and Discussion

6.1 Summary

The primary aim of this thesis was to identify the structure of the planetary scale waves that drive variability in the strength of the stratospheric polar vortex in the Northern Hemisphere winter. The motivation for doing so lies in the fact that wave-driving of the polar vortex is the main control on its strength (Polvani and Waugh, 2004), and relatedly, on the temperature in the polar region of the stratosphere (Newman et al., 2001). The causes of changes in the strength of the polar vortex are important to understand because they tend to be followed by persistent shifts in the position of the eddy-driven jet stream in the troposphere (Baldwin and Dunkerton, 2001), leading to increased predictability on extended range timescales (Sigmond et al., 2013). The temperature distribution in the polar stratosphere on the other hand is fundamental for ozone chemistry, and the dynamical wave-driving of the Northern Hemisphere stratospheric vortex is a strong control on the amount of ozone loss in a given season (Fusco and Salby, 1999).

The particular question answered in this thesis regarding the variability of upward wave activity flux was whether it is primarily driven by standing waves fixed in place or by travelling wave modes. In order to address this question, a novel spectral decomposition of wave variability into standing and travelling components was developed. Techniques for such a decomposition had been previously proposed (Hayashi, 1973, 1977, 1979; Pratt, 1976) but they did not explicitly account for the covariance between standing and travelling waves, and did not provide a way to reconstruct the real space standing and travelling fields. The method proposed in Chapter 2 takes a slightly different approach

than previous authors, by directly decomposing the Fourier coefficients themselves into standing and travelling components, instead of decomposing the power spectra (i.e. the Fourier amplitudes squared). This allows for the explicit calculation of the covariance between the standing and travelling components, and the straightforward inversion of the decomposed Fourier coefficients to real space. In practice, the method proposed in this thesis estimates a similar amount of variance in standing waves compared to the historical methods of Hayashi and Pratt, but partitions what previous methods would exclusively attribute to travelling variance into both travelling variance and a covariance term. In Chapter 2, the method is applied to planetary scale geopotential height anomalies in the Northern Hemisphere winter. It is shown that standing waves tend to dominate variability at the lowest frequencies, but that there are certain frequencies at which travelling waves have clear spectral peaks. For example, there is a prominent westward travelling wave-1 mode with a period of approximately 25 days that is most dominant in the troposphere between approximately 60°N and 80°N. For shorter length scales (zonal wavenumbers 5 and higher) the eastward travelling component is strongest in the troposphere, as expected. Time-lagged correlations demonstrate that the westward travelling wave-1 in the high latitudes is roughly barotropic and coherent from the troposphere into the mid-stratosphere. On the other hand the standing wave-1 tends to be westward tilted with height, and its amplitude anomalies propagate from the troposphere to the stratosphere with a time lag of approximately 3-6 days.

In terms of the wave-driving of the stratosphere, an important consideration is whether the standing wave anomalies have a tendency to amplify and attenuate the climatological background wave. This is because it has been shown that amplifications of the climatological wave are in many cases the main way to drive changes in the strength of the polar vortex (e.g. Ineson and Scaife, 2009; Nishii et al., 2009; Garfinkel et al., 2010; Smith and Kushner, 2012). With regards to this point, Chapter 2 examines the typical positions of the antinodes of the standing waves at various levels. It was shown that in the lower stratosphere, the wave-1 standing wave has preferred longitudes for its antinodes, and they are closely aligned with the maximum and minimum of the climatological wave-1. This suggests that the standing waves should, at least for wave-1, explain a large portion of the variance of the part of the upward wave activity flux that is due to interference of wave anomalies with the climatological wave (i.e. the LIN term).

Chapter 3 tests this idea by applying the standing-travelling wave decomposition developed in Chapter 2 to the meridional wind and temperature anomalies in the North-

ern Hemisphere winter in order to separate the heat flux variability into contributions from standing and travelling waves. It is shown that especially on longer timescales (>15 days) the standing wave anomalies dominate both extreme heat flux events, and the overall variability of the LIN term. This is in part because the standing component of the LIN term is the most persistent part of the heat flux. In turn, this can be attributed to the fact that the standing waves are dominated by the lowest frequencies, as was shown in Chapter 2. The importance of standing waves amplifying and attenuating the climatological wave for driving changes in the strength of the stratospheric polar vortex is explicitly tested by computing lag-correlations between components of the heat flux at various levels with the NAM at 10hPa. This shows that heat flux anomalies in the troposphere preceding changes in the strength of the stratospheric polar vortex are mostly driven by standing waves amplifying the climatology, with a shorter contribution at a lag of approximately -10 days coming from the travelling component. Furthermore, it is shown that filtering for the wave-1 heat flux anomaly (or wave-1 LIN term) makes the connection between tropospheric upward wave activity flux and 10hPa NAM stronger, indicating that higher wavenumber variability in the troposphere masks the connection between upward wave activity flux and polar vortex strength. It is shown that atmospheric general circulation models with good stratospheric resolution are capable of simulating the observed connection between heat fluxes and 10hPa NAM. Finally, the precursors to split and displacement sudden stratospheric warmings are computed. This demonstrates that displacement warmings are primarily driven by standing waves amplifying the climatology, while split events have an additional significant contribution from the NONLIN term.

Although the primary focus of this thesis is on the roles of standing and travelling waves in driving variability in upward wave activity flux and polar vortex strength, two additional extensions motivated by the work in Chapters 2 and 3 were made. First, Chapter 4 attempted to explain the causes of the positive skewness of upward wave activity flux. It was shown that the positive skewness can be understood through the strong relationship between the LIN and NONLIN terms that was found to exist when each of the terms was filtered by wavenumber. The dependency is seen most clearly for wave-1 in the Northern Hemisphere winter. Briefly, it is observed when the wave-1 LIN term is strongly negative or positive, the wave-1 NONLIN term tends to be large and positive. This means that they tend to cancel when LIN is negative, but amplify each other when LIN is positive, and we argue that this leads to the positive skewness of the total heat flux anomaly. The relationship between the LIN and NONLIN terms exists

because of the westward tilt with height of the climatological wave. This is because the westward tilted climatology means that a large amplitude (positive or negative) LIN will coincide with a westward tilted wave anomaly, and this in turn implies a positive NONLIN term. This argument is verified through the use of a toy model that computes heat flux as a function of the wave anomaly amplitude, phase and tilt, and climatological wave amplitude, phase and tilt. It is shown that the heat flux distribution skew depends strongly on climatological wave tilt, and goes to zero as the climatology becomes barotropic. Furthermore, the toy model is used to identify the characteristics of the wave anomaly parameter distributions that are important for setting the asymmetries of the LIN (which is negatively skewed for wave-1) and NONLIN (which is positively skewed) distributions. It is found that the negative skew of the LIN term is due to a relationship between phase and amplitude in which wave anomalies that are out of phase with the climatology tend to be of higher amplitude than those that are in phase. The positive skewness of the NONLIN term is due to westward tilted wave anomalies tending to be of larger amplitude than eastward tilted anomalies. A similar relationship between the LIN and NONLIN terms exists for wave-2 in the Northern Hemisphere and wave-1 in the Southern Hemisphere.

The second extension made in this thesis was the application of the standing-travelling wave decomposition to the mid-tropospheric wintertime circulation in the Northern Hemisphere, with a particular focus on the drivers of cold winter weather over central eastern North America. Although the behaviour of standing and travelling waves in the troposphere was touched on in Chapter 2 (e.g. Fig. 2.5), the primary focus there was on the planetary scale waves which are able to propagate into the stratosphere. In Chapter 5, the role of standing and travelling waves in tropospheric wave variability was explored. Because the Northern Hemisphere's tropospheric circulation is a complex combination of quasi-stationary waves, westward travelling planetary scale waves and eastward travelling synoptic waves, it is an ideal testbed for the standing-travelling wave decomposition. By computing the variance over time of the 500hPa geopotential height, and its standing, eastward travelling and westward travelling subcomponents, it was shown that each of these parts of the wavefield has its variability maximized in different regions, suggesting different dynamics may be driving each component. In terms of overall variance explained, the standing wave dominates, followed by eastward travelling waves, particularly between 30°N and 60°N, and westward travelling waves, particularly between 60°N and 80°N. The standing wave variance is largest over the North Pacific and North Atlantic oceans, the westward travelling variance is nearly zonally uniform, and

the eastward travelling variance is maximized over the storm track regions. One-point correlation maps show that standing wave variability is associated with teleconnection patterns such as the Pacific/North America pattern or the North Atlantic Oscillation, while eastward travelling waves consist of synoptic wave packets. This understanding was then applied to identifying the drivers of cold winter weather in eastern North America. It was shown that a measure of the strength of the ridge-trough across North America correlates well with the surface air temperature over eastern North America. Furthermore, although standing waves explain the majority of the variance of the ridge-trough strength, on shorter timescales eastward travelling waves can also significantly modulate its strength. In particular, it was shown that during the winter of 2013/14, standing wave anomalies amplified the ridge-trough throughout most of the season, but that the particularly strong cold air outbreak of 7 January 2014 was driven by one the largest amplitude eastward travelling waves on record. On the other hand, the ridge-trough during the cold winter of 2014/15 was not as strongly driven by synoptic waves, and accordingly the cold anomalies were more persistent during that winter. No significant changes over the historical period (since 1958) were found in the winter-mean ridge-trough strength, or of the intra-seasonal variability in the total, standing or eastward travelling components of the ridge-trough.

Considering the entirety of this thesis, there are a few points that stand out as worthwhile to emphasize. First, the development of a novel decomposition of wave variability into standing and travelling components is an important new technical development. The most significant improvements of this method over previous ones are that it allows for the reconstruction of real space standing and travelling wave fields and that it explicitly accounts for the covariance between the two. In this thesis, the decomposition has allowed for an improved understanding of the structure of the wave anomalies that drive the linear interference effect. It has been used to show that standing waves, which dominate the planetary scale geopotential height variability at the lowest frequencies, are responsible for the longer persistence of the LIN term. Standing waves amplifying and attenuating the climatology largely explain the connection between tropospheric upward wave activity flux and stratospheric polar vortex strength, and they also are significant precursors for displacement sudden stratospheric warmings. This suggests that monitoring the standing wavefield may be helpful in the prediction of extreme changes in the strength of the stratospheric polar vortex. This will be further discussed in the next section.

Second, by analyzing the terms individually for wave-1 and wave-2, a clear relationship between the LIN and NONLIN terms has been found. Briefly, because of the westward tilt of the climatological wave, when the LIN term is negative it tends to be cancelled by a positive NONLIN term, and when it is positive it gets amplified by a positive NONLIN term. This relationship was used in Chapter 4 to explain the positive skewness of the wave-1 heat flux distribution in the Northern Hemisphere lower stratosphere. A simple statistical model was developed which allowed for the attribution of certain aspects of the heat flux distributions to aspects of the wave anomaly parameter distributions (such as relationships between wave anomaly amplitudes and phases). We were motivated to understand the skewness of the heat flux distribution because of its implications for the distribution of temperatures in the polar stratosphere, which strongly impacts ozone chemistry processes. However, there is still more work necessary to clarify the connection between the skews of the heat flux and temperature distributions. Possible ways to address this will be outlined in Section 6.2.

Finally, in Chapter 5, the standing-travelling decomposition was used to analyze the mid-tropospheric circulation in the Northern Hemisphere winter. Although the focus was on understanding the large-scale circulation patterns that lead to cold surface temperatures over eastern North America, like those that were seen over the winters of 2013/14 and 2014/15, the potential for this method to provide broader insights into tropospheric dynamics is significant. Chapter 5 showed that the technique provides a simple way to separate variability into quasi-stationary and travelling components without the need for an explicit time scale separation, as is often used in such an analysis (e.g. Blackmon, 1976). The next section will further discuss possible applications for the standing-travelling decomposition, and in particular its potential use in understanding future changes in eddy amplitudes in the troposphere.

6.2 Future work

Given the development in this thesis of a new method for the separation of wave variability into standing and travelling components, one obvious avenue of future work lies in exploiting this technique in new contexts. For example, as was briefly described in Section 2.3.7, the method can be applied to convectively-coupled equatorial waves that are detectable in spatio-temporal spectra of outgoing longwave radiation. Further work could extend this analysis, and in particular focus on mixed-Rossby gravity waves

and eastward inertio-gravity waves. These are particularly interesting in the context of standing-travelling wave because their dispersion relation crosses the $k = 0$ line, and thus they will have a mixture of travelling and standing wave power. Some recent studies have focused on this part of the antisymmetric OLR spectrum, and used empirical orthogonal function analysis and object identification techniques to determine whether the MRG and EIG waves primarily consist of standing or travelling waves (Kiladis et al., 2016; Dias and Kiladis, 2016). It would be interesting to isolate this part of the spectrum, and apply the standing-travelling decomposition described in Chapter 2 as well as correlation coherence analysis to provide another perspective on this question.

There are also other geophysical situations in which this type of spectral analysis could be useful. For example, in the southern tropical Indian Ocean slowly westward propagating Rossby waves (periods from 3 to 5 years) have been identified in fields such as sea surface height, sea surface temperature and meridional surface wind (Masumoto and Meyers, 1998; White, 2000). However, there are also standing waves in this basin that interfere with the propagating signal and make its detection difficult during certain periods. White (2000) used a complex empirical orthogonal function analysis to separate the dominant propagating and standing signals (see also Appendix of White and Cayan (2000)). It would be interesting to compare how the spectral decomposition developed in this thesis would distinguish the standing and travelling waves in the southern tropical Indian Ocean. It should be noted that the spectral estimates of the power of the standing and propagating components used by White and Cayan (2000) and White (2000) are similar to the method of Pratt (1976) and do not account for the covariance between them.

Chapter 3 documented the connection of heat fluxes to variability of the strength of the stratospheric polar vortex. Following this work, it would be helpful to more carefully document the potential for the monitoring of the standing wave field to increase the predictability of SSWs. It was shown in Figs. 3.6 and 3.10 that there are persistent anomalies in the standing component of the LIN heat flux preceding changes in the strength of the polar vortex, and preceding displacement SSWs. Thus, knowing the state of the standing wave field on a particular day could be helpful in making predictions of upcoming changes in stratospheric polar vortex strength. However, because the decomposition into standing and travelling waves is made in spectral space, it is not trivial to make the decomposition operationally (i.e. before having a complete winter's data). The following are two possible ways this could be achieved. First, current data could

be projected onto typical modes that represent different phases of the standing wave variability. This would be analogous to how the Madden-Julian Oscillation's "Real-Time Multivariate MJO" index is calculated (Wheeler and Hendon, 2004). Another way to operationally compute the standing wave field would be to simply use a time period up to the current date (i.e. the preceding 151 days, if using the same length as in Chapters 2 and 3). However, this would have the effect that the estimated standing/travelling wave fields for a particular day would possibly change as the season progressed. For example: the calculated fields for a particular day, say January 1, would be different using a time period centred on January 1 versus ending on January 1.

Work on understanding the predictability of extreme stratospheric events in modern atmospheric models is underway by multiple research groups. For example, the Stratospheric Network for the Assessment of Predictability (SNAP) is coordinating hindcast experiments from various modelling centres to quantify the ability of numerical weather prediction systems to predict particular SSW events (Tripathi et al., 2015, 2016). Examining the split SSW event of 7 January 2013, Tripathi et al. (2016) found that the five modelling systems used were generally able to predict the event with a lead time of 10 days, but not if initialized 15 days before the event. When initialized with this longer lead time, models were typically able to properly forecast the wave-1 upward wave activity flux that preceded the event, but failed to simulate the amplification of the wave-2 component in the stratosphere that coincided with the event. Similarly, Taguchi (2016) has found that hindcasts by the Japan Meteorological Agency more accurately simulated SSWs with low aspect ratios (i.e. those with an initially more symmetric polar vortex) and large latitudinal displacements. Effectively, the hindcasts better forecast displacement-like events versus split-like events. These results are in accordance with what was found in Chapter 3: displacement SSWs have longer-lived precursors consisting of standing waves driving the LIN heat flux term, while split SSWs have shorter NONLIN heat flux precursors, suggesting the displacement events may be more predictable. In future work, it would be interesting to apply the linear interference framework and the standing-travelling wave decomposition to the hindcasts performed for the SNAP project.

In Chapter 4 the causes of the positive skewness of the heat flux distribution in the polar stratosphere were explored. The motivation for doing so was to explain the positive skewness of the temperature distribution in the stratosphere, which is important for ozone chemistry and stratosphere-troposphere coupling. However, the link between the skews

of the two distributions was not clearly established. It is known that mid-stratospheric temperature and polar vortex strength is closely controlled by time-integrated upward wave activity flux in the lower stratosphere (Newman et al., 2001; Polvani and Waugh, 2004), but the implications of this for the relationship between the skews of the two distributions is unclear. Future work will address this by developing a stochastic model that simulates the connection between upward wave activity flux in the lower stratosphere and temperature in the polar mid-stratosphere. By forcing this model with varying distributions of upward wave activity flux, it will be possible to clearly demonstrate whether the skewness of the wave activity flux distribution is indeed relevant for the skewness of the temperature distribution. The model itself would be an AR(1) process of the form $T_{n+1} = \alpha T_n + F_n$ where T_n and F_n represent the polar stratospheric temperature and upward wave activity flux at time step n, respectively. The forcing F_n could be sampled from observations, artificially generated, or some combination of the two. For example, it is known that polar stratospheric temperature (or polar vortex strength) is well correlated with upward wave activity flux that is integrated over a relatively long (approximately 40 day) period (Newman et al., 2001; Polvani and Waugh, 2004). For this reason, it may be necessary to use a quantity that represents the time-averaged upward wave activity flux for F_n instead of the actual daily quantity.

Beyond the relationship between fluxes and temperature, there are other outstanding questions from the work in Chapter 4. For example, the cause of the relationship between phase and amplitude for wave-1 anomalies in the Northern Hemisphere that leads to a negatively skewed wave-1 LIN term is not understood. The relationship suggests that there is an upper limit on the amplitude of the total (i.e. climatology + anomaly) wave, since the largest amplitude anomalies tend to happen when they are destructively interfering with the climatology, but this requires further study. There are other open questions. For example, why is the dependence between the LIN and NONLIN terms seen for wave-1 and wave-2 individually, but not when all wavenumbers are summed together? It is possible that this is due to a relationship between wave-1 and wave-2 heat fluxes, but this has not been explored in this thesis. Furthermore, the implications of the LIN/NONLIN relationship for the explanation of the stratospheric response to surface forcing such as Eurasian snow cover or tropical sea surface temperature anomalies remain unexplored. As an example, experiments with a simplified general circulation model in which a surface cooling is imposed at various longitudes have shown that that the stratospheric response is largely determined by the LIN term (Fig. 6 of Smith et al. (2010)). However, the relationship in those experiments between the LIN term and the

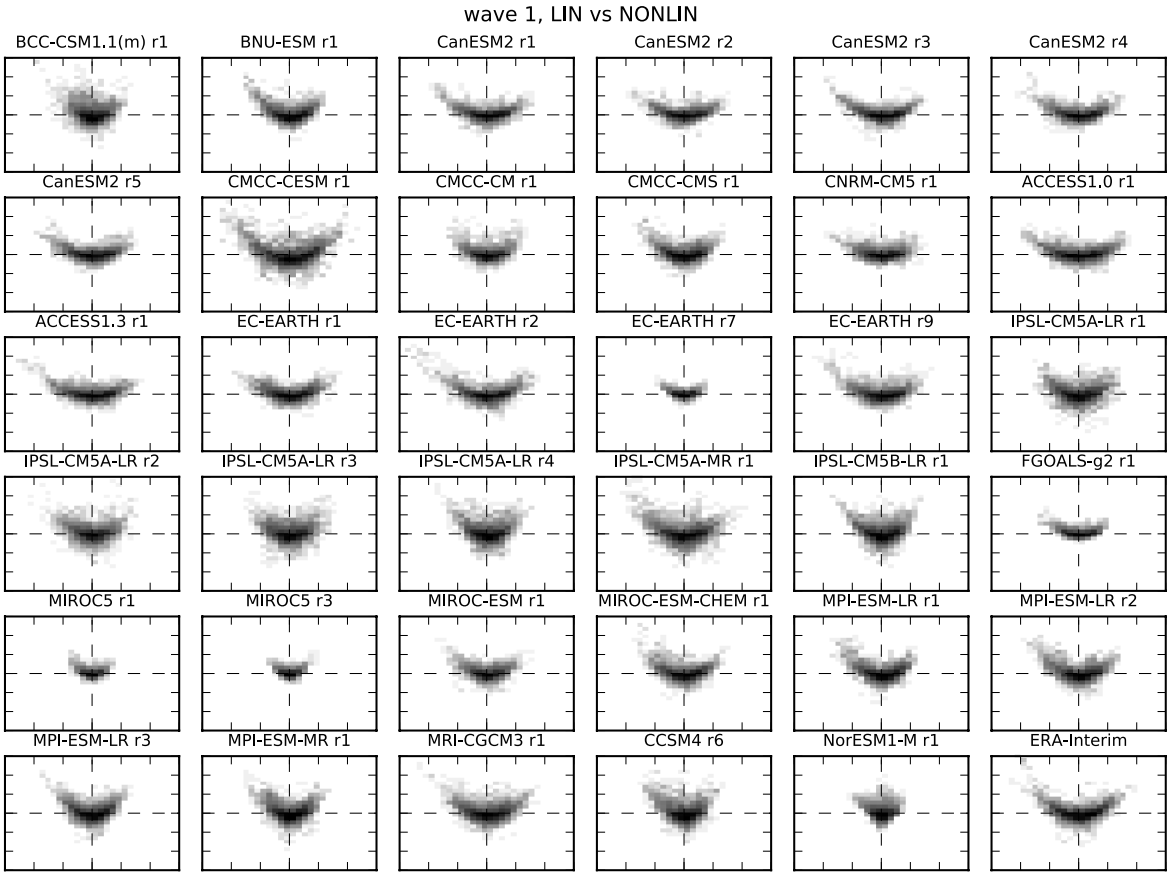

Figure 6.1: 2D histograms of daily mean wave-1 LIN (abscissa) versus wave-1 NONLIN (ordinate) at 60°N and 100hPa, using all 1979-2015 DJF days from CMIP5 historical and RCP8.5 experiments for multiple CMIP5 models and realizations. Data from the ERA-Interim reanalysis (1979-2013) is shown in the bottom right panel.

total heat flux anomaly is close to linear (Fig. 6c of Smith et al. (2010)) suggesting there is no cancellation with the NONLIN term when LIN is negative. Further work is needed to understand why this is. Possibilities include the fact that all wavenumbers are being included in the Smith et al. (2010) results, that the time-averaging done in that work eliminates the relationship, or finally, there may be some fundamental difference between the internal variability of the atmosphere that was studied in Chapter 4 and the forced response of Smith et al. (2010).

It would also be of interest to know whether modern climate models correctly simulate the relationship between the LIN and NONLIN terms, and relatedly the positive skewness of heat flux. Figure 6.1 shows 2D histograms of wintertime wave-1 LIN versus wave-1 NONLIN at 60°N and 100hPa (i.e. the same quantity that was plotted in Fig. 4.5e) for a variety of models from the Coupled Model Intercomparison Project phase 5 (CMIP5) (Taylor et al., 2012). The data is computed using merged historical and

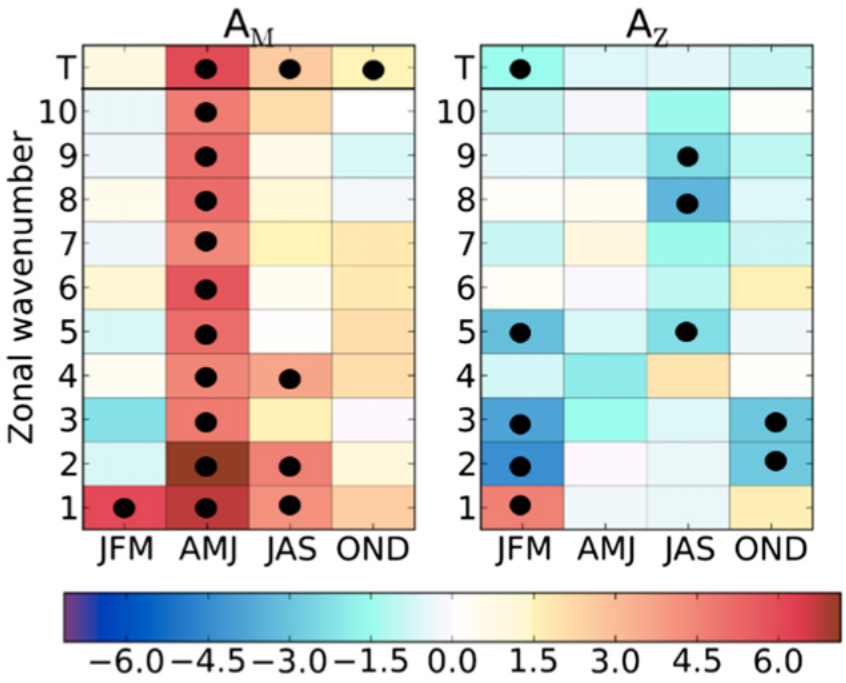

Figure 6.2: The equilibrium response in planetary wave amplitude (% change) in all four seasons and the first 10 wavenumbers, as well as the total amplitude (T) for (left) A_M and (right) A_Z. The isopleths used for A_M are 5400, 5500, 5700, and 5600 m for winter (JFM), spring (AMJ), summer (JAS), and fall (OND), respectively. The black dots indicate a 95% statistical significance using a Student's t test on the seasonal averages of the daily amplitudes. Reproduced from Blackport and Kushner (2016).

RCP8.5 experiments, over the years 1979-2015. The histogram computed from reanalysis data is shown in the bottom-right panel for comparison. Figure 6.1 shows that nearly all of the CMIP5 models for which data was available show at least in a qualitative sense the correct relationship between LIN and NONLIN. However, there is substantial variation in the details of the histograms. For example, a substantial number of models underestimate the variance in the LIN and NONLIN terms. Further work will compare the skews of the anomaly heat flux distributions, and investigate whether a relationship between climatological wave tilt and skew exists across CMIP5 models, as was found using the statistical model of Chapter 4 (i.e. Fig. 4.9). Although the potential for applying this analysis to the CMIP5 ensemble is somewhat limited by the availability of daily data (and when daily data is available, by its limited vertical resolution), within the framework of the Dynamics and Variability Model Intercomparison Project (DynVarMIP) (Gerber and Manzini, 2016) which will be a part of the CMIP6 effort (Eyring et al., 2015), there will be a significantly greater availability of high temporal and vertical resolution output data which will make this analysis more tractable.

Chapter 5 applied the standing-travelling wave decomposition to the wintertime tro-

pospheric circulation in the Northern Hemisphere. The historical changes in the winter-mean strength and intra-seasonal variability of the ridge-trough over North America—or dipole circulation index (DCI)—were calculated. No significant trend in the winter-mean DCI or variability in the total, standing or eastward travelling parts of the DCI were found. Nevertheless, some studies have suggested that there have been, or will be, changes in wave amplitudes in the mid-latitudes as a result of climate change (Francis and Vavrus, 2012) although the statistical significance of these results is disputed (e.g. Barnes, 2013; Screen and Simmonds, 2013). As a specific example of a plausible forced response to Arctic amplification, Blackport and Kushner (2016) found changes in wave amplitudes in experiments with a coupled atmosphere-ocean model in which sea ice loss was imposed by artificially changing the albedo of the sea ice. Figure 6.2, which is reproduced from Blackport and Kushner (2016), shows the differences in two measures of wave amplitudes between simulations with and without sea ice loss imposed. In particular, these metrics (see Screen and Simmonds (2013) for details of their computation) are designed to measure the meridional waviness of the mid-tropospheric circulation (A_M, the meridional extent of a given Z500 isopleth), and the zonal eddy amplitude at a particular latitude (A_Z). Here we will focus on the A_Z metric since it is most easily related to the spectral decomposition introduced in Chapter 2 and the dipole circulation index defined in Chapter 5. Briefly, it is the amplitude of a particular Fourier harmonic of the 500hPa geopotential height at 45°N. Figure 6.2 shows that during winter there is a statistically significant increase in amplitude of wave-1 A_Z, and decreases in amplitude for wave-2 through wave-10, with these decreases being statistically significant for wave-2, wave-3 and wave-5. However, it is not clear what the dynamical causes of these changes in wave amplitude are. Insight to this question could be gained by separating the wave amplitude changes into standing, eastward travelling and westward travelling components. For example, changes in the meridional gradient of temperature caused by the surface Arctic amplification associated with sea ice loss could potentially lead to changes in baroclinicity and hence synoptic wave amplitudes. An analysis of contributions of standing and travelling waves to the amplitude changes seen in Fig. 6.2 is underway.

It would also be helpful to understand the representation of tropospheric standing and travelling waves in other coupled model simulations. Lucarini et al. (2007) and Di Biagio et al. (2014) have documented their simulation in the CMIP3 and CMIP5 ensembles, respectively, but both of these studies used the older methods of Hayashi and Pratt, which we showed in Chapter 2 have significant issues with the lack of representation of the covariance between standing and travelling waves. Thus, possible future work will

apply the new spectral decomposition developed in Chapter 2 to a current ensemble of coupled model simulations, including potentially the upcoming CMIP6 ensemble (Eyring et al., 2015).

To conclude, this thesis developed a novel spectral decomposition of wave variability into standing and travelling components. It applied it to planetary scale waves in the Northern Hemisphere winter in order to understand the structure of the waves that interfere with the climatological wave and ultimately drive changes in the strength of the stratospheric polar vortex. It was shown that standing waves are the dominant driver of such interference, and are important precursors to displacement sudden stratospheric warmings. The positive skewness of the upward wave activity flux distribution was explained by appealing to a newly shown relationship between the LIN and NONLIN terms. This may have important implications for the cause of the skewness of the temperature distribution in the stratosphere. Finally, the standing-travelling wave decomposition was applied to the mid-tropospheric flow in the Northern Hemisphere winter, and the large-scale circulation patterns associated with cold surface temperatures over eastern North America were shown. The future work outlined in this section will be important in further emphasizing the relevance of the research completed in this thesis.

Appendices

Appendix A

Spectral identities and derivations

A.1 Inverse Fourier transform of real signal

The inverse 2D discrete Fourier transform is conventionally written as

$$q(\lambda, t) = \frac{1}{NT} \sum_{k=1}^{N-1} \sum_{j=0}^{T-1} e^{ik\lambda + i\omega_j t} \hat{q}_{k,j}. \tag{A.1}$$

Noting that $\hat{q}_{k,j} = \hat{q}_{N+k,T+j}$ and assuming for convenience that N and T are odd (which is not strictly necessary), one can rewrite Equation A.1 as

$$q(\lambda, t) = \frac{1}{NT} \sum_{k=-N_2}^{N_2} \sum_{j=-T_2}^{T_2} e^{ik\lambda + i\omega_j t} \hat{q}_{k,j} \tag{A.2}$$

where $N_2 = (N-1)/2$ and $T_2 = (T-1)/2$. Furthermore, given that $q(\lambda, t)$ is a real-valued function, we have $\hat{q}_{-k,-j} = (\hat{q}_{k,j})^\dagger$. Thus we can keep only half the Fourier coefficients. Recalling that $q(\lambda, t)$ has zero zonal-mean, we can rewrite Equation A.2 as

$$\begin{aligned} q(\lambda, t) = &\frac{1}{NT} \sum_{k=1}^{N_2} \sum_{j=-T_2}^{T_2} e^{ik\lambda + i\omega_j t} \hat{q}_{k,j} \\ &+ \frac{1}{NT} \sum_{k=-N_2}^{-1} \sum_{j=-T_2}^{T_2} e^{ik\lambda + i\omega_j t} \hat{q}_{k,j}. \end{aligned} \tag{A.3}$$

Then, using that

$$\begin{aligned}\sum_{k=-N_2}^{-1}\sum_{j=-T_2}^{T_2} e^{ik\lambda+i\omega_j t}\hat{q}_{k,j} &= \sum_{k=1}^{N_2}\sum_{j=-T_2}^{T_2} e^{-ik\lambda+i\omega_j t}\hat{q}_{-k,j} \\ &= \sum_{k=1}^{N_2}\sum_{j=-T_2}^{T_2} e^{-ik\lambda-i\omega_j t}\hat{q}_{-k,-j} \\ &= \left(\sum_{k=1}^{N_2}\sum_{j=-T_2}^{T_2} e^{ik\lambda+i\omega_j t}\hat{q}_{k,j}\right)^{\dagger}, \end{aligned} \tag{A.4}$$

where the second equality holds because we are summing over a symmetric (about zero) range of integers j, we see

$$q(\lambda,t) = \frac{2}{NT}\sum_{k=1}^{N_2}\sum_{j=-T_2}^{T_2} \mathrm{Re}\left(e^{ik\lambda+i\omega_j t}\hat{q}_{k,j}\right). \tag{A.5}$$

Rewriting the Fourier coefficients in terms of their amplitudes and complex phases, $\hat{q}_{k,j} = Q_{k,j}e^{i\phi_{k,j}}$, we have our reformulated inverse 2D discrete Fourier transform:

$$q(\lambda,t) = \frac{2}{NT}\sum_{k=1}^{N_2}\sum_{j=-T_2}^{T_2} Q_{k,j}\cos\left(k\lambda+\omega_j t+\phi_{k,j}\right). \tag{A.6}$$

It is trivial to rewrite this in the form of Eq. 2.2 given that $q(\lambda,t)$ as zero time-mean.

A.2 Longitude of standing wave antinodes

Hayashi (1973, 1977) and Pratt (1976) provide a formula for computing the longitudes of the antinodes of the standing part of a signal in terms of the power spectra and cross-spectra of $c_k(t)$ and $s_k(t)$ (note, in this section we follow the notation of Hayashi and Pratt, as outlined in Section 3.22.2.3). In particular, Hayashi (1973) defines[1]

$$\alpha = \tan^{-1}\left(\frac{2K_\omega(c_k,s_k)}{P_\omega(c_k)-P_\omega(s_k)}\right) \tag{A.7}$$

[1]Note Eq. 3.3 in Hayashi (1973) is erroneously missing the $\tan^{-1}$. See, for example, Eq. 13 of Pratt (1976) or Eq. 4.3 of Hayashi (1977).

and shows that the longitudes of the maximum time-variance of the signal are given by

$$\lambda = \frac{m\pi + \alpha/2}{k} \tag{A.8}$$

where m is an integer. We showed in Section 3.22.2.1 that the longitudes of the antinodes of the standing wave at wavenumber k and frequency ω_j are given by $\lambda = \frac{1}{k}(m\pi - \overline{\phi}_{k,j})$ with $\overline{\phi}_{k,j}$ defined in Eq. 2.8. Thus, to demonstrate the equivalence between our formula and Hayashi's, we must show that $\alpha = -2\overline{\phi}_{k,j}$.

We begin by rewriting Eq. 2.7 in the form of Eq. 2.13. Note for simplicity we take $Q^{\mathrm{St}}_{k,j} = 1$, although the derivation holds generally. Straightforward algebraic manipulations can be used to show that

$$q^{\mathrm{St}}_{k,\pm j}(\lambda, t) = c_k(t)\cos k\lambda + s_k(t)\sin k\lambda \tag{A.9}$$

where

$$\begin{aligned} c_k(t) =& (\cos\phi_{k,j} + \cos\phi_{k,-j})\cos\omega_j t \\ &+ (-\sin\phi_{k,j} + \sin\phi_{k,-j})\sin\omega_j t \end{aligned} \tag{A.10}$$

and

$$\begin{aligned} s_k(t) =& (-\sin\phi_{k,j} - \sin\phi_{k,-j})\cos\omega_j t \\ &+ (-\cos\phi_{k,j} + \cos\phi_{k,-j})\sin\omega_j t. \end{aligned} \tag{A.11}$$

We now compute the Fourier transforms of $c_k(t)$ and $s_k(t)$ in order to be able to compute their power spectra and cross-spectra. That is, we decompose $c_k(t)$ and $s_k(t)$ as

$$c_k(t) = \hat{c}_{k,j}e^{i\omega_j t} + \hat{c}_{k,-j}e^{-i\omega_j t} \tag{A.12}$$

$$s_k(t) = \hat{s}_{k,j}e^{i\omega_j t} + \hat{s}_{k,-j}e^{-i\omega_j t}. \tag{A.13}$$

where

$$\hat{c}_{k,j} = \frac{1}{2}(\cos\phi_{k,j} + \cos\phi_{k,-j} + i\sin\phi_{k,j} - i\sin\phi_{k,-j}) \tag{A.14}$$

$$\hat{s}_{k,j} = \frac{1}{2}(-\sin\phi_{k,j} - \sin\phi_{k,-j} + i\cos\phi_{k,j} - i\cos\phi_{k,-j}) \tag{A.15}$$

and $\hat{c}_{k,-j} = (\hat{c}_{k,j})^\dagger$ and $\hat{s}_{k,-j} = (\hat{s}_{k,j})^\dagger$. Using these formulas one can show that

$$P_\omega(c_k) = |\hat{c}_{k,j}|^2 = \cos^2\left(\frac{\phi_{k,j} + \phi_{k,-j}}{2}\right) \tag{A.16}$$

$$P_\omega(s_k) = |\hat{s}_{k,j}|^2 = \sin^2\left(\frac{\phi_{k,j} + \phi_{k,-j}}{2}\right) \tag{A.17}$$

$$K_\omega(c_k, s_k) = \mathrm{Re}(\hat{c}_{k,j} \cdot \hat{s}_{k,j}) = -\frac{1}{2}\sin(\phi_{k,j} + \phi_{k,-j}). \tag{A.18}$$

Thus, substituting the above into Equation A.7 we have that

$$\begin{aligned}
\alpha &= \tan^{-1}\left(\frac{-\sin(\phi_{k,j} + \phi_{k,-j})}{\cos^2\left(\frac{\phi_{k,j}+\phi_{k,-j}}{2}\right) - \sin^2\left(\frac{\phi_{k,j}+\phi_{k,-j}}{2}\right)}\right) \\
&= -\tan^{-1}\left(\frac{\sin(\phi_{k,j} + \phi_{k,-j})}{\cos(\phi_{k,j} + \phi_{k,-j})}\right) \\
&= -(\phi_{k,j} + \phi_{-k,j}) \\
&= -2\overline{\phi}_{k,j}
\end{aligned} \tag{A.19}$$

as required.

A.3 Variance over time

Here we show how the variance over time of a single-wavenumber signal can be rewritten as a sum over the Fourier coefficients. We consider

$$q_k(\lambda, t) = \frac{2}{NT}\sum_{j=-T_2}^{T_2} Q_{k,j}\cos\left(k\lambda + \omega_j t + \phi_{k,j}\right). \tag{A.20}$$

We compute the variance over time of the single-wavenumber signal (assuming the time-mean is zero), a quantity which depends on longitude:

$$\begin{aligned}\mathrm{var}[q_k](\lambda) &= \frac{1}{T}\sum_{t=0}^{T-1}\left(q_k(\lambda,t)\right)^2 \\ &= \frac{4}{N^2T^3}\sum_{j=-T_2}^{T_2}\sum_{j'=-T_2}^{T_2} Q_{k,j}Q_{k,j'}\cdot \\ &\sum_{t=0}^{T-1}\cos\left(k\lambda+\omega_j t+\phi_{k,j}\right)\cos\left(k\lambda+\omega_{j'}t+\phi_{k,j'}\right) \qquad \text{(A.21)}\end{aligned}$$

where we have substituted in Eq. A.20, and then changed the order of summation. Using the orthogonality of the cosine basis functions, one can show

$$\begin{aligned}&\sum_{t=0}^{T-1}\cos\left(k\lambda+\omega_j t+\phi_{k,j}\right)\cos\left(k\lambda+\omega_{j'}t+\phi_{k,j'}\right) \\ &\quad= \frac{T}{2}\delta_{j,j'}+\frac{T}{2}\cos(2k\lambda+2\overline{\phi}_{k,j})\delta_{j,-j'} \\ &\quad= \frac{T}{2}\delta_{j,j'}+\frac{T}{2}\left(2\cos^2(k\lambda+\overline{\phi}_{k,j})-1\right)\delta_{j,-j'}. \qquad \text{(A.22)}\end{aligned}$$

Substituting Eq. A.22 into Eq. A.21 we have our final result for the variance over time of our signal represented as a sum over the Fourier coefficients:

$$\begin{aligned}\mathrm{var}[q_k](\lambda) = \frac{2}{N^2T^2}\sum_{j=-T_2}^{T_2}&\left\{Q_{k,j}^2+2Q_{k,j}Q_{k,-j}\cos^2(k\lambda+\overline{\phi}_{k,j})\right. \\ &\left.-Q_{k,j}Q_{k,-j}\right\}. \qquad \text{(A.23)}\end{aligned}$$

Bibliography

Albers, J. R. and T. Birner, 2014: Vortex preconditioning due to planetary and gravity waves prior to sudden stratospheric warmings. *J. Atmos. Sci.*, **71**, 4028–4054.

Andrews, D. G., J. R. Holton, and C. B. Leovy, 1987: *Middle Atmosphere Dynamics*. Academic Press.

Andrews, D. G. and M. E. McIntyre, 1976: Planetary waves in horizontal and vertical shear: the generalized Eliassen-Palm relation and the mean zonal acceleration. *J. Atmos. Sci.*, **33**, 2031–2048.

Arkin, P. A. and P. E. Ardanuy, 1989: Estimating climatic-scale precipitation from space: a review. *J. Clim.*, **2**, 1229–1238.

Baldwin, M. P. and T. J. Dunkerton, 1999: Propagation of the Arctic Oscillation from the stratosphere to the troposphere. *J. Geophys. Res.*, **104**, 30 937–30 946.

Baldwin, M. P. and T. J. Dunkerton, 2001: Stratospheric harbingers of anomalous weather regimes. *Science*, **294**, 581–584.

Baldwin, M. P., P. B. Rhines, H.-P. Huang, and M. E. McIntyre, 2007: The jet-stream conundrum. *Science*, **315**, 467–468.

Baldwin, M. P., D. B. Stephenson, D. W. J. Thompson, T. J. Dunkerton, A. J. Charlton, and A. O'Neill, 2003: Stratospheric memory and skill of extended-range weather forecasts. *Science*, **301**, 636–640.

Baldwin, M. P. and D. W. J. Thompson, 2009: A critical comparison of stratosphere-troposphere coupling indices. *Quarterly Journal of the Royal Meteorological Society*, **135**, 1661–1672.

Barnes, E. A., 2013: Revisiting the evidence linking Arctic amplification to extreme weather in midlatitudes. *Geophys. Res. Lett.*, **40**, 4734–4739.

Blackmon, M. L., 1976: A climatological spectral study of the 500 mb geopotential height of the Northern Hemisphere. *J. Atmos. Sci.*, **33**, 1607–1623.

Blackport, R. and P. J. Kushner, 2016: The transient and equilibrium climate response to rapid summertime sea ice loss in CCSM4. *J. Clim.*, **29**, 401–417.

Bornman, J. F., N. Paul, and X. Tang, 2011: Environmental effects of ozone depletion and its interactions with climate change: 2010 assessment. *Photochem. Photobiol. Sci.*, **10**, 174.

Boville, B. A., 1984: The influence of the polar night jet on the tropospheric circulation in a GCM. *J. Atmos. Sci.*, **41**, 1132–1142.

Branstator, G., 1987: A striking example of the atmosphere's leading traveling pattern. *J. Atmos. Sci.*, **44**, 2310–2323.

Butchart, N., S. A. Clough, T. N. Palmer, and P. J. Trevelyan, 1982: Simulations of an observed stratospheric warming with quasi-geostrophic refractive index as a model diagnostic. *Quart. J. Roy. Meteorol. Soc.*, **108**, 475–502.

Butler, A. H. and L. M. Polvani, 2011: El Niño, La Niña, and stratospheric sudden warmings: a re-evaluation in light of the observational record. *Geophys. Res. Lett.*, **38**, L13 807.

Butler, A. H., D. J. Seidel, S. C. Hardiman, N. Butchart, T. Birner, and A. Match, 2015: Defining sudden stratospheric warmings. *Bulletin of the American Meteorological Society*, **96**, 1913–1928.

Charlton, A. J., A. O'Neill, D. B. Stephenson, W. Lahoz, and M. Baldwin, 2003: Can knowledge of the state of the stratosphere be used to improve statistical forecasts of the troposphere? *Quarterly Journal of the Royal Meteorological Society*, **129**, 3205–3224.

Charlton, A. J. and L. M. Polvani, 2007: A new look at stratospheric sudden warmings. Part I: Climatology and modeling benchmarks. *J. Clim.*, **20**, 449–469.

Charney, J. G. and P. G. Drazin, 1961: Propagation of planetary-scale disturbances from the lower into the upper atmosphere. *J. Geophys. Res.*, **66**, 83–109.

Charney, J. G. and A. Eliassen, 1949: A numerical method for predicting the perturbations of the middle latitude westerlies. *Tellus*, **1**, 38–54.

Cohen, J., M. Barlow, P. J. Kushner, and K. Saito, 2007: Stratosphere-troposphere coupling and links with Eurasian land surface variability. *J. Clim.*, **20**, 5335–5343.

Cohen, J. and J. Jones, 2011: Tropospheric precursors and stratospheric warmings. *J. Climate*, **25**, 1780–1790.

Cohen, J. et al., 2014: Recent Arctic amplification and extreme mid-latitude weather. *Nature Geosci.*, **7**, 627–637.

Coumou, D., V. Petoukhov, S. Rahmstorf, S. Petri, and H. J. Schellnhuber, 2014: Quasi-resonant circulation regimes and hemispheric synchronization of extreme weather in boreal summer. *Proc. Natl. Acad. Sci. USA*, **111**, 12 331–12 336.

Coumou, D. and S. Rahmstorf, 2012: A decade of weather extremes. *Nature Clim. Change*, **2**, 491–496.

Davies, H. C., 2015: Weather chains during the 2013/2014 winter and their significance for seasonal prediction. *Nature Geosci.*, **8**, 833–836.

Dee, D. P. et al., 2011: The ERA-Interim reanalysis: Configuration and performance of the data assimilation system. *Q. J. Roy. Meteor. Soc.*, **137**, 553–597.

Di Biagio, V., S. Calmanti, A. Dell'Aquila, and P. M. Ruti, 2014: Northern hemisphere winter midlatitude atmospheric variability in CMIP5 models. *Geophys. Res. Lett.*, **41**, 1277–1282.

Dias, J. and G. N. Kiladis, 2016: The relationship between equatorial mixed Rossby-gravity and eastward inertio-gravity waves. Part II. *J. Atmos. Sci.*, **73**, 2147–2163.

Douville, H., 2009: Stratospheric polar vortex influence on Northern Hemisphere winter climate variability. *Geophys. Res. Lett.*, **36**, L18 703.

Dunn-Sigouin, E. and T. A. Shaw, 2015: Comparing and contrasting extreme stratospheric events, including their coupling to the tropospheric circulation. *J. Geophys. Res. Atmos.*, **120**, doi:10.1002/2014JD022 116.

Eliassen, A. and E. Palm, 1961: On the transfer of energy in stationary mountain waves. *Geofys. Publ.*, **22**, 1–23.

Esler, J. G., L. M. Polvani, and R. K. Scott, 2006: The Antarctic stratospheric sudden warming of 2002: a self-tuned resonance? *Geophys. Res. Lett.*, **33**, L12 804.

Esler, J. G. and R. K. Scott, 2005: Excitation of transient Rossby waves on the stratospheric polar vortex and the barotropic sudden warming. *J. Atmos. Sci.*, **62**, 3661–3682.

Eyring, V. et al., 2015: Overview of the Coupled Model Intercomparison Project Phase 6 (CMIP6). *Geosci. Model Dev. Discuss.*, **8**, 10 539–10 583.

Fletcher, C. G. and P. J. Kushner, 2011: The role of linear interference in the annular mode response to tropical SST forcing. *J. Clim.*, **24**, 778–794.

Fraedrich, K. and H. Böttger, 1978: A wavenumber-frequency analysis of the 500mb geopotential at 50°N. *J. Atmos. Sci.*, **35**, 745–750.

Francis, J. A. and S. J. Vavrus, 2012: Evidence linking Arctic amplification to extreme weather in mid-latitudes. *Geophys. Res. Lett.*, **39**, L06 801.

Fritts, D. C., 2003: *Encyclopedia of Atmospheric Sciences*. Academic Press, 1308-1314 pp.

Fusco, A. C. and M. L. Salby, 1999: Interannual variations of total ozone and their relationship to variations of planetary wave activity. *J. Clim.*, **12**, 1619–1629.

Garfinkel, C., D. Hartmann, and F. Sassi, 2010: Tropospheric precursors of anomalous Northern Hemisphere stratospheric polar vortices. *J. Clim.*, **23**, 3282–3299.

Garfinkel, C. I., J. J. Benedict, and E. D. Maloney, 2014: Impact of the MJO on the boreal winter extratropical circulation. *Geophys. Res. Lett.*, **41**, 6055–6062.

Garfinkel, C. I., S. B. Feldstein, D. W. Waugh, C. Yoo, and S. Lee, 2012: Observed connection between stratospheric sudden warmings and the Madden-Julian Oscillation. *Geophys. Res. Lett.*, **39**, L18 807.

Gerber, E. P. and E. Manzini, 2016: Dynvarmip: Assessing the dynamics and variability of the stratosphere-troposphere system. *Geosci. Model Dev. Discuss.*, **in review**.

Gerber, E. P. et al., 2010: Stratosphere-troposphere coupling and annular mode variability in chemistry-climate models. *J. Geophys. Res.*, **115**, D00M06.

Gerber, E. P. et al., 2012: Assessing and understanding the impact of stratospheric dynamics and variability on the earth system. *Bull. Am. Meteorol. Soc.*, **93**, 845–859.

Gillett, N. P., M. P. Baldwin, and M. R. Allen, 2001: Evidence for nonlinearity in observed stratospheric circulation changes. *J. Geophys. Res.*, **106**, 7891–7901.

Gillett, N. P. and D. W. J. Thompson, 2003: Simulation of recent Southern Hemisphere climate change. *Science*, **302**, 273–275.

Harnik, N., 2009: Observed stratospheric downward reflection and its relation to upward pulses of wave activity. *J. Geophys. Res.*, **114**, D08 120.

Hartmann, D. L., 2015: Pacific sea surface temperature and the winter of 2014. *Geophys. Res. Lett.*, **42**, 1894–1902.

Haurwitz, B., 1940: The motion of atmospheric disturbances on a spherical earth. *J. Mar. Res.*, **3**, 254–267.

Hayashi, Y., 1971: A generalized method of resolving disturbances into progressive and retrogressive waves by space fourier and time cross-spectral analyses. *J. Meteor. Soc. Japan*, **49**, 125–128.

Hayashi, Y., 1973: A method of analyzing transient waves by space-time cross spectra. *J. Appl. Meteorol.*, **12**, 404–408.

Hayashi, Y., 1977: On the coherence between progressive and retrogressive waves and a partition of space-time power spectra into standing and traveling parts. *J. Appl. Meteorol.*, **16**, 368–373.

Hayashi, Y., 1979: A generalized method of resolving transient disturbances into standing and traveling waves by space-time spectral analysis. *J. Atmos. Sci.*, **36**, 1017–1029.

Held, I. M., 1983: Stationary and quasi-stationary eddies in the extratropical troposphere: theory. *Large-scale dynamical processes in the atmosphere*, B. J. Hoskins and R. P. Pearce, Eds., Academic Press, 127–168.

Hendon, H. H. and M. C. Wheeler, 2008: Some space-time spectral analyses of tropical convection and planetary-scale waves. *J. Atmos. Sci.*, **65**, 2936–2948.

Hitchcock, P., T. G. Shepherd, and G. L. Manney, 2013: Statistical characterization of Arctic polar-night jet oscillation events. *J. Clim.*, **26**, 2096–2116.

Holton, J. R., P. H. Haynes, M. E. McIntyre, A. R. Douglass, R. B. Rood, and L. Pfister, 1995: Stratosphere-troposphere exchange. *Rev. Geophys.*, **33**, 403–439.

Holton, J. R. and C. Mass, 1976: Stratospheric vacillation cycles. *J. Atmos. Sci.*, **33**, 2218–2225.

Holton, J. R. and H. C. Tan, 1980: The influence of the equatorial Quasi-Biennial Oscillation on the global circulation at 50 mb. *J. Atmos. Sci.*, **37**, 2200–2208.

Hoskins, B. J. and D. J. Karoly, 1981: The steady linear response of a spherical atmosphere to thermal and orographic forcing. *J. Atmos. Sci.*, **38**, 1179–1196.

Hoskins, B. J. and P. J. Valdes, 1990: On the existence of storm-tracks. *J. Atmos. Sci.*, **47**, 1854–1864.

Ineson, S. and A. A. Scaife, 2009: The role of the stratosphere in the European climate response to El Niño. *Nature Geosci.*, **2**, 32–36.

Kalnay, E. et al., 1996: The NCEP/NCAR 40-year reanalysis project. *Bull. Amer. Meteor. Soc.*, **77**, 437–471.

Kiladis, G. N., J. Dias, and M. Gehne, 2016: The relationship between equatorial mixed Rossby-gravity and eastward inertio-gravity waves. Part I. *J. Atmos. Sci.*, **73**, 2123–2145.

Kodera, K. and H. Koide, 1997: Spatial and seasonal characteristics of recent decadal trends in the Northern Hemispheric troposphere and stratosphere. *Journal of Geophysical Research: Atmospheres*, **102**, 19 433–19 447.

Kodera, K., K. Yamazaki, M. Chiba, and K. Shibata, 1990: Downward propagation of upper stratospheric mean zonal wind perturbation to the troposphere. *Geophys. Res. Lett.*, **17**, 1263–1266.

Kug, J.-S. et al., 2015: Two distinct influences of Arctic warming on cold winters over North America and East Asia. *Nature Geosci.*, **8**, 759–762.

Labitzke, K., 1981: The amplification of height wave 1 in January 1979: A characteristic precondition for the major warming in February. *Mon. Wea. Rev.*, **109**, 983–989.

Labitzke, K., 1982: On the interannual variability of the middle stratosphere during the northern winters. *J. Meteor. Soc. Japan*, **60**, 124–139.

Lau, K.-M. and P. H. Chan, 1983: Short-term climate variability and atmospheric teleconnections from satellite-observed outgoing longwave radiation. Part II: Lagged correlations. *J. Atmos. Sci.*, **40**, 2751–2767.

Lau, N.-C. and E. O. Holopainen, 1984: Transient eddy forcing of the time-mean flow as identified by geopotential tendencies. *J. Atmos. Sci.*, **41**, 313–328.

Lau, N.-C. and J. M. Wallace, 1979: On the distribution of horizontal transports by transient eddies in the Northern Hemisphere wintertime circulation. *J. Atmos. Sci.*, **36**, 1844–1861.

Lee, M.-Y., C.-C. Hong, and H.-H. Hsu, 2015: Compounding effects of warm sea surface temperature and reduced sea ice on the extreme circulation over the extratropical North Pacific and North America during the 2013-2014 boreal winter. *Geophys. Res. Lett.*, **42**, 1612–1618.

Liebmann, B. and C. A. Smith, 1996: Description of a complete (interpolated) outgoing longwave radiation dataset. *Bull. Amer. Meteor. Soc.*, **77**, 1275–1277.

Limpasuvan, V. and D. L. Hartmann, 1999: Eddies and the annular modes of climate variability. *Geophys. Res. Lett.*, **26**, 3133–3136.

Limpasuvan, V., D. W. J. Thompson, and D. L. Hartmann, 2004: The life cycle of the Northern Hemisphere sudden stratospheric warmings. *J. Clim.*, **17**, 2584–2596.

Lindzen, R. S., B. Farrell, and D. Jacqmin, 1982: Vacillations due to wave interference: Applications to the atmosphere and to annulus experiments. *J. Atmos. Sci.*, **39**, 14–23.

Lucarini, V., S. Calmanti, A. Dell'Aquila, P. M. Ruti, and A. Speranza, 2007: Intercomparison of the northern hemisphere winter midlatitude atmospheric variability of the IPCC models. *Clim. Dyn.*, **28**, 829–848.

Madden, R. A., 1975: Oscillations in the winter stratosphere: Part 2: The role of horizontal eddy heat transport and the interaction of transient and stationary planetary scale waves. *Mon. Wea. Rev.*, **102**, 717–729.

Madden, R. A., 1979: Observations of large-scale traveling Rossby waves. *Rev. Geophys. Space Phys.*, **17**, 1935–1949.

Madden, R. A. and P. Speth, 1989: The average behavior of large-scale westward traveling disturbances evident in the Northern Hemisphere geopotential hieghts. *J. Atmos. Sci.*, **46**, 3225–3239.

Manney, G. L. et al., 2011: Unprecedented Arctic ozone loss in 2011. *Nature*, **478**, 469–475.

Martius, O., L. M. Polvani, and H. C. Davies, 2009: Blocking precursors to stratospheric sudden warming events. *Geophys. Res. Lett.*, **36**, L14 806.

Masumoto, Y. and G. Meyers, 1998: Forced Rossby waves in the southern tropical Indian Ocean. *J. Geophys. Res.*, **103**, 27 589–27 602.

Matsuno, T., 1966: Quasi-geostrophic motions in the equatorial area. *J. Meteor. Soc. Japan*, **44**, 25–43.

Matsuno, T., 1971: A dynamical model of the stratospheric sudden warming. *J. Atmos. Sci.*, **28**, 1479–1494.

May, W., 1999: Space-time spectra of the atmospheric intraseasonal variability in the extratropics and their dependency on the El Niño/Southern Oscillation phenomenon: model versus observation. *Clim. Dyn.*, **15**, 369–387.

McIntyre, M. E., 1972: Baroclinic instability of an idealized model of the polar night jet. *Quart. J. Roy. Meteorol. Soc.*, **98**, 165–174.

McIntyre, M. E., 1982: How well do we understand the dynamics of stratospheric warmings? *J. Meteor. Soc. Japan*, **60**, 37–65.

McIntyre, M. E., 1989: On dynamics and transport near the polar mesopause in summer. *J. Geophys. Res.*, **94**, 14 617–14 628.

Murray, F. W., 1960: Dynamical stability of the stratosphere. *J. Geophys. Res.*, **65**, 3273–3305.

Newman, P. A. and E. R. Nash, 2005: The unusual Southern Hemisphere stratosphere winter of 2002. *J. Atmos. Sci.*, **62**, 614–628.

Newman, P. A., E. R. Nash, and J. E. Rosenfield, 2001: What controls the temperature of the Arctic stratosphere during the spring. *J. Geophys. Res.*, **106 (D17)**, 19 999–20 010.

Nishii, K., H. Nakamura, and T. Miyasaka, 2009: Modulations in the planetary wave field induced by upward-propagating Rossby wave packets prior to stratospheric wudden warming events: A case study. *Q. J. R. Meterol. Soc.*, **135**, 39–52.

Peixoto, J. P. and A. H. Oort, 1992: *Physics of Climate*. American Institute of Physics.

Petoukhov, V., S. Rahmstorf, S. Petri, and H. J. Schellnhuber, 2013: Quasiresonant amplication of planetary waves and recent Northern Hemisphere weather extremes. *Proc. Natl. Acad. Sci. USA*, **110**, 5336–5341.

Plumb, R. A., 1981: Instability of the distorted polar night vortex: A theory of stratospheric warmings. *J. Atmos. Sci.*, **38**, 2514–2531.

Polvani, L. M. and P. J. Kushner, 2002: Tropospheric response to stratospheric peturbations in a relatively simple general circulation model. *Geophys. Res. Lett.*, **29 (7)**.

Polvani, L. M. and D. W. Waugh, 2004: Upward wave activity flux as a precursor to extreme stratospheric events and subsequent anomalous surface weather regimes. *J. Clim.*, **17**, 3548–3554.

Pratt, R. W., 1976: The interpretation of space-time spectral quantities. *J. Atmos. Sci.*, **33**, 1060–1066.

Quiroz, R. S., 1986: The association of stratospheric warmings with tropospheric blocking. *J. Geophys. Res.*, **91**, 5277–5285.

Randel, W. J., 1987: A study of planetary waves in the southern winter troposphere and stratosphere. Part I: Wave structure and vertical propagation. *J. Atmos. Sci.*, **44**, 917–935.

Randel, W. J. and I. M. Held, 1991: Phase speed spectra of transient eddy fluxes and critical layer absorption. *J. Atmos. Sci.*, **48**, 688–697.

Randel, W. J., F. Wu, and R. Stolarski, 2002: Changes in column ozone correlated with the stratospheric EP flux. *J. Meteor. Soc. Japan*, **80**, 849–862.

Salby, M. L. and R. R. Garcia, 1987: Vacillations induced by interference of stationary and traveling planetary waves. *J. Atmos. Sci.*, **44**, 2679–2711.

Scaife, A. A., J. R. Knight, G. K. Vallis, and C. K. Folland, 2005: A stratospheric influence on the winter NAO and North Atlantic surface climate. *Geophys. Res. Lett.*, **32**, L18 715.

Scaife, A. A. et al., 2014: Skillful long-range prediction of European and North American winters. *Geophys. Res. Lett.*, **41**, 2514–2519.

Scaife, A. A. et al., 2016: Seasonal winter forecasts and the stratosphere. *Atmos. Sci. Lett.*, **17**, 51–56.

Scherhag, R., 1952: Die explosionsartigen stratosphärenerwärmungen des spätwinters. *Ber. Deutsch. Wetterdienstes (US Zone)*, **38**, 51–63.

Scinocca, J. F., N. A. McFarlane, M. Lazare, and D. Plummer, 2008: The CCCma third generation AGCM and its extension into the middle atmosphere. *Atmos. Chem. Phs.*, **8**, 7055–7074.

Screen, J. A., C. Deser, and L. Sun, 2015: Reduced risk of North American cold extremes to continued arctic sea ice loss. *Bull. Amer. Meteor. Soc.*, **96**, 1489–1503.

Screen, J. A. and I. Simmonds, 2013: Exploring links between Arctic amplification and mid-latitude weather. *Geophys. Res. Lett.*, **40**, 959–964.

Screen, J. A. and I. Simmonds, 2014: Amplified mid-latitude planetary waves favour particular regional weather extremes. *Nature Clim. Change*, **4**, 704–709.

Shaw, T. A. and J. Perlwitz, 2013: The life cycle of Northern Hemisphere downward wave coupling between the stratosphere and troposphere. *J. Clim.*, **26**, 1745–1763.

Shaw, T. A. and J. Perlwitz, 2014: On the control of the residual circulation and stratospheric temperatures in the Arctic by planetary wave coupling. *J. Atmos. Sci.*, **71**, 195–206.

Shaw, T. A., J. Perlwitz, and N. Harnik, 2010: Downward wave coupling between the stratosphere and troposphere: The importance of meridional wave guiding and comparison with zonal-mean coupling. *J. Clim.*, **23**, 6365–6381.

Shaw, T. A., M. Sigmond, T. G. Shepherd, and J. F. Scinocca, 2009: Sensitivity of simulated climate to conservation of momentum in gravity wave drag parameterization. *J. Clim.*, **22**, 2726–2742.

Shepherd, T. G., 2014: Atmospheric circulation as a source of uncertainty in climate change projections. *Nature Geosci.*, **7**, 703–708.

Shindell, D. T., R. L. Miller, G. A. Schmidt, and L. Pandolfo, 1999: Simulation of recent northern winter climate trends by greenhouse-gas forcing. *Nature*, **399**, 452–455.

Sigmond, M. and J. C. Fyfe, 2016: Tropical Pacific impacts on cooling North American winters. *Nature Clim. Change*.

Sigmond, M., J. F. Scinocca, V. V. Kharin, and T. G. Shepherd, 2013: Enhanced seasonal forecast skill following stratospheric sudden warmings. *Nature Geoscience*, **6**, 98–102.

Sjoberg, J. P. and T. Birner, 2012: Transient tropospheric forcing of sudden stratospheric warmings. *J. Atmos. Sci.*, **69**, 3420–3432.

Sjoberg, J. P. and T. Birner, 2014: Stratospheric wave-mean flow feedbacks and sudden stratospheric warmings in a simple model forced by upward wave activity flux. *J. Atmos. Sci.*, **71**, 4055–4071.

Smagorinsky, J., 1953: The dynamical influence of large-scale heat sources and sinks on the quasi-stationary mean motions of the atmosphere. *Q. J. R. Meteorol. Soc.*, **79**, 342–366.

Smith, K. L., 2012: Eurasian snow cover and the role of linear interference in stratosphere-troposphere interactions. Ph.D. thesis, University of Toronto.

Smith, K. L., C. G. Fletcher, and P. J. Kushner, 2010: The role of linear interference in the annular mode response to extratropical surface forcing. *J. Clim.*, **23**, 6036–6050.

Smith, K. L. and P. J. Kushner, 2012: Linear interference and the initiation of extra-tropical stratosphere-troposphere interactions. *Journal of Geophysical Research*, **117**, D13 107.

Smith, K. L., P. J. Kushner, and J. Cohen, 2011: The role of linear interference in northern annular mode variability associated with Eurasian snow cover extent. *J. Clim.*, **24**, 6185–6202.

Solomon, S., 1999: Stratospheric ozone depletion: a review of concepts and history. *Rev. Geophys.*, **37**, 275–316.

Son, S.-W. et al., 2008: The impact of stratospheric ozone recovery on the Southern Hemisphere winter jet. *Science*, **320**, 1486–1489.

Speth, P. and R. A. Madden, 1983: Space-time spectral analyses of Northern Hemisphere geopotential heights. *J. Atmos. Sci.*, **40**, 1086–1100.

Taguchi, M., 2016: Connection of predictability of major stratospheric sudden warmings to polar vortex geometry. *Atmos. Sci. Lett.*, **17**, 33–38.

Takayabu, Y. N., 1994: Large-scale cloud disturbances associated with Equatorial waves. Part I: spectral features of the cloud disturbances. *J. Meteor. Soc. Japan*, **72**, 433–448.

Taylor, K., R. Stouffer, and G. Meehl, 2012: An overview of CMIP5 and the experiment design. *Bull. Am. Meteorol. Soc.*, **93**, 485–498.

Thompson, D. W. J., M. P. Baldwin, and J. M. Wallace, 2002: Stratospheric connection to Northern Hemisphere wintertime weather: Implications for prediction. *J. Clim.*, **15**, 1421–1428.

Thompson, D. W. J. and J. M. Wallace, 2000: Annular modes in the extratropical circulation. Part I: month-to-month variability. *J. Clim.*, **13**, 1000–1016.

Trenberth, K. E. et al., 1998: Progress during TOGA in understanding and modeling global teleconnections associated with tropical sea surface temperatures. *J. Geophys. Res.*, **103**, 14 291–14 234.

Tripathi, O. P. et al., 2015: The predictability of the extratropical stratosphere on monthly time-scales and its impact on the skill of tropospheric forecasts. *Q. J. R. Meteorol. Soc.*, **141**, 987–1003.

Tripathi, O. P. et al., 2016: Examining the predictability of the Stratospheric Sudden Warming of January 2013 using multiple NWP systems. *Mon. Wea. Rev.*, **144**, 1935–1960.

Tsay, C.-Y., 1974: A note on the methods of analyzing traveling waves. *Tellus*, **26**, 412–415.

Tung, K. K. and R. Lindzen, 1979a: A theory of stationary long waves. Part I: A simple theory of blocking. *Mon. Wea. Rev.*, **107**, 714–734.

Tung, K. K. and R. Lindzen, 1979b: A theory of stationary long waves. Part II: Resonant Rossby waves in the presence of realistic vertical shears. *Mon. Wea. Rev.*, **107**, 735–750.

Voldoire, A. et al., 2013: The CNRM-CM5.1 global climate model: description and basic evaluation. *Clim. Dyn.*, **40**, 2091–2121.

von Storch, H. and F. W. Zwiers, 1999: *Statistical Analysis in Climate Research*. Cambridge Univ. Press.

Wallace, J. M. and D. S. Gutzler, 1981: Teleconnections in the geopotential height field during the Northern Hemisphere winter. *Mon. Wea. Rev.*, **109**, 784–812.

Wallace, J. M. and V. E. Kousky, 1968: Observational evidence of Kelvin waves in the tropical stratosphere. *J. Atmos. Sci.*, **25**, 280–292.

Wang, S.-Y., L. Hipps, R. R. Gillies, and J.-H. Yoon, 2014: Probable causes of the abnormal ridge accompanying the 2013/14 California drought: ENSO precursor and anthropogenic warming footprint. *Geophys. Res. Lett.*, **41**, 3220–3226.

Wang, S.-Y., W.-R. Huang, and J.-H. Yoon, 2015: The North American winter 'dipole' and extremes activity: a CMIP5 assessment. *Atmos. Sci. Lett.*, **16**, 338–345.

Watt-Meyer, O. and P. J. Kushner, 2015a: Decomposition of atmospheric disturbances into standing and traveling components, with application to Northern Hemisphere planetary waves and stratosphere-troposphere coupling. *J. Atmos. Sci.*, **72**, 787–802.

Watt-Meyer, O. and P. J. Kushner, 2015b: The role of standing waves in driving persistent anomalies of upward wave activity flux. *J. Clim.*, **28**, 9941–9954.

Waugh, D. W., A. H. Sobel, and L. M. Polvani, 2016: What is the polar vortex, and how does it influence weather? *Bull. Amer. Meteor. Soc.*, in press.

Wheeler, M. and G. N. Kiladis, 1999: Convectively coupled equatorial waves: Analysis of clouds and temperatures in the wavenumber-frequency domain. *J. Atmos. Sci.*, **56**, 374–399.

Wheeler, M. C. and H. H. Hendon, 2004: An all-season Real-Time Multivariate MJO Index: development of an index for monitoring and prediction. *Mon. Wea. Rev.*, **132**, 1917–1932.

White, W. B., 2000: Coupled Rossby waves in the Indian Ocean on interannual timescales. *J. Phys. Oceanogr.*, **30**, 2972–2988.

White, W. B. and D. R. Cayan, 2000: A global El Niño-Southern Oscillation wave in surface temperature and pressure and its interdecadal modulation from 1900 to 1997. *J. Geophys. Res.*, **105**, 11 223–11 242.

Wolter, K. et al., 2015: How unusual was the cold winter of 2013/14 in the upper midwest? *Explaining extremes of 2014 from a climate perspective*, Bull. Amer. Meteor. Soc.

Yanai, M. and T. Maruyama, 1966: Stratospheric wave disturbances propagating over the equatorial Pacific. *J. Meteor. Soc. Japan*, **44**, 291–294.

Yoden, S., M. Taguchi, and Y. Naito, 2002: Numerical studies on time variations of the troposphere-stratosphere coupled system. *J. Meteor. Soc. Japan*, **80**, 811–830.

Zhang, C. and H. H. Hendon, 1997: Propagating and standing components of the intraseasonal oscillation in tropical convection. *J. Atmos. Sci.*, **54**, 741–752.

Copyright Acknowledgements

Chapter 2 is based on Watt-Meyer, O. and P. J. Kushner, 2015: Decomposition of atmospheric disturbances into standing and traveling components, with application to Northern Hemisphere planetary waves and stratosphere-troposphere coupling. *J. Atmos. Sci.*, **72**, 787-802.

Chapter 3 is based on Watt-Meyer, O. and P. J. Kushner, 2015: The role of standing waves in driving persistent anomalies of upward wave activity flux. *J. Clim.*, **28**, 9941-9954.